Assessing Teratogen-Induced Changes in Murine Fetal Brain Vasculature Using *In Utero* Optical Coherence Tomography

by
Raksha Raghunathan

A dissertation submitted to the Department of Biomedical Engineering,
Cullen College of Engineering
in partial fulfillment of the requirements for the degree of

Doctor of Philosophy

in Biomedical Engineering

Chair of Committee: Kirill V. Larin

Committee Member: Rajesh C. Miranda

Committee Member: Howard Gifford

Committee Member: Yingchun Zhang

Committee Member: David Mayerich

University of Houston
May 2020

Copyright 2020, Raksha Raghunathan

DEDICATION

This dissertation is dedicated to my biggest cheerleaders in life, my parents.

You both have stood by my side through thick and thin. Thank you for keeping me comfortable no matter what the situation was, and for giving me the best of everything. You did your best to make sure I got everything I needed and more. Your hard work, sacrifice, and blessings have been crucial for me thus far, and I am eternally grateful for everything you have done.

I hope I made you proud. This is just the first step.

ACKNOWLEDGMENTS

First, I would like to extend my deepest gratitude to Dr. Kirill Larin for giving me an opportunity to carry out my graduate work in his Biomedical Optics Laboratory. He has been an inspiration, role model, and an extremely supportive mentor. He has helped me push my limits and has constantly given me all the encouragement, guidance, and inspiration needed for this journey. I am extremely grateful for all he has done for me and for all the opportunities he has provided me with during the course of my PhD.

I would like to sincerely thank the members of my dissertation committee- Dr. Miranda, Dr. Gifford, Dr. Mayerich, and Dr. Zhang for their time, invaluable inputs, and guidance. Dr. Miranda has been a great collaborator and co-mentor and has helped me in every step of my PhD. He has constantly provided me with his insights and has been extremely patient with me. I am grateful to have studied under Dr. Larin, and him.

I want to thank Drs. Manmohan Singh, Chen Wu, and Chih-Hao Liu for teaching me everything I know and for being constant pillars of support during the past six years, especially during my early years in the lab. I also thank my fellow graduate students Achuth Nair, and Justin Rippy. The five of you have stood by me through these years and have provided support and help in every way possible. All of you helped create the best work environment possible, and I am forever grateful to all of you. I could not have wished for a better family, here in Houston.

I want to thank Dr. Amanda Mahnke from Dr. Miranda's lab at Texas A&M for her insightful guidance with my project. I want to thank Drs. Salavat Aglyamov, Alexander Schill, Zhaolong Han, Narendran Sudheendran, and Jiasong Li for sharing their expertise and helping when needed. I also thank the other members of the Biomedical Optics Laboratory, including

Dr. Behzad Khajavi, graduate students Yogeshwari Ambekar, Hongqiu Zhang, and Harshdeep Singh Chawla, and all the undergraduate students in the lab for all your support. None of this would have been possible without any of your support.

I want to thank my cousins Sharanya, and Pranav, and two of my best friends-like-family Aishwarya and Prashanth. Words can't describe the roles you four have played in my life and these seven years in particular. Your constant love, encouragement, faith, and support on a daily basis has helped me get to the finish line of my PhD. Thank you, from the bottom of my heart.

I want to thank the rest of my family and friends for staying by my side and supporting me whenever I needed it the most.

This section would not be complete if I don't mention my parents. Even though I have already dedicated this dissertation to you both, I wanted to thank you here for everything you have done for me. Thank you for being there and loving me unconditionally. I am incredibly lucky to have you both as my parents and I am eternally grateful and forever indebted to both of you.

ABSTRACT

This dissertation reports the use of *in utero* optical coherence tomography to evaluate changes in vasculature in a developing murine fetal brain caused due to prenatal exposure to teratogens. Embryogenesis is a highly complex process that is extremely vulnerable to external factors. Proper visualization of embryonic development is crucial to understand the basic physiological processes and identify defects if any. This dissertation is divided into two major sections: 1) assessing teratogen induced changes in the murine fetal brain vasculature during the second trimester equivalent period (chapters 2-4) and 2) combining optical coherence tomography with Brillouin microscopy to image and evaluate changes in biomechanical properties during neural tube closure in order to study first trimester exposure to teratogens (appendix A3). The first section is further divided into the following sub-sections: 1) assessing alcohol induced changes in murine fetal brain vasculature, 2) assessing nicotine induced changes in murine fetal brain vasculature, and 3) assessing synthetic cannabinoid (SCB) induced changes in murine fetal brain vasculature. The advancement of algorithms to image and detect minute changes in vasculature are also detailed. The contributions of this work are significant to understand the effects of teratogens on development, as blood flow plays a major role in embryogenesis. Understanding the acute changes in vasculature caused within minutes of maternal exposure to a teratogen can open several new avenues to explore as blood flow drives organ development. Results from this dissertation have been published in 7 first author peer-reviewed publications.

TABLE OF CONTENTS

LIST OF TABLES

LIST OF FIGURES

Chapter-1 Introduction

This chapter introduces the work presented in this dissertation. The chapter starts with a brief explanation of embryogenesis and explains the need for imaging embryonic development, with a brief overview of all the techniques that have been used over the years. Since this work focuses on the use of optical coherence tomography, a summary of optical coherence tomography and its use in imaging embryonic development is also provided. The chapter concludes with the techniques used in this dissertation and an overview of the organization of this dissertation.

1.1 Embryogenesis

Embryogenesis is a highly complex and dynamic process. Understanding this process is highly interdisciplinary and involves several aspects of science including cell biology, biophysics, and engineering. Similar to the importance of basic processes involved in development, even the asymmetric placement and development of different organs in the body is of immense significance [1]. A slight change in the process can lead to congenital abnormalities, which are one of the main causes of infant mortality and have long term effects on quality of life. Present in about 3% of newborns, approximately 120,000 babies are affected annually because of congenital defects [2, 3]. This emphasizes the need to study and understand the basic processes involved in embryogenesis.

Several animal models have been developed to study embryonic development at different gestational stages. The murine model is well-preferred because of its close resemblance to human development and because numerous mutant models have been

developed that are closely associated with human diseases. These models have helped improve our understanding of not only development, but also disease progression and therapeutics. The total gestational period of a mouse is approximately 21 days. The first 10 days is considered the first trimester equivalent to humans, the second 10 days is the second trimester equivalent to humans, and the first 10 days after birth is considered the third trimester equivalent to human gestation. The process starts with fertilization, which occurs in the ampulla of the oviduct. This is followed by cleavage and blastulation of the fertilized egg. While cleavage refers to the mitotic cell divisions of the single cell zygote, blastulation refers to the formation of the blastula. The blastula is a spherical structure that consists of approximately hundreds of cells. The outer layer of the blastula is the trophoblast and the hollow inside of this sphere consists of a small group of cells called the inner cell mass (ICM) while the rest is filled with fluid. The trophoblast develops into the chorion and the placenta of the fetus, while the ICM develops into the fetus. Both cleavage and blastulation occurs as the fertilized zygote travels to the uterus via the fallopian tube. These processes occur between gestational day (GD) 0 and GD 4.0 in mice [4]. At GD 4.5 implantation occurs at the uterus [5] and immediately after, the process of gastrulation starts.

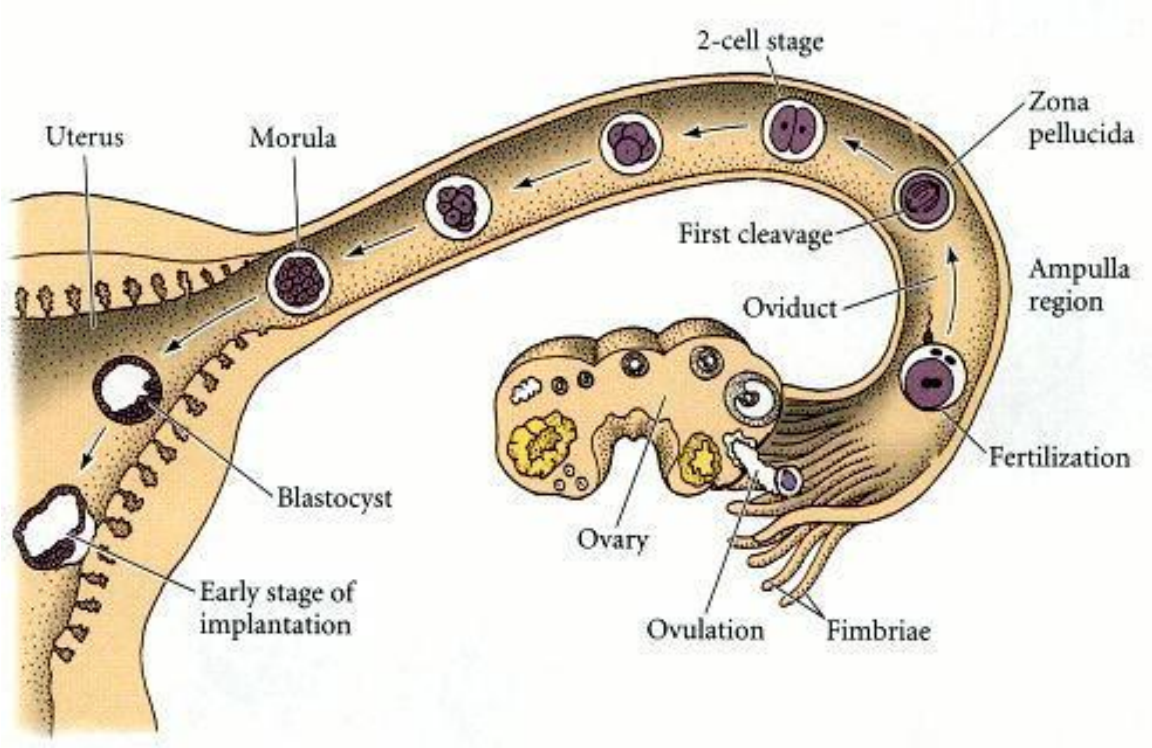

Figure 1.1 Development of a human embryo from fertilization to implantation. Adapted from [6]

Gastrulation [6] is the process by which the ICM forms the three basic germ layers: ectoderm, mesoderm, and endoderm. This is the step which decides the overall body plan [7]. Organogenesis begins right after gastrulation and the cardiovascular system is the first system that begins to develop. While the heart tube forms as early as GD 6.5, by about GD 8.0 the heart tube starts to contract [7-9]. For the first few hours plasma is circulated through the vascular system, and then blood cells from the blood islands start circulating, as the contractions get stronger. Within the next few hours, the fetus turns, the heart loops, and blood flow becomes stronger. A simple circulatory loop consisting of the heart, dorsal aorta, yolk sac plexus, and sinus venosus is set up at this time [10-12]. This marks the start of angiogenesis in the developing fetus, which includes the formation of new vessels through the remodeling of already existing vessels. Angiogenesis is dependent on both

genetic factors and the hemodynamic forces acting on the tissue [13, 14], and plays a crucial role in organogenesis. Thus, it is extremely important to understand the process of angiogenesis and any abnormalities that may occur during this process.

The next major process of fetal development is neurulation. Neurulation is the process which forms the neural tube, which in turn forms the brain and most of the spinal cord at a later developmental stage [15]. The central nervous system (CNS) is one of the earliest systems to start developing and the last to be completed, after birth. Since the CNS development starts very early on and lasts through the entire pregnancy, this system is extremely vulnerable to the effects of teratogens, *in utero* [16]. The CNS starts to develop as a simple neural plate that folds to form a neural groove and finally closes to form a neural tube. This process of neural tube closure is extremely important and its failure results in neural tube defects, such as spina bifida [17-20]. The process of neural tube closure is one of the most important parts of fetal development as the development of the CNS is entirely dependent on it. Neural tube closure occurs in the first trimester of pregnancy, and appendix A3 of this dissertation details techniques that have been developed as a part of this dissertation to image first trimester exposure to teratogens, particularly the effects on neural tube closure biomechanics.

The end of the first trimester and the start of the second trimester marks the beginning of brain development. During this period, a network of blood vessels in the subarachnoid space give rise to microvessels that invade the fetal brain [21] and the neural stem cells generate most of the neurons of the brain. While appendix A3 focuses on imaging first trimester exposure, a significant portion of this dissertation (chapters 2-4)

focuses on evaluating changes in brain development, particularly angiogenesis, due to exposure to teratogens in the second trimester.

1.2 Imaging embryonic development

Advances in genetic engineering have led to a plethora of genetically manipulated animal models that have revealed the genetic bases for a number of diseases. However, phenotypic information is just as important, but is not well-documented [22-25]. Hence there is a need for noninvasive, rapid, and high-resolution imaging modalities to expand our understanding of embryogenesis and aid the development of effective therapeutics.

Histological staining was one of the first methods used to image embryonic development. It has always been the gold standard for phenotypic analysis, but is invasive, time consuming, and requires a large litter size at each developmental stage. Apart from this, the necessity to fix tissues can significantly alter the gross morphology and appearance of the tissue [26, 27]. Noninvasive imaging modalities can overcome some of these limitations and could potentially perform live imaging of embryos. Consequently, several noninvasive imaging modalities have been used to image embryonic development including confocal microscopy, ultrasound biomicroscopy (UBM), micro-magnetic resonance imaging (micro-MRI), and micro-computed tomography (micro-CT) [28]. However, each has their own set of advantages and disadvantages. Despite its high-resolution capabilities, confocal microscopy is not suited for high-throughput live embryonic imaging because of its insufficient imaging depth and the requirement of fluorescent markers [14, 29, 30]. With a penetration depth of few centimeters, UBM is a powerful imaging technique, but its limited spatial resolution of 30 to 100 μm makes it

unsuitable for imaging fine structures and processes, particularly in early stage embryos. Imaging fine structures, such as microvessels, and processes is very important, especially when imaging small animal embryos, for example, embryonic cardiovascular investigations [31, 32]. Micro-MRI can also achieve similar high spatial resolutions of 25 to 100 μm [33-35]. However, long acquisition times needed for sufficient contrast in thin embryonic tissues (hours) restrict the use of micro-MRI for live embryonic imaging. Although micro-CT offers a high spatial resolution of 2 to 50 μm, the use of external contrast agents and ionizing radiation may be toxic for embryos and hence makes it unsuitable for imaging live embryos and for longitudinal studies [36-38]. Optical projection tomography (OPT) is a relatively new technique for 3D imaging of embryos with very high spatial resolutions of 1 to 10 μm. However, the need for tissue fixation and optical clearing makes it unfeasible for live embryonic imaging [26, 27, 39]. Selective plane illumination microscopy (SPIM) is a technique capable of providing multidimensional, high resolution images of embryos. Although a number of studies have been performed on zebrafish and medaka fish embryos [40, 41], and murine embryos [42], live embryonic imaging using SPIM is difficult as embedding the embryo in agarose is essential to prevent motion of the sample.

In the past decade, optical coherence tomography (OCT) has been developed and used for live 3D imaging of different embryos with high spatial and temporal resolutions. Initially developed for imaging the retina in 1991 [43], OCT is now widely used in clinical ophthalmology [44], and other fields [45]. Due to its ability to provide noninvasive cross-sectional images of a specimen with high spatial and temporal resolutions, OCT is rapidly gaining momentum over other imaging modalities for imaging developing embryos due to

its high speed, noninvasive nature, high spatial resolution, superior contrast, and the rapid development of functional extensions [46-49].

1.3 Optical coherence tomography

OCT is a low coherence interferometric technique capable of label-free, noninvasive, and depth-resolved imaging of tissues with micrometer-scale spatial resolution [43]. Often referred to as the optical analog of ultrasound, OCT uses backscattered light from different layers of the sample to obtain depth-resolved information. Due to the high speed of light, the direct time delay cannot be used to detect backscattered photons from various layers of the sample like in the case of acoustic echoes from ultrasound imaging. Hence, low coherence interferometry (LCI) is used to measure the echo delays between the backscattered light coming from different layers. OCT provides micrometer-scale spatial resolution and an imaging depth of up to 2 millimeters in tissue. Since its introduction, OCT has been used in various fields such as, ophthalmology [50, 51], dermatology [52], cardiology [53, 54], dentistry [55], and cancer imaging [56-58].

1.3.1 Time-domain OCT (TDOCT)

OCT was first introduced as a time-domain system (TDOCT). Figure 1.2 shows a schematic of a TDOCT system. TDOCT is an extension of LCI [59] and was first used to noninvasively image the retina in 1991 [43]. In its basic configuration, light from a broadband source is split and sent to the sample and reference arms in a Michelson-type

interferometer. The backscattered light from the sample interferes with the light reflected from the reference arm, which has a known time delay. Due to the low coherent nature of the light, only depth information from the sample that matches the optical path length of the reference arm within the coherence length of the laser source, which is the axial resolution in OCT, is captured. Thus, a complete axial scan (A-scan or A-line) is obtained by translating the reference mirror. The 3D imaging is traditionally accomplished by scanning the beam across the samples in the x and y directions using galvanometer mounted mirrors. The primary disadvantage of TDOCT is long acquisition times due to the motion of the reference mirror needed to get depth information and reduced sensitivity as compared to Fourier domain OCT.

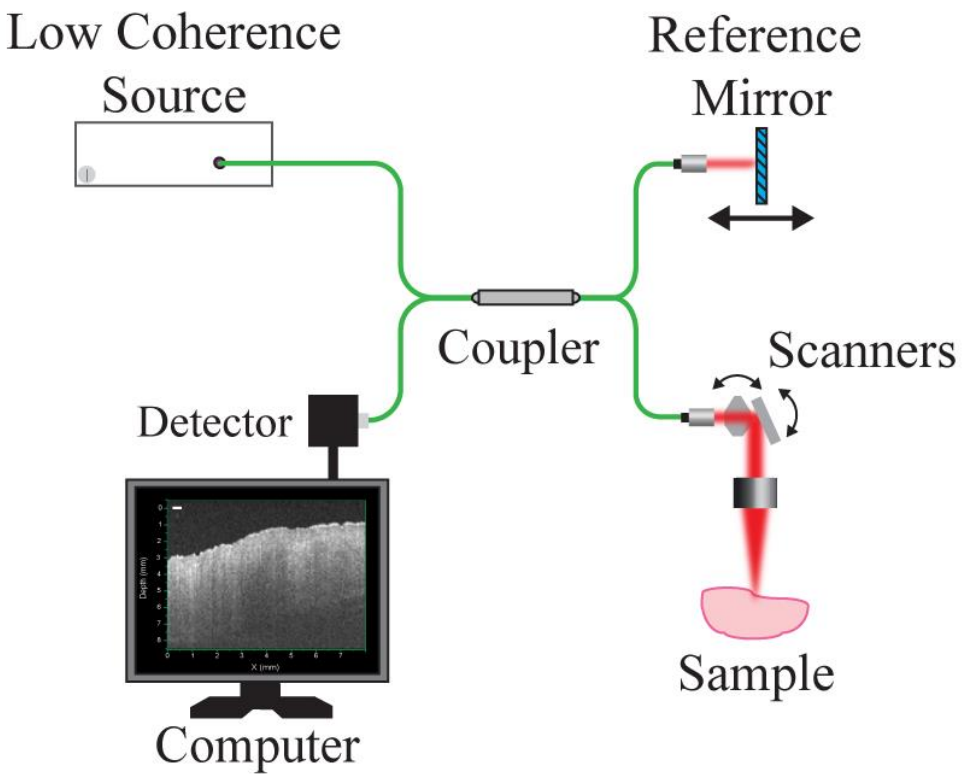

Figure 1.2 Schematic of a typical TDOCT system.

1.3.2 Fourier-domain OCT (FDOCT)

FDOCT was introduced by Fercher et al. in 1995 [60]. FDOCT has several advantages over TDOCT, including a simpler construction, higher speed, and significant signal-to-noise ratio (SNR) improvement [61-63]. FDOCT obtains a single depth-resolved A-scan without modulating the reference arm by capturing spectral information. FDOCT can be further classified into two types: spectral-domain OCT (SDOCT) and swept-source OCT (SSOCT).

1.3.3 Spectral-domain OCT (SDOCT)

An SDOCT system is like a TDOCT system, where the light source is split and sent to the sample and the reference arms, and the backscattered light from the sample and the reflected light from the reference arm interfere. Instead of a photodetector in the case of a TDOCT, a spectrometer (most commonly a combination of a diffraction grating, focusing lens, and CCD array) is used to capture the spectrum of the interference pattern. A single A-scan is obtained by performing a Fourier transform on the spectrally encoded interference pattern. Thus, in SDOCT, an entire depth-resolved A-scan is obtained at once, which is unlike TDOCT where depth information is obtained by scanning the reference arm. The most commonly used light sources in SDOCT systems are superluminescent diodes. These are readily available in several central wavelengths, bandwidths, and power ranges. Compared to traditional SSOCT systems (described in the next section), SDOCT systems are of lower costs, are much simpler, and have superior intrinsic phase stability. Figure 1.3 shows a schematic of a SDOCT system.

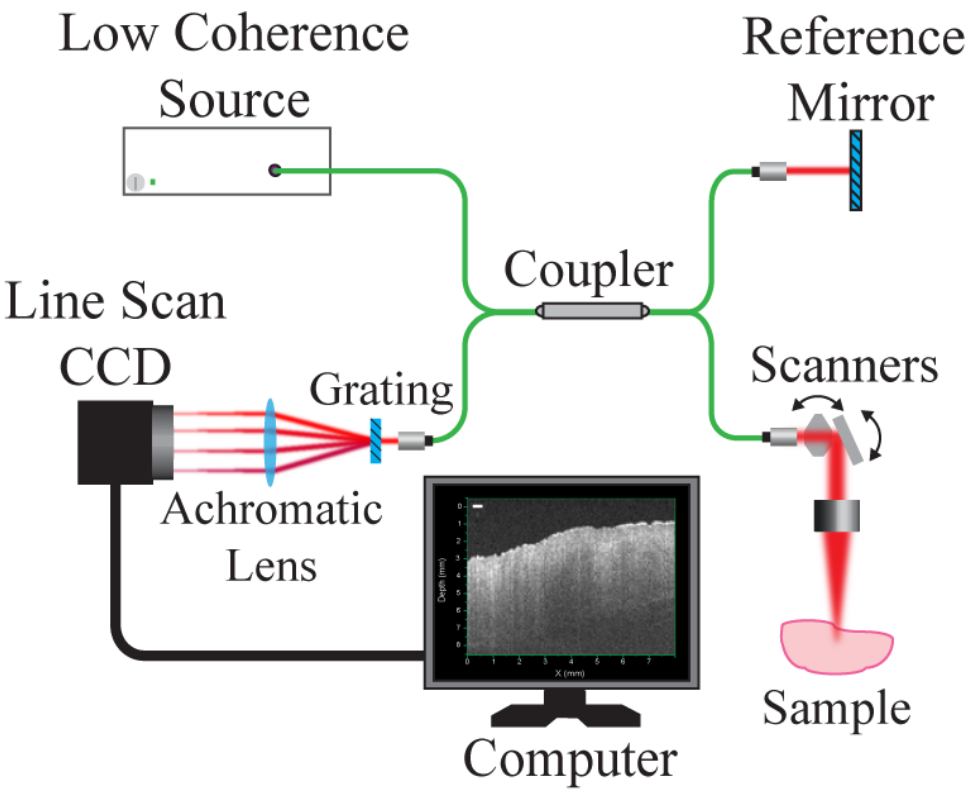

Figure 1.3 Schematic of a typical SDOCT system.

1.3.4 Swept-source OCT (SSOCT)

SSOCT systems utilize a swept-source laser, which sweeps through multiple wavelengths over time. Instead of using a spectrometer to obtain the spectrum of the interference pattern, an SSOCT system uses a balanced photodetector. Since the laser sweeps through the different wavelengths over time, the spectral information is encoded in time, rather than in space as in the case of an SDOCT system. The A-scan, in the case of SSOCT, can be reconstructed by performing FFT on the fringe, exactly the same as in SDOCT. SSOCT systems are capable of imaging much faster when compared to traditional point-scan SDOCT systems. Studies with A-scan rates of 30 MHz and even 100 MHz have been reported [64, 65]. These high imaging speeds have enabled volumetric imaging at

video rates greater than 30 volumes per second [66]. Recent studies have used ultrafast detectors, thus performing very large imaging volumes (up to meters^3), while maintaining the micrometer-scale spatial resolution. Since most systems use light sources of higher central wavelengths, deep tissue imaging is one of the main advantages of SSOCT. Due to the necessity of synchronization between the source and the detector, jitter can limit the phase stability of an SSOCT system compared to SDOCT systems. Over the years several techniques have been used to reduce this jitter including the use of a fiber Bragg grating (FBG), which enabled optical synchronization instead of electronic synchronization [67, 68]. Figure 1.4 shows a schematic of a SSOCT system.

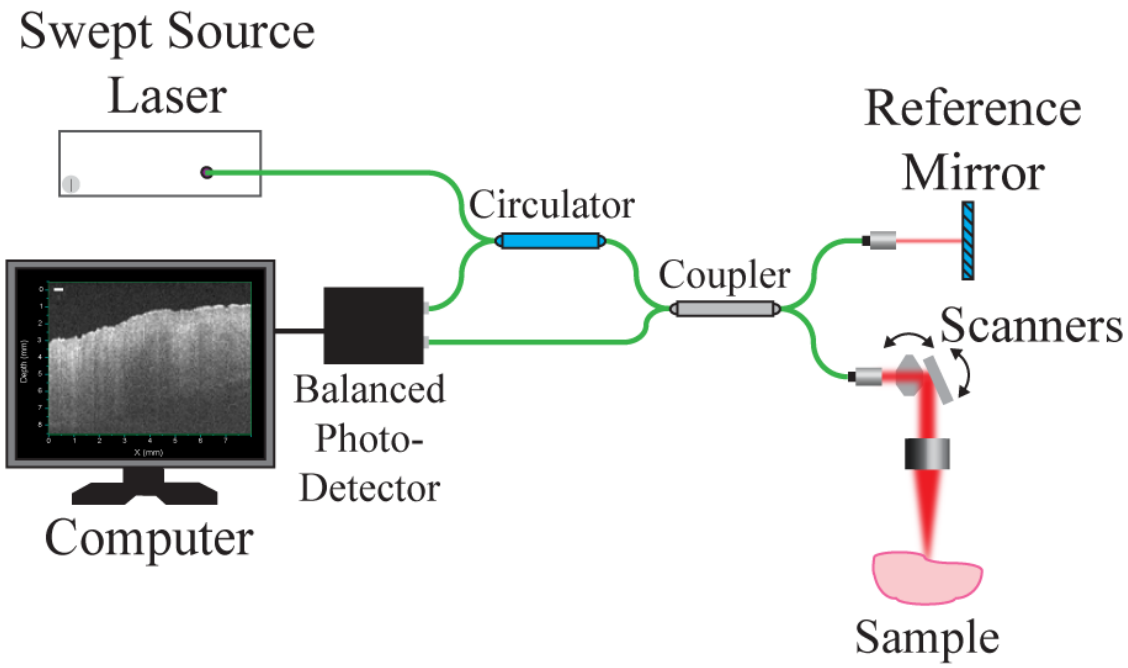

Figure 1.4 Schematic of a typical SSOCT system.

1.4 OCT for embryology: Progress over the years

OCT has shown immense potential for embryonic imaging mainly due to its ability to perform noninvasive depth resolved imaging, rapid acquisition speeds, and high spatial resolutions. Over the years, several functional extensions of OCT have been developed to extend its use from mere structural imaging to functional imaging. Some examples include, Doppler OCT [69, 70], optical coherence elastography (OCE) [71, 72], polarization sensitive OCT (PSOCT) [73, 74], second harmonic OCT [75], and angiographic OCT [76, 77]. While a detailed account of the use of different types of OCT and the use of different functional extensions of OCT in embryology can be found in Raghunathan et al. [78], this section of the dissertation will focus on a summary of the progress in use of OCT for embryology over the years and will conclude with an explanation of angiographic OCT, which is mainly used in this dissertation.

1.4.1 TDOCT

Early investigations with OCT involved studying morphological changes in *Rana pipiens, Branchydanio rerio*, and *Xenopus laevis* [79]. These initial investigations were performed using a TDOCT system. Cross-sectional OCT images of *R. pipiens* tadpoles were compared to histological sections and showed the potential of OCT as a tool for noninvasive “optical biopsy” of embryos. Sequential imaging of a developing zebrafish was performed over time along the same cross-section, proving that OCT is capable of longitudinal in vivo imaging. The ability of OCT to distinguish between normal and abnormal morphology was also demonstrated by comparing OCT images of normal and abnormal *X. laevis* to corresponding histological sections [80]. These early investigations

showed that OCT imaging eliminated the need to sacrifice the embryos for analysis and was less time consuming than standard histological sectioning [81, 82].

Although several imaging modalities were available to image the adult heart, tools to study the developing embryonic cardiovascular system, *in vivo*, were not well-developed. OCT overcame the limitations of other imaging modalities and proved to be capable of noninvasively investigating the structure and function of *in vivo* embryonic hearts with high spatial and temporal resolution. OCT was first used for imaging the developing cardiovascular system by Boppart et al. [83]. In this study, *in vitro* and *in vivo* investigations were performed. In order to reduce the acquisition time, several different modifications were made to the system. The limitations of this study opened avenues for the assessment of other cardiac parameters such as cardiac output and flow velocity through the obtained optical measurements. Subsequent studies worked on different technological advancements as well as other quantifications to analyze cardiac development [84-89].

As mentioned earlier, since blood flow plays a major role in several developmental processes [90-93], understanding blood flow velocities during development was hypothesized to reveal the basis of various diseases and defects. For this purpose, Doppler OCT, a novel functional extension of OCT was introduced in 1997 [69, 70, 94]. Over the next few years, several advancements were made to combat every limitation that provided setbacks [95-97]. One such important advancement was the introduction of gated imaging. Due to the longer acquisition times of TDOCT systems, motion artifacts appeared during functional imaging of the heart. Gating was introduced to minimize these artifacts. Defined as image acquisition synchronized to the heart cycle, gated cardiac imaging was able to provide sufficient data to produce 3D images of the beating heart without motion artifacts,

thus helping in evaluating and analyzing parameters, such as ejection fraction and stroke volume [98, 99]. Lastly, TDOCT was also used in the phenotyping of transgenic embryonic murine hearts [100].

1.4.2 FDOCT

The sensitivity and speed of OCT was significantly increased with the introduction of FDOCT [61-63]. This facilitated the use of OCT for embryonic imaging in several animal models ranging from worms to zebrafish to mice.

The first use of SDOCT in embryology was in 2008, to perform the first *in vivo* 3D imaging of zebrafish embryos [101]. This investigation showed the potential of SDOCT to perform longitudinal studies and distinguish developmental defects in mutants, demonstrating the potential of OCT to detect developmental changes at a microstructural level. SDOCT was also used to image developmental defects in zebrafish embryos due to ethanol exposure [102]. The first multimodal imaging of embryos involving OCT was demonstrated by Bradu et al. [103]. In this study, SDOCT was combined with laser scanning fluorescence microscopy (LSFM). While SDOCT provided depth-resolved structural information at once, LSFM was used to collect fluorescence emission from a broad depth. Complementary information from both the techniques provided more specific and sensitive information. As in the case of TDOCT, several advancements were made in the subsequent years in terms of optics [104], using functional extensions of OCT [105], quantifying parameters [106-111], and techniques to accommodate the new parameters for quantifications [112]. SDOCT was used for differentiating between mutants and controls

[113] like TDOCT and was also used for new applications such as image-guided microinjections [114].

First studies of embryonic development using SSOCT were performed in 2009, where 3D structural imaging of live embryos at different stages were performed [115]. In 2011, the first *in utero* imaging using SSOCT was performed [116]. This provided a way to image live embryos at later stages of gestation using OCT. Using this protocol, the development of several different organs was studied including the limbs, eye [117, 118], and most importantly the brain. This method of brain imaging was used for the first time to show the effects of ethanol exposure on the developing brain using OCT [119]. Similar to TDOCT, and SDOCT, functional extensions like Doppler OCT [120, 121], and speckle variance OCT [122, 123] were also developed for SSOCT. In addition to technological advancements such as the use of Fourier domain mode-locked lasers to provide ultrahigh-speed imaging [66, 124-130], several different post processing algorithms were also introduced to improve image acquisition and to produce higher quality images [131-133]. New techniques to broaden the application of OCT to image developing embryos were also proposed. One such example was rotational imaging optical coherence tomography (RI-OCT) [134], where 3D structural imaging was performed at four different angles with an interval of 90 degree between each angle. The images from the different angles were combine during post processing. This eliminated the problem of insufficient imaging depth at certain gestational stages due to light attenuation.

The next section of this chapter discusses angiographic OCT, which is the main technique used in the work presented in this dissertation.

1.4.3 Angiographic OCT

Angiographic OCT is a functional extension of OCT used to visualize blood vessels [77, 135]. The main principle behind angiographic OCT is to use the variation in signal caused by moving particles in the blood to provide contrast (motion contrast) for imaging [76, 136]. For example, when imaging any organ or tissue with blood flow, there are two types of OCT signals obtained. One is the signal obtained due to backscattering from the static tissue (structural tissue) and the other is obtained due to backscattering from the moving particle. When imaged over time, the signal from the structural tissue remains the same as it is stationary. However, the signal from the moving particles changes over time. Hence, during imaging, multiple images are recorded over time, at the same spatial position. The temporal changes in the OCT signal caused by the moving particles provide the contrast for the angiographic OCT image, hence aiding in isolating the vasculature from the background tissue.

As mentioned earlier, the OCT signal is obtained by performing a fast Fourier transform on the spectral interference pattern. Thus, the OCT signal is a complex signal (after Fourier transform), and hence, is composed of amplitude or intensity information and phase information. Depending on which of these components is used, angiographic OCT can be divided into three categories:

1. Intensity signal-based angiographic OCT (Example: speckle variance OCT)
2. Phase signal-based angiographic OCT (Example: Phase variance OCT)
3. Complex signal-based angiographic OCT (Example: correlation mapping optical coherence angiography)

Of these, this dissertation uses two types of angiographic OCT: a) intensity signal-based speckle variance OCT (SVOCT), and b) complex signal-based correlation mapping optical coherence angiography (cm-OCA).

1.4.4 Speckle variance OCT (SVOCT)

SVOCT was introduced to overcome the main disadvantage of Doppler OCT, which was the Doppler angle dependency and hence insensitivity to flow in a direction perpendicular to the scanning beam [137]. Speckle is a random interference pattern cause by light from mutually coherent sources with random phases that have been scattered multiple times [138]. Since speckle is a random phenomenon, it is usually described by its statistical properties. Speckle appears as bright and dark spots and has mostly been considered a source of noise as it tends to degrade the contrast of an image. However, speckle can also be used to provide information about tissue structure and flow [138-140].

Since speckle arising from dynamic scatterers decorrelates faster than speckle arising from static scatterers, by calculating the variance between several OCT images recorded in the same spatial position over time, tissue microvasculature can be mapped using a simple algorithm:

$$SV_{i,j} = \frac{1}{N}\sum_{t=0}^{N-1}(I_{i,j,t} - I_{i,j,mean})^2, \quad (1)$$

where $SV_{i,j}$ is the variance at the pixel *(i, j)*. $I_{i,j,t}$ is the structural image intensity at pixel *(i, j)* at time *t*. $I_{i,j,mean}$ is the mean of intensity values at pixel *(i, j)* of all N values. SVOCT is sensitive to both transverse and axial components of blood flow, unlike Doppler OCT.

1.4.5 Correlation mapping OCA (cm-OCA)

With a concept similar to SVOCT, correlation mapping OCT is a technique that calculates the correlation coefficient between multiple B-scans at the same location. Flow regions show lower correlation coefficient compared to the static regions that show higher values, hence distinguishing microvasculature from tissue. Correlation based methods, like SVOCT, are sensitive to the mobility of scatterers and less sensitive to the Doppler angle. Methods based on both intensity and complex signal have been used. However, methods based on the complete complex information have provided superior vasculature contrast as the correlation coefficient calculated becomes less sensitive to environmental motion [141, 142]. Despite these advantages, complex correlation-based OCT, still suffers from two major problems: a) reduced SNR, and b) variance of the estimated complex correlation coefficient due to low SNR. For example, just like motion, low SNR can also lead to a low correlation coefficient, hence depicting high flow signal. To solve this problem several studies have used intensity-based methods to remove the low SNR regions. However, above the set intensity threshold, this problem still persists. Variance of the estimated correlation coefficient, dependent on the changing SNR, is another factor that can reduce the contrast of the vasculature maps. This is a problem that could arise due to involuntary sample motion during live imaging that causes decorrelation and artifacts.

To overcome these disadvantages, Makita et al. [142], in 2016, proposed cm-OCA, in which the signal was derived using the SNR-corrected low-noise complex correlation. The computed correlation values were independent of the SNR decay along depth. In addition, complex averaging was used to mitigate the motion effects and hence higher angiographic contrast was achieved when compared to intensity-based methods.

The imaging procedure is similar to SVOCT, where a spatial position is scanned multiple times and the average temporal correlation is calculated instead of the variance. The SNR-dependent artifacts are corrected using temporal variance of the background noise. The work in the dissertation followed a similar algorithm to Makita et al. [142] for cm-OCA and Sudheendran et al. [122] for SVOCT. More information on the exact procedure followed in this work can be found in the section titled "Imaging, quantifications, and statistics" in each of the individual chapters.

1.5 Prenatal substance abuse

As mentioned earlier, the process of embryonic development is highly vulnerable to the effects of teratogens. While the fetus can be exposed to teratogens in different ways, one of the most common ways is prenatal substance abuse. Prenatal substance abuse is a major public health concern [143]. In the United States, the most commonly abused substance is nicotine, followed by alcohol, cannabis, and other illicit substances [144, 145]. Most of these drugs are known to cross the feto-placental barrier and hence is known to cause detrimental effects not only to the mother but to the developing fetus as well [146]. The effects of several different drugs on the human fetus has been studied for many decades now. For example, the effects of prenatal cigarette use have been studied since the 1960s [147], the effects of ethanol and opiate use has been studied since the 1970s [148-150], and the effects of various other illicit drugs have been studied since the 1980s [151-153].

In the United States, 40% of women are known to live with a lifetime drug use disorder [154]. Most importantly, women in their reproductive years (18-44), especially between the ages of 18-29 are more susceptible to developing a substance abuse disorder

[155]. This combined with the prevalence of unplanned pregnancies in the United States, increases the risk of prenatal substance abuse. In 2012, 8.5% of pregnant women reported alcohol use, 15.9% reported cigarette smoking, and 5.9% reported the use of illicit substances. This resulted in a total of 380,000 babies being exposed to illicit substances, over 550,000 being exposed to alcohol, and over one million exposed to tobacco *in utero*. Similar patterns were seen in other regions like Europe [156] and Australia [157]. As far as low- and middle-income countries are concerned, there is relatively less information on the prevalence of substance abuse during pregnancy. The overall prevalence of tobacco use in such countries was reported to be 2.6%, with some countries having higher rates of up to 15% [158]. Although information is scarce, according to the World Health Organization, cannabis is the most commonly abused substance in these countries. The prevalence of alcohol use in South Africa is 19.6% and the prevalence of illicit drug use is anywhere in between 3.6 and 8.5% [159].

Several studies have reported that some pregnant women have quit their substance abuse during pregnancy after learning about the harmful effects it can have on the fetus [160]. However, this is offset by the increase in rates of relapse, postpartum [161]. Unfortunately, most of these drugs are also known to pass through breast milk, thus increasing their chances of exposure even after birth. The human brain is not fully developed until well into adolescence, thus, a relapse into drug abuse postpartum, definitely poses significant harm to the developing brain.

The different effects that have been reported due to individual drugs have been described in the respective chapter introductions.

1.6 Organization of the rest of this dissertation

Most of this dissertation (chapters 2-4) has been divided based on the different teratogens that have been studied.

Chapter 2 shows the acute effects of maternal exposure to alcohol on developing fetal brain vasculature evaluated using *in utero* angiographic OCT. The results presented in this chapter, starts of with a single dose study that was initially tested to simulate binge drinking. Then, a dose response curve is plotted to show the effects of two other doses of alcohol. Finally, angiographic OCT was also used to distinguish between the changes in the vasculature of the mother and the baby simultaneously after maternal exposure to ethanol.

Chapter 3 depicts results from prenatal exposure to nicotine. Similar to chapter 2, acute changes in developing fetal brain vasculature was evaluated when the mother was administered pure nicotine. Again, first set of results shown are from a dose of 1 mg/kg that is known to cause intrauterine growth restriction in the fetus. This was followed by results from a lower dose (0.1 mg/kg). This dose is equivalent to what is achieved by an average human smoker.

Chapter 4 shows results from synthetic cannabinoid studies. Since this is a relatively new area of research, as of now, we have tested only one dose of the synthetic cannabinoid CP-55,940.

Chapter 5 summarizes the work of the first part of this dissertation along with a discussion of future work and limitations.

The second part of this dissertation is described in Appendix A3. This part demonstrates the use of OCT, combined with another optical imaging modality called

Brillouin microscopy to evaluate stiffness changes in a developing fetus. The final goal of this work is to image changes in fetal development caused due to exposure to teratogens in the first trimester. This section summarizes results from two studies performed to evaluate changes in stiffness of fetal tissue as the fetus develops.

Chapter-2 Assessing alcohol induced fetal brain vasculature changes

In this chapter, acute changes in murine fetal brain vasculature caused by prenatal exposure to ethanol were assessed using *in utero* angiographic OCT. A home-built SS-OCT system was used to image the fetal brain and a post processing algorithm was used to create the vasculature maps. Results showed a significant decrease in vessel diameter minutes after maternal ethanol consumption, suggesting a possible decrease in blood flow to the developing brain during the peak period of fetal neurogenesis and angiogenesis. A dose response curve is plotted depicting results from two other doses of ethanol. Finally, acute vasculature changes that occur in the mother are compared to the changes that occur in the fetus when the mother is administered ethanol.

2.1 Introduction

No amount of alcohol is considered safe during pregnancy. Despite this being a constant warning, alcohol consumption during pregnancy is common. Prenatal exposure to alcohol, in any amount, is known to significantly damage the developing fetus and cause congenital defects. In 1973, fetal alcohol syndrome, was an official term given to a group of defects caused by exposing the developing fetus to alcohol [149]. Since then, research has shown that prenatal exposure to alcohol causes a broad range of developmental defects and was then given a general name. Fetal alcohol spectrum disorders (FASD) refers to a range of abnormalities caused by prenatal alcohol exposure (PAE) [162]. This includes physical, behavioral, and cognitive defects. The neurocognitive and behavioral problems are known to be lifelong issues. Early detection, diagnosis, and therapy have resulted in improved outcomes. Some of the different diagnoses under FASD include:

1. Fetal alcohol syndrome (FAS)
2. Partial fetal alcohol syndrome
3. Alcohol-related birth defects (ARBD)
4. Alcohol-related neurodevelopmental disorder (ARND)
5. Neurobehavioral disorder associated with prenatal alcohol exposure (ND-PAE)

The estimated global prevalence of FASD is 22.7 per 1000 births, and regional estimates can vary from 33.5 per 1000 births in the United States to 113.22 per 1000 births in South Africa [163]. In general, 15% of all pregnancies end in spontaneous abortions, but this number is as high as 45% for women who are heavy drinkers [164]. Comparing rates of still birth, the number is said to be six-times greater when exposed to alcohol than the normal population [165]. The severity of the effect depends on a variety of factors, but most importantly, the amount of alcohol consumed and the period of gestation during which alcohol was consumed. Other factors that can potentially increase the severity of the defect include smoking, environmental toxins, and socioeconomic factors [166].

Due to the prevalence of unplanned pregnancies in the United States [167], and binge patterns of alcohol consumption [168], PAE in the first trimester is common. However, many women continue to consume alcohol well into their second trimester of pregnancy [169]. The second trimester marks the peak period for fetal neurogenesis and angiogenesis. The majority of neurons of the adult brain are born during this period [170]. Although PAE has its effects on different organ systems, the CNS is affected the most due to the extent of its developmental period. Thus, in order to understand the effects of PAE on a developing brain, studying second trimester exposure to alcohol is crucial. Several

aspects of brain development after PAE including morphological, behavioral, and cognitive studies are being studied in detail [119, 171-180]. The microvasculature that develops during the second trimester supports the nutritional needs of the developing fetus [21], provide endocrine control of fetal growth [181], and promote neural development [182]. Although several studies have evaluated changes in blood flow after PAE [183, 184], acute changes in fetal brain vasculature have not been well documented.

The work and results in this chapter are divided into three sections:

1. The first section is the pilot study of this work. SVOCT was used to evaluate acute vasculature changes in the fetal brain after maternal alcohol consumption. A single dose of ethanol, which simulated binge-drinking in humans, was used for this study. More details on the dosage is provided in Section 2.2.3. Comparisons are made with vasculature images recorded before maternal ethanol consumption as well as a sham group, where tap water was administered to the mother instead of any ethanol.
2. The second section shows results from dose response studies. Results from the pilot study showed drastic results for the dose that was tested, emphasizing the importance of testing lower doses. Additionally, it has been shown in previous work that exposure to low doses of ethanol can also cause noticeable effects [185]. Hence, we tested two doses of ethanol in addition to the dose tested in the pilot study. A complete description of the doses can be found in section 2.2.3. From this point onwards, the cm-OCA algorithm was implemented for all studies. The advantages of cm-OCA over SVOCT have been explained in section 1.4.5.

3. The final section of the results involves assessing vasculature changes in the mother and the fetus simultaneously. Ethanol can be found in the fetus within a minute after maternal exposure to the teratogen [186]. Maternal and fetal metabolism of ethanol occur through the same pathways [187]. However, understanding of the metabolic capacity of the fetal liver is limited. Nevertheless, the fetal metabolic capacity is only 5 to 10% of adult activity [188]. Hence studying the responses of the mother and the fetus, simultaneously, to the same dose of the teratogen is crucial. Once again, the complete description of the dose used can be found in section 2.2.3.

2.2 Materials and methods

2.2.1 OCT system

Since the same OCT system was used for all the work shown in this dissertation, a complete description of the OCT system used is written in Appendix A1.

2.2.2 Animal manipulations

Except for the teratogen used and the dosing details, the procedure for animal manipulation including the surgical procedure was the same throughout all the studies presented in this dissertation. A complete description of the animal manipulation is written in Appendix A2.

2.2.3 Dosing

The first study simulated binge-drinking episodes in humans. Thus, 16.6% ethanol at a dose of 3 g/kg was administered via intragastric gavage. This dose has been shown previously, in mice, to cause a blood alcohol concentration (BAC) of 117 mg/dl in the mother, which corresponds to the levels achieved by the average non-alcoholic human population during binge-drinking episodes [183]. However, for the second part of the study, the effects of 2 additional doses, 0.75 g/kg and 1.5 g/kg of 16.6% ethanol were evaluated, and the dose response curve was plotted. For the final section of this chapter, where the vasculature of the mother and fetus was analyzed simultaneously, the dose used was similar to the first study of this chapter where a dose of 3 g/kg of 16.6% ethanol was used.

2.2.4 Imaging, quantifications, and statistics

SVOCT images were obtained by an algorithm used in Sudheendran et al. [122]. The cm-OCA images were obtained using the algorithm from Makita et al. [142]. The OCT probe beam was scanned over a small region of the fetal brain *in utero*. The 3D OCT images consisted of 600 B-scans per volume and each B-scan consisted of 600 A-scans. Five B-scans were recorded at each spatial position for reconstructing the vasculature maps. The time for each B-scan was 20 ms, and the total acquisition time was 84 seconds including the galvanometer flyback time between B-scans. As mentioned previously, the variance between the 5 B-scans were calculated in the case of SVOCT, and the correlation coefficient between these 5 frames was calculated in the case of cm-OCA to obtain the vasculature maps.

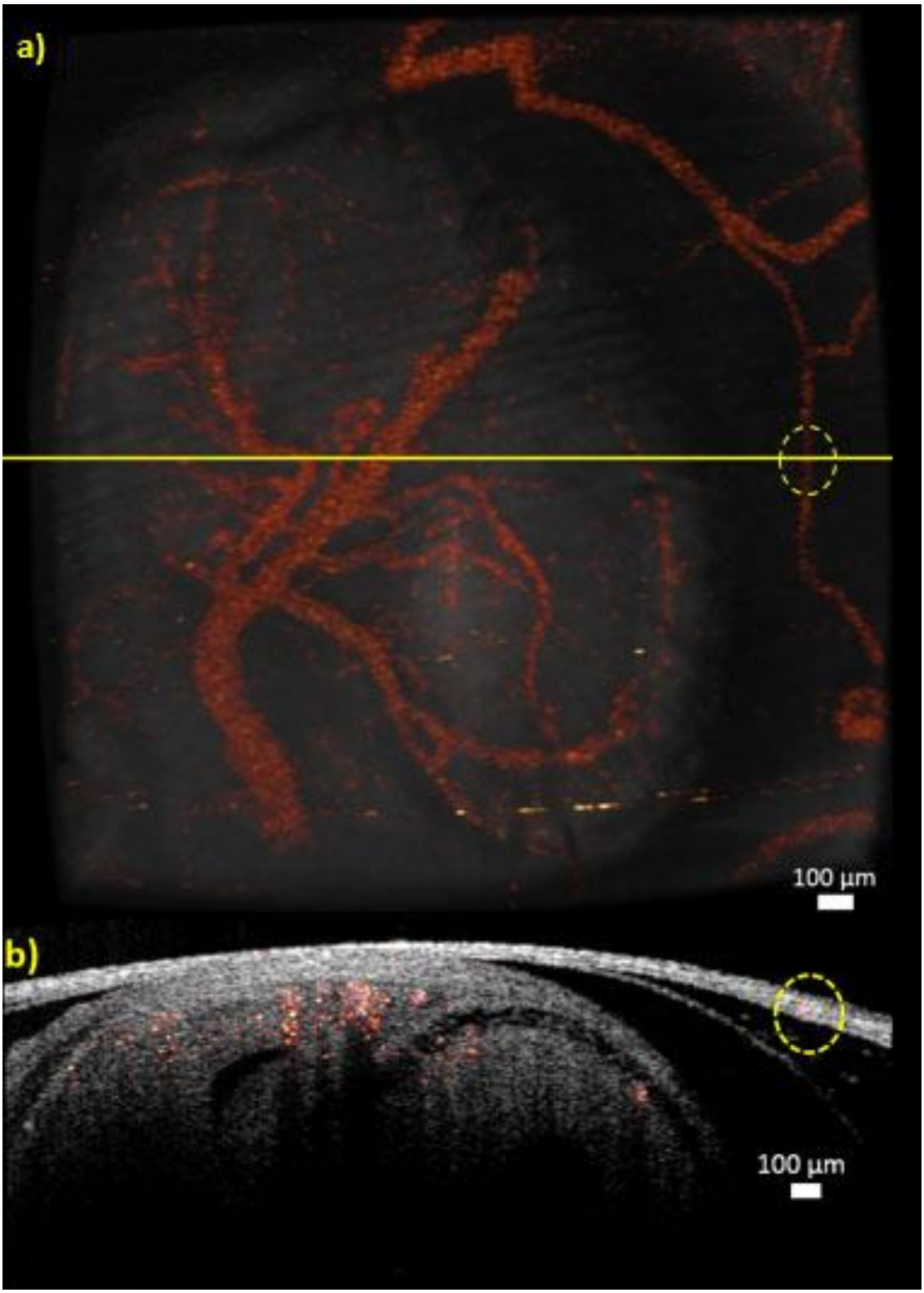

Figure 2.1 (a) 3D structural OCT image overlapped with the 3D SVOCT image, (b) 2D cross-section depicted by the yellow line in (a). The circled region indicates a blood vessel in the uterus.

Figure 2.1 (a) shows an overlay of a 3D structural OCT image with the corresponding 3D SVOCT image. In order to differentiate between the blood vessels in the uterus and the blood vessels in the fetal brain, a cross section of the overlay from figure 2.1(a), depicted by the dotted yellow line, is shown in figure 2.1 (b). From, figure 2.1 (b), the vessels in the top right, depicted by a yellow dotted circle, can be clearly identified as blood vessels on the uterine wall, whereas the vessels on the left are identified as vessels on the fetal brain. This ability to distinguish between vessels on the uterus and the fetal brain ensured that all the quantifications were made on the vessels from the brain only.

An average intensity projection (AIP) was performed along the axial dimension of the 3D SVOCT images. This provided an *en face* view of the vasculature in the fetal brain, yolk sac, and the uterus of the mother. AIPs were utilized only for the first study, where SVOCT was used. For all the remaining studies that used cm-OCA, maximum intensity projections (MIP) were obtained. In the case of SVOCT images alone, a bulk motion artifact correction was performed during SVOCT postprocessing. The average SVOCT intensities at each B-scan position were plotted to identify B-scans that were affected by bulk motion. A threshold value was selected, and any B-scan with an average SVOCT value greater than this threshold was replaced with the previous SVOCT B-scan, assuming that there was sufficiently high spatial sampling between adjacent B-scans [189]. A complete description of the bulk motion reduction algorithm used for the cm-OCA images can be found in section 3.2.4 of this dissertation.

All the quantifications were performed on the AIP/MIP images. Matlab (MathWorks, Natick, MA, USA) was used to implement the SVOCT and cm-OCA algorithms. Amira (EFI Co., Portland, OR) was used to denoise the images and to perform

quantifications for the studies shown in this chapter. For the alcohol studies, vessel diameter (VD) quantifications were made.

For the SVOCT images alone, the quantifications were performed using Matlab. However, as mentioned earlier, the denoising was conducted in Amira. For the SVOCT quantifications, a hessian filter-based approach was used to enhance the contrast and connectivity of the blood vessels in the 2D projection (Hessian based Frangi Vesselness filter, Dirk-Jan Kroon, MathWorks File Exchange, MathWorks, Natick, MA, USA). The output was thresholded by a binary mask and the vessel diameter was calculated using Matlab.

For the first part of this study, where a single dose (3 g/kg) was tested, a nonparametric Friedman test of differences was conducted on each sample to assess statistical significance of the changes in vessel diameter over time. Then a 2-sided Mann-Whitney *U* test was performed to evaluate if there was a statistical significance in the percentage change of vessel diameter between the ethanol and sham groups at 45 minutes post maternal exposure.

For the dose response studies, a nonparametric Kruskal-Wallis ANOVA was performed to assess the effects of different doses on the vasculature. This was followed by a 2-sided Mann-Whitney *U* test, that was performed to test for statistically significant changes between every ethanol group and the sham group (3 pairs), and between the three ethanol groups (3 pairs). Thus, there were a total of 6 pairs that was tested. Bonferroni correction was included in this case for multiple pair-wise tests.

2.3 Results

2.3.1 Single binge-like bolus exposure

This first section of the results focuses on the effects of a single binge-like exposure to ethanol on the fetal brain vasculature. A dose of 3 g/kg of 16.6% ethanol was used for this study.

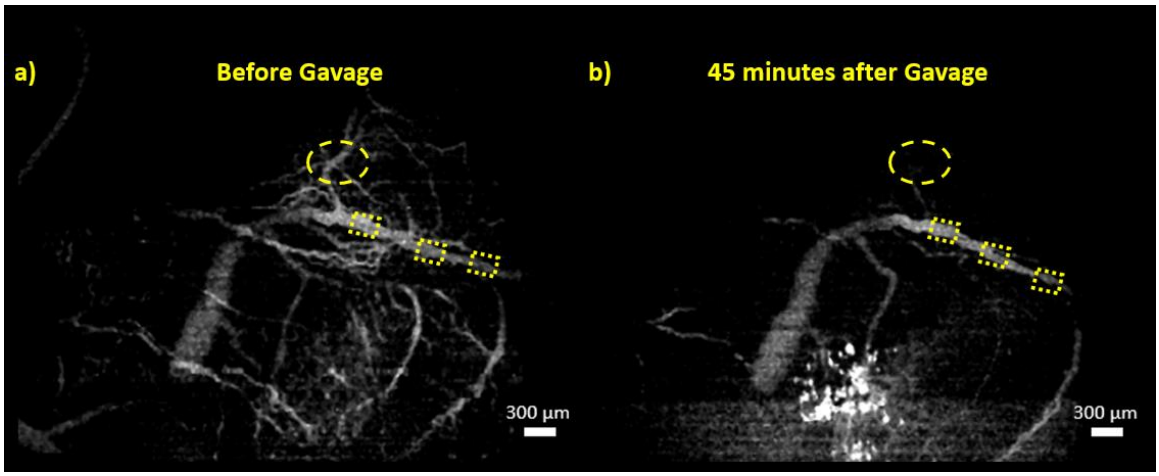

Figure 2.2 (a) 2D MIP of the SVOCT image of the fetal brain vasculature before intragastric gavage with water. (b) 2D MIP of the SVOCT image of the fetal brain vasculature after intragastric gavage with water. The dotted circle shows the gradual disappearance of smaller tributaries.

Results from one fetus each from the sham and ethanol groups are shown in figures 2.2, and 2.3 respectively, followed by results from 3 fetuses of 3 different mothers from each of the sham and ethanol groups, shown in figure 2.5. Changes in VD were quantified at three different locations on the main vessel to ensure consistency in results. The data presented here is represented as percentage change in VD at every time point after gavage with the measurement taken before gavage as the reference.

Figures 2.2 (a) and (b) show AIPs of 3D SVOCT images of fetal brain vasculature before and 45 minutes after gavage with tap water respectively, while figures 2.3 (a) and (b) show AIPs of 3D SVOCT images of fetal brain vasculature before and 45 minutes after gavage with ethanol respectively. Results show a drastic reduction in vasculature after maternal consumption of ethanol which is not seen in the case of the sham group.

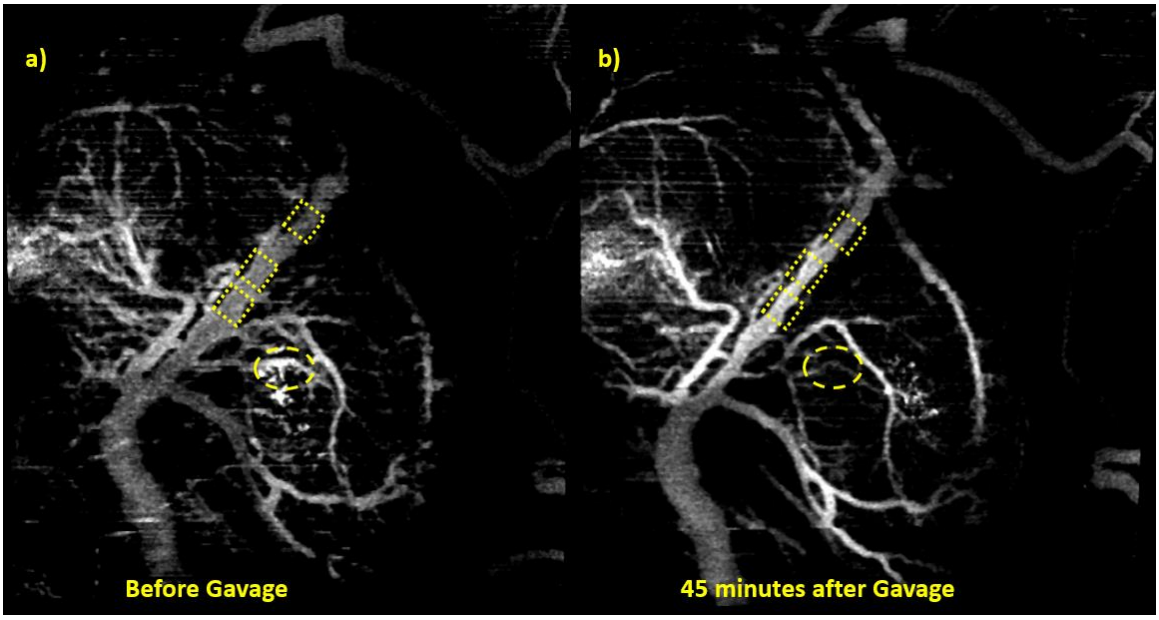

Figure 2.3 (a) 2D MIP of the SVOCT image of the fetal brain vasculature before intragastric gavage with ethanol at a dose of 3 g/kg. (b) 2D MIP of the SVOCT image of the fetal brain vasculature 45 minutes after intragastric gavage with ethanol at a dose of 3 g/kg.

Figure 2.4 (a) depicts the percentage change in VD for a period of 45 minutes after gavage with tap water (sham group) at 5-minute intervals, whereas figure 2.4 (b) depicts the percentage change in VD for a period of 45 minutes after gavage with ethanol at 5-minute intervals. The mean of the median values of percentage change in VD at each time point for the sham group was 3.0%±1.9%. For the ethanol group, at 5 minutes after ethanol exposure, the percentage change in VD was 2.0% which increased to 31.9% at 45 minutes post maternal ethanol exposure.

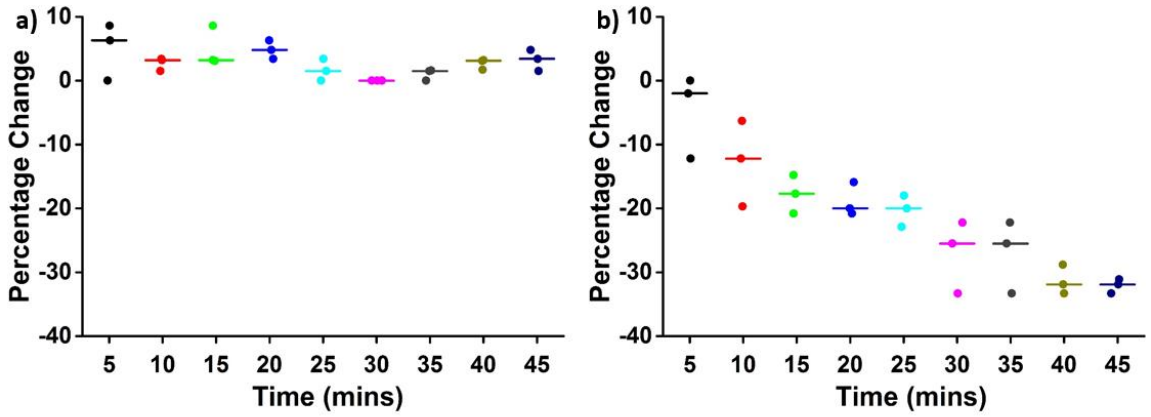

Figure 2.4 Percentage change in vessel diameter after administration of (a) water, and (b) ethanol at a dose of 3 g/kg, every 5 minutes for a total period of 45 minutes with the pre-gavage measurement as the reference. The line depicts the interposition median, and the raw data is plotted alongside.

The bright white spots seen on both the figures 2.2 and 2.3 are due to dehydration of the uterine tissue. The tissue was not hydrated due to the possibility of the saline interfering with the effects of ethanol. The sham group was not hydrated also to maintain consistency. However, for all the studies following this one, the tissue was hydrated one minute before every measurement for the teratogen as well as the respective sham group with 1x PBS.

Table 2.1 Summary of the Friedman ANOVA results performed on all samples. The degrees of freedom for all tests were 8.

	Sham group			**Ethanol group**		
	Sample 1	Sample 2	Sample 3	Sample 1	Sample 2	Sample 3
$\chi 2$ value	12.31	6.53	11.26	22.37	23.46	16.44
Significance	P = 0.137	P = 0.587	P = 0.187	P = 0.004	P = 0.003	P = 0.036

Table 2.1 summarizes results from the Friedman ANOVA performed on all samples. All samples from the ethanol group showed statistically significant changes over time whereas the samples from the sham group did not.

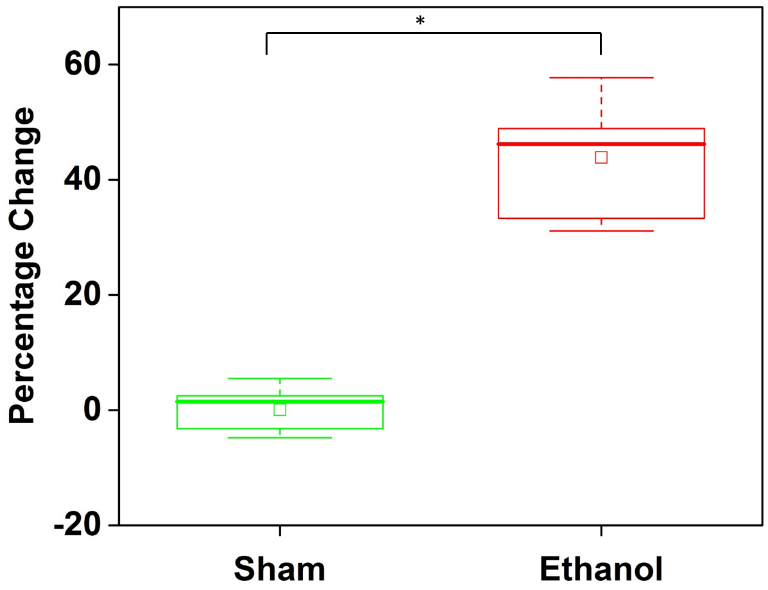

Figure 2.5 Percentage change in vessel diameter 45 minutes after administration of water and ethanol (dose: 3 g/kg) by intragastric gavage. The asterisk indicates P < 0.001 by a 2-sided Mann-Whitney *U* test.

Figure 2.5 shows a summary of all results from all samples (n = 9 measurements for each group) at 45 minutes post-exposure. The box represents the interquartile range,

the whiskers are the standard deviation and the inscribed hollow squares represent the mean of the data distribution. The Mann- Whitney *U* test showed a statistically significant difference between the ethanol and the sham groups ($n_1 = n_2 = 9$, $U = 0$, ($P = 4.12 \times 10^{-4}$, $P < 0.001$)).

2.3.2 Dose response analysis

Ethanol in the same concentration (16.6%), at two other doses of 0.75 g/kg and 1.5 g/kg were tested in this study. Figures 2.6 and 2.7 show results from one fetus from each of the additional doses evaluated.

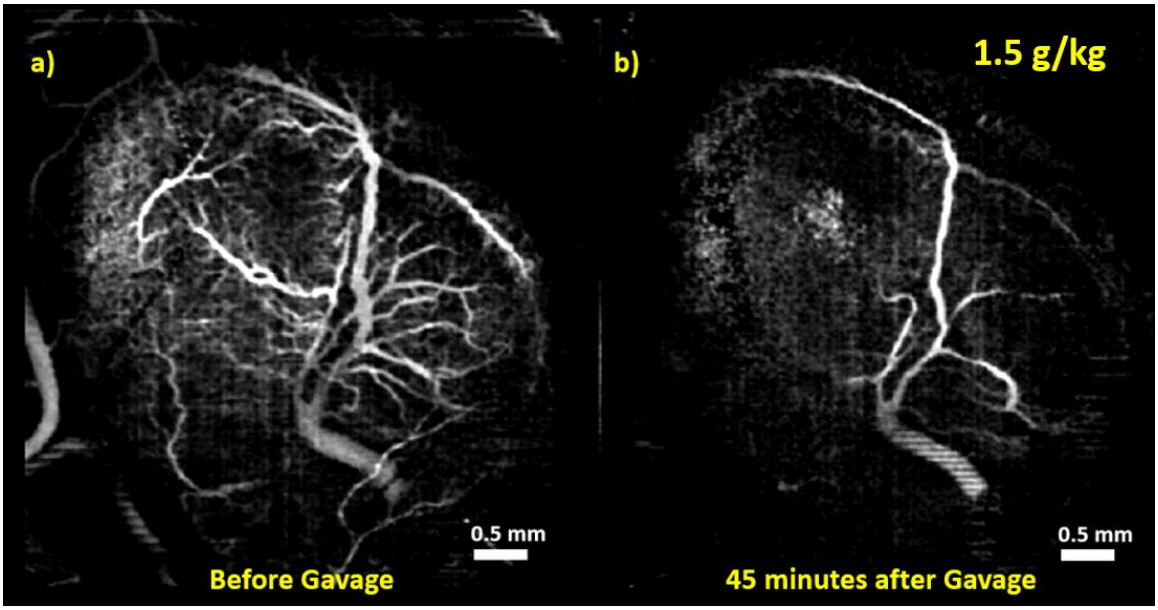

Figure 2.6 2D MIP of cm-OCA images of fetal brain vasculature (a) before, and (b) 45 minutes after maternal exposure to ethanol at a dose of 1.5 g/kg.

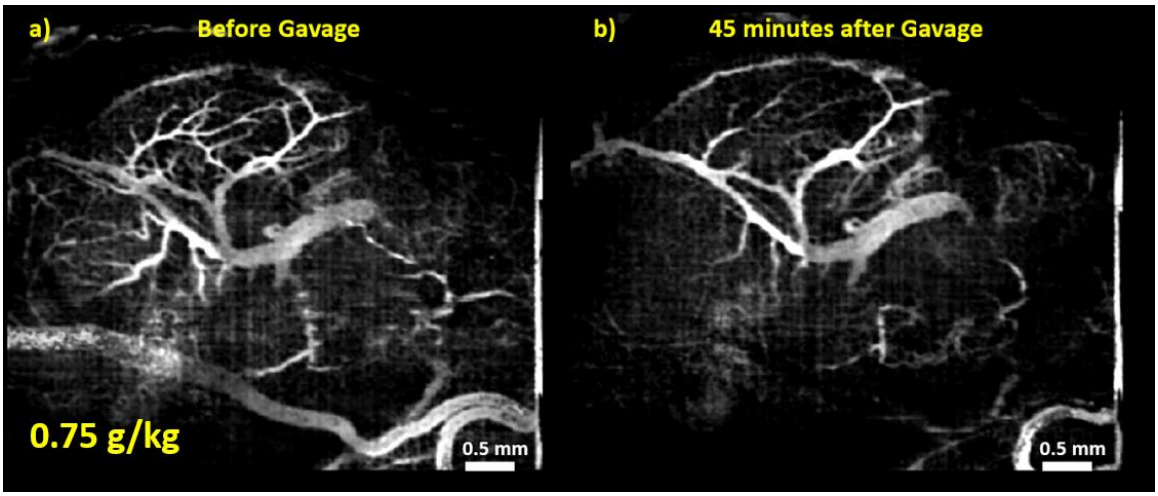

Figure 2.7 2D cm-OCA images of fetal brain vasculature (a) before and (b) 45 minutes after maternal exposure to ethanol at a dose of 0.75 g/kg.

Figures 2.6 (a) and (b) show MIPs of 3D cm-OCA images of fetal brain vasculature before and 45 minutes after gavage respectively with ethanol at a dose of 1.5 g/kg, while figures 2.7 (a) and (b) show MIPs of 3D cm-OCA images of fetal brain vasculature before and 45 minutes after gavage respectively with ethanol at a dose of 0.75 g/kg. Both showed a reduction in vasculature. These results were quantified to compare with the dose of 3 g/kg. Results of the dose 3 g/kg (shown in section 2.3.1) was reprocessed using the cm-OCA algorithm for comparison purposes.

Figure 2.8 shows the dose response results. As expected, the effects of the lower doses are considerably less when compared to 3 g/kg. These results were also compared to the sham group (tap water). 'LR' on the plot refers to experiments performed with lactated Ringer's instead of ethanol or tap water. These experiments were done to test the

differences between the effects of tap water and Lactated Ringer's as the sham group for future studies.

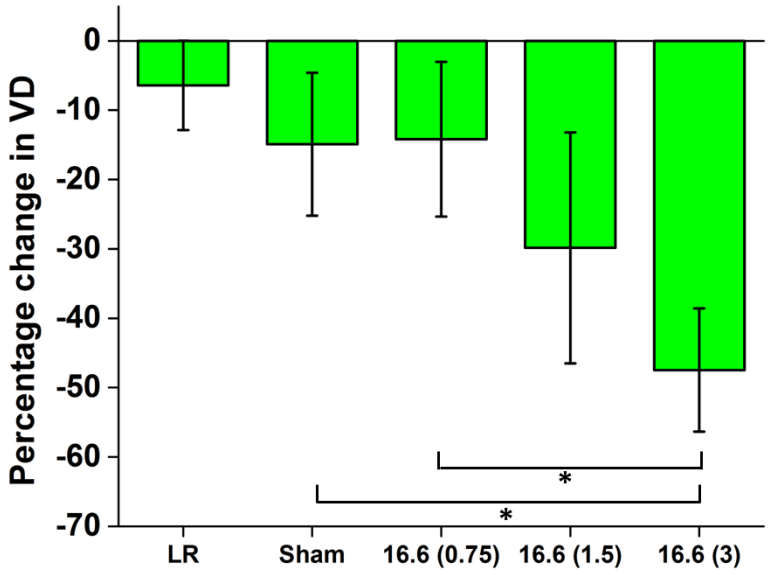

Figure 2.8 Percentage change in VD 45 minutes post maternal exposure to water, lactated Ringer's (LR), and 16.6% ethanol at doses 0.75 g/kg, 1.5 g/kg, and 3 g/kg. The asterisk indicates $P < 0.001$ using a 2-sided Mann-Whitney *U* test.

The Kruskal-Wallis ANOVA showed a statistically significant difference between the six groups. The 2-sided Mann-Whitney *U* test was performed between each of the groups (6 pairs in total) for pairwise testing. A statistically significant difference was found between the sham group and the ethanol group at a dose of 3 g/kg and between the ethanol groups at a dose of 0.75 g/kg and 3 g/kg. Table 2 shows the results from the 6 pair-wise Mann-Whitney *U* test. P values in bold indicates statistical significance after Bonferroni correction for multiple tests.

Table 2.2 Summary of the Mann-Whitney *U* tests. P values in bold indicates statistical significance.

	n1	**n2**	**U**	**p**
Sham vs 0.75 g/kg	18	15	124	0.7
Sham vs 1.5 g/kg	18	12	167.5	0.01
Sham vs 3 g/kg	18	9	160	**5.38×10^{-5}**
0.75 g/kg vs 1.5 g/kg	15	12	141	0.013
0.75 g/kg vs 3 g/kg	15	9	81	**4.09×10^{-4}**
1.5 g/kg vs 3 g/kg	12	9	86	0.025

2.3.3 Comparison of acute vasculature changes in the mother and the fetus

Since there is a paucity of research on the acute changes in the developing fetal brain vasculature after maternal ethanol consumption, a method to validate if our surgical and experimental protocols were not biased was developed to simultaneously assess the effects of maternal alcohol consumption on both the mother and the fetus. Ethanol is known to have different effects on blood vessels based on the location of the vessel in the body, so vessels on the skin of the hind limb of the mother were imaged with the mother in a supine position. This location was chosen because the peripheral vessels on the forearm in humans are known to dilate when exposed to alcohol [190]. Since the forelimb of the mother was relatively difficult to image due to the surgical procedures on the abdominal cavity, the peripheral vessels on the hindlimb were imaged instead.

A dose of 3 g/kg of ethanol was tested on three mice. Instead of the usual procedure where the fetal brain was imaged for a period of 45 minutes after maternal ethanol consumption, imaging was performed after only 30 minutes to ensure proper imaging of the mother and fetal brain.

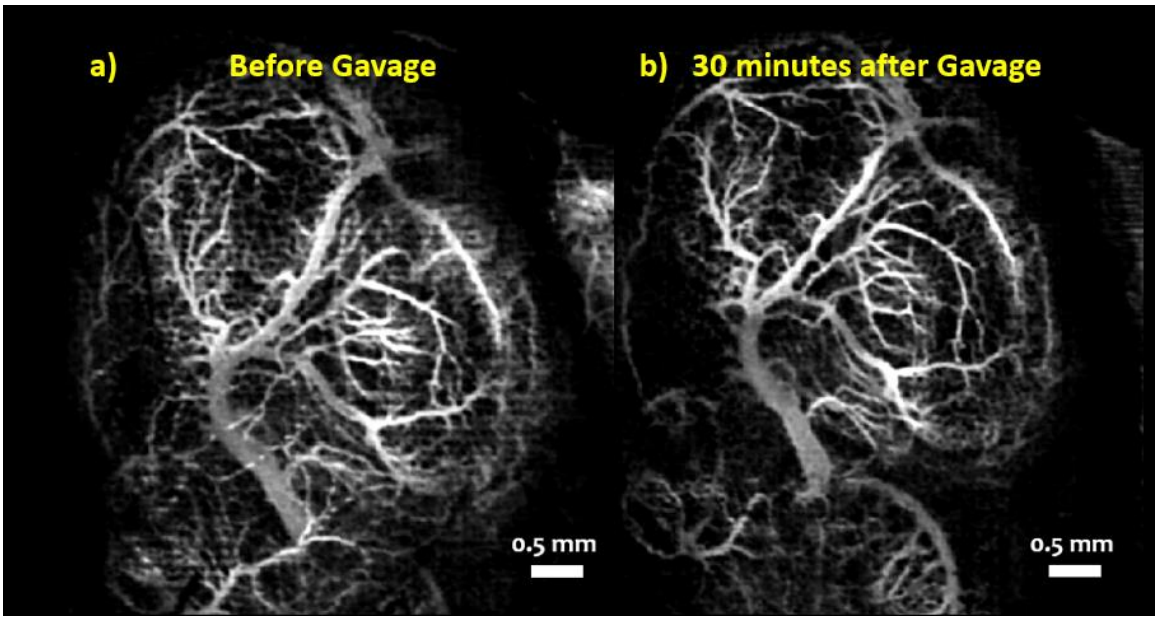

Figure 2.9 2D MIP of cm-OCA images of fetal brain vasculature (a) before and (b) 45 minutes after maternal exposure to ethanol at a dose of 3 g/kg.

Figures 2.9 (a) and (b) show MIPs of 3D cm-OCA images of the fetal brain before and 30 minutes after exposure to ethanol respectively. Similar to results shown in figures 2.3 (a) and (b) a drastic vasoconstriction was seen in the fetal brain within 30 minutes of ethanol exposure.

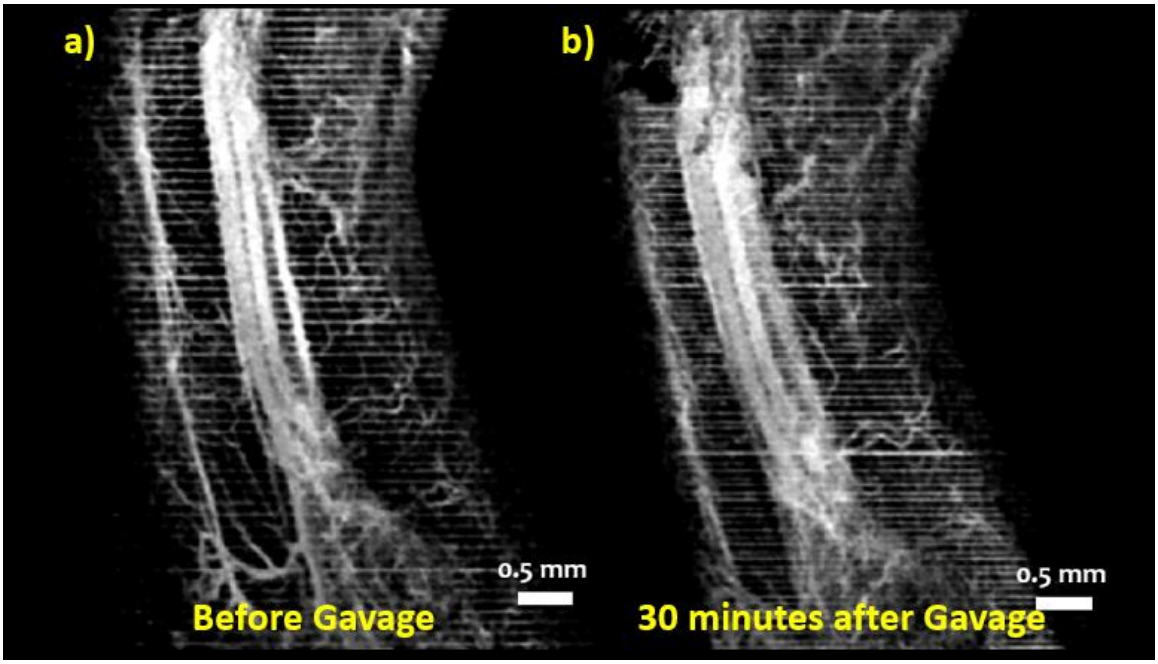

Figure 2.10 2D MIP of cm-OCA images of the hindlimb of the mother (a) before and (b) 45 minutes after maternal exposure to ethanol at a dose of 3 g/kg.

Figures 2.10 (a) and (b) show MIPs of 3D cm-OCA images of the mother's skin on her hindlimb before and 30 minutes after ethanol exposure respectively. A drastic vasodilation was noticed unlike the case of the fetal brain. This is similar to previous results shown on humans where vasodilation was noticed in forearm skin, whereas vasoconstriction was noticed in the underlying muscle [190].

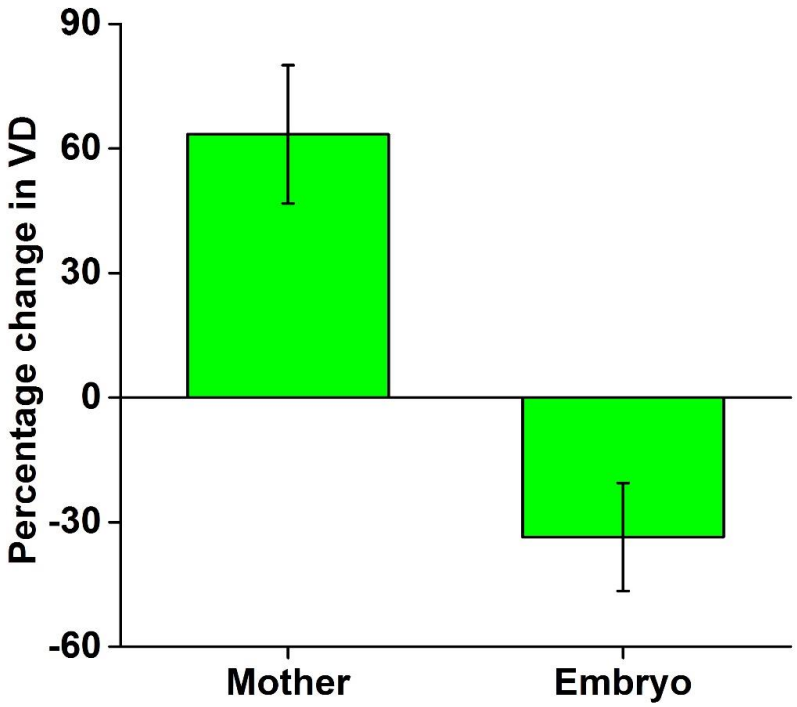

Figure 2.11 Comparison between percentage change in VD 45 minutes after maternal exposure to ethanol at a dose of 3g/kg in the mother and the embryo.

Figure 2.11 shows results from the VD quantifications that were performed both on the images from the mother and the fetus.

2.4 Discussion

The second trimester equivalent period of mouse gestation encompasses the peak period for fetal neurogenesis [170] and angiogenesis [21]. Brain development during this period is particularly vulnerable to alcohol. Hence, vasculature changes due to prenatal exposure to alcohol can have significant effects on brain development. In this chapter, *in utero* angiographic OCT was utilized to assess acute vasculature changes in the murine fetal brain caused by maternal alcohol consumption. The results showed a drastic reduction

in vessel diameter within 45 minutes of maternal alcohol exposure when compared to the sham group.

In a few samples from both the ethanol and sham groups, we noticed a disappearance of smaller tributaries emanating from the larger vessels. This gradual loss over time, was perhaps because of prolonged exposure to isoflurane anesthesia or due to partial occlusion of uterine vasculature during the process of exteriorization and immobilization of the uterine horn. Previous studies have shown that maternal heart rate was not significantly lowered by isoflurane, and that the ethanol itself did not alter maternal heart rate or blood flow, suggesting that the interaction between anesthesia and ethanol is minimum [183]. Moreover, the immobilization procedure was identical between all samples. Consequently, the reduction in fetal cranial vessel diameter was likely specifically due to acute maternal alcohol exposure.

One other factor that could probably influence the vessel diameter quantifications is the change in optical properties due to dehydration of the uterus that was depicted in figures 2.2 and 2.3. For this set of experiments (3 g/kg of ethanol), dehydration was observed in both the ethanol and sham groups, and all our measurements were made on fetal brain vasculature rather than uterine vasculature. Thus, we can safely assume that the influence of optical properties on our quantifications were negligible. After this set of experiments, the uterus was hydrated with 1X PBS, 1 minute before every measurement, reducing the complications of dehydration.

For the first set of experiments, ethanol was given at a volume of 3g/kg to the mother via intragastric gavage. As mentioned earlier, this dose was chosen as previous studies have shown that this dose resulted in a mean peak BAC of 117 mg/dL, representing

binge-like intoxication readily achieved in non-alcoholic human populations [183]. This level of BAC was achieved when 95% ethanol was used with C57BL/6 mice. In this work, we used approximately 17% ethanol, as CD-1 mice were used instead of C57BL/6 strain. C57BL/6 mice have higher tolerance towards alcohol [191]. Seeing such drastic effects at such low concentrations influenced the design of the next study, which involved studying the effects of different doses on the murine fetal brain vasculature. As expected, the dose response studies showed a decrease in the effects of ethanol on fetal brain vasculature as the dose decreased.

It is also important to determine if the changes in vasculature caused by ethanol exposure persist beyond the period of exposure or are reversed. In a previous study, effects of maternal exposure to ethanol on fetal cerebrovascular blood flow persisted for at least 24 hours [183], demonstrating that the effects of ethanol are persistent beyond the 45 minutes shown here. It will also be important in future studies to ascertain if changes in fetal and uterine blood flow are correlated.

Previous studies using ultrasound imaging have shown that maternal binge-alcohol exposure at earlier developmental time points (GD 12.5) resulted in an apparent decrease in cardiac stroke volume through fetal cranial arteries as measured by velocity time integral after a single binge-like exposure and also following subsequent repeated binge-like exposures [183]. Although our results have shown an immediate reduction in the fetal cranial vessel diameter following maternal ethanol exposure at GD 14.5, the relationship between vasoconstriction and reduction in cardiac stroke volume is yet to be determined. Other studies have shown that influence of gestational stage of exposure plays a crucial role in determining the effects if PAE on fetal development [192-194]. The mid-first

trimester through the second trimester equivalent period is a critical period for fetal neurogenesis [170], angiogenesis, and vasculogenesis [21]. Hence the vasoconstriction seen in this study could have permanent detrimental effects on brain development, which could lead to lifelong physical and mental disabilities. Previous studies have already shown distinct morphological changes in the murine fetal brain *ex vivo* after repeated binge-like exposures to alcohol using OCT [119]. Hence, future studies will also involve the impact of developmental stage and brain maturation on the cranial vascular effects of PAE.

2.4 Conclusions

This chapter demonstrated the use of *in utero* angiographic OCT to evaluate acute changes in developing fetal brain microvasculature due to maternal exposure to ethanol. Results showed a prominent decrease in vasculature within 45 minutes of exposure. Different doses of ethanol were tested, and the dose response curve was plotted. Finally, to validate our procedure, we simultaneously imaged blood vessels on the mother and the fetus and observed that while the vessels on the fetal brain constricted, the vessels on the skin of the hind limb of the mother dilated. Previous studies in humans have shown results similar to what was seen from the mother, thus opening doors for new studies to understand the reason for vasoconstriction in the fetal brain.

Chapter-3 Assessing nicotine induced fetal brain vasculature changes

In this chapter, acute changes in murine fetal brain vasculature caused due to prenatal exposure to nicotine were assessed using *in utero* cm-OCA. A home-built SS-OCT system was used to image the fetal brain and a post processing algorithm was used to create the vasculature maps. Results showed a significant decrease in vessel diameter minutes after maternal nicotine consumption, similar to the case of ethanol. Dose response studies were performed and two doses, including the main dose is included in this dissertation.

3.1 Introduction

Maternal cigarette smoking has been regarded as one of the main causes of congenital birth defects. In 2016, 7.2% women in the United States reported smoking during pregnancy [195]. Maternal smoking during pregnancy is known to cause several defects including intrauterine growth restriction (IUGR), placental abruption, still birth, preterm birth, low birth weight, sudden infant death syndrome, and spontaneous abortion [196-207]. Some defects are lifelong including learning disabilities, cognitive dysfunction, behavioral problems, attention deficit disorders, and psychiatric disorders [208-221]. Hence, smoking cessation is strongly recommended during pregnancy and lactation. Although this is always a recommendation, several women continue to smoke during their entire pregnancy, mostly due to nicotine addiction. Thus, even though 75% pregnant smokers have reported the desire to quit smoking, only 20 to 30% have been successful at it [222-224].

Since the inability to quit smoking is mostly attributed to nicotine withdrawal, nicotine replacement therapy (NRT) is the recommended pharmacotherapy for smoking cessation [225-228]. A substantial number of women also use electronic cigarettes or e-cigarettes to help quit smoking [229-231]. Both these approaches are usually sought after because of the belief that pure nicotine [232] provides a safe and effective way for smoking cessation as they do not have the other combustible and hazardous materials present in a traditional cigarette. This approach remains popular even after the US Food and Drug administration has classified nicotine as a category D drug [233].

E-cigarettes are electronic nicotine delivery devices that consist of a battery and a heating element consisting of the nicotine juice [234]. Depending upon the puff volume and the nicotine concentration, e-cigarettes deliver as high or higher amounts of nicotine as traditional cigarettes [235, 236]. Recent surveys have shown that 40% of pregnant women using e-cigarettes did not realize that e-cigarettes contained nicotine or could be addictive, and 40% believed that these are less harmful than conventional cigarettes [229]. NRT is widely available in the form nicotine gum, patches, lozenges, inhalators, and nasal sprays. These methods are known to deliver nicotine in amounts equivalent to smoking 10 cigarettes a day [237]. The safety of NRT in general, as well as during pregnancy, is not well documented.

During embryogenesis, the cellular and architectural assembly of the central nervous system is controlled by several neurotransmitters [238, 239]. These neurotransmitters perform multiple functions that aid in normal development including promoting neural cell replication, initiating differentiation from the replication, initiation and termination of axonogenesis and synaptogenesis, evoking or retarding apoptosis, and

enabling appropriate migration and localization of specific cell populations within the developing brain regions [240]. Due to the multitude of processes that occur during development, the brain is particularly vulnerable to neuroactive chemicals such as nicotine. Nicotine imitates the function of one such neurotransmitter, acetylcholine, by binding to acetylcholine receptors in the developing brain, thus hindering brain development. Prenatal nicotine exposure is known to affect brain development in several ways including triggering apoptosis, reducing the number neuronal cells, truncation of axonogenesis and deficient synaptogenesis [241-250]. Most importantly, nicotine is shown to cause delayed-onset changes [248, 251], that is, even when nicotine is no longer present in the system, its effects are still seen by causing damage to the brain in the postnatal period, thus changing the trajectory of brain development.

As mentioned earlier in this dissertation, the gestational stage at which maternal exposure to teratogens occurs is a very important factor in determining the severity and the type of defect caused. Initially, it was thought that during the first trimester, nicotinic acetylcholine receptors (nAChRs) were not expressed in sufficient numbers. Hence several studies concluded that exposure to nicotine during the first trimester, would not cause a significant effect on the fetus [245, 248, 252]. However, recent studies have shown that not only are nAChRs present, but they are biologically active even during the development of the neural tube, during the first trimester [253, 254]. This emphasizes the need to study the effects of nicotine and other teratogens on neural tube closure. Appendix A3 of this dissertation focuses on imaging neural tube closure and will provide more details on how OCT has been used in combination with Brillouin microscopy to evaluate changes in biomechanical properties of the neural tube tissue at different developmental stages. It has

also been shown that excessive stimulation of nAChRs by nicotine causes profound disruption at the cellular and architectural levels [255]. The second trimester, on the other hand, is a critical period for brain development as several neurons are born during this period [170]. Apart from this, the microvasculature that invade the fetal brain during this period is known to aid in several aspects of fetal development, including supporting nutritional needs of the embryo, providing endocrinal support, and neural development [21, 181, 182]. Even though there has been a wide variety of research focused on outcomes from prenatal nicotine exposure, there has been no research done on evaluating the effects of acute exposure to nicotine, during the second trimester, on the developing fetal brain vasculature.

This chapter summarizes the use of *in utero* cm-OCA to evaluate fetal brain vasculature changes due to maternal exposure to pure nicotine during the second trimester. A dose response analysis was also performed, including a dose that corresponds to an average human dose. Results showed a decrease in vasculature in both doses of nicotine, that was not observed in the sham group.

3.2 Materials and methods

3.2.1 OCT system

Please refer to appendix A1.

3.2.2 Animal manipulations

Please refer to appendix A2.

3.2.3 Dosing

Two doses of nicotine were tested. For the preliminary study, a dose of 1 mg/kg of nicotine was used, which is a relatively high dose in comparison to the levels of nicotine achieved by an average human who smokes. However, mice are known to metabolize nicotine faster [240] and hence this dose could be considered a moderate dose for a mouse model. Hence, this was the first dose that was tested. An average smoker receives approximately 8 to 20 mg of nicotine per 80 to 100 kg of body weight. Hence, 0.1 mg/kg was the next dose that was tested to simulate human smoking. The sham group was given the equivalent volume of distilled water.

3.2.4 Imaging, quantification, and statistics

The imaging procedure is similar to that presented in the cm-OCA portion of chapter 2. The 3D OCT image consisted of 600 B-scans per volume and each B-scan consisted of 600 A-scans. Five B-scans were recorded at each spatial position. The time for each B-scan was 20 ms and the total acquisition time was 84 seconds including the galvanometer flyback time between B-scans. An approximate total area of 6.0 x 6.2 mm^2 of the fetal brain was imaged. The vasculature maps were obtained using a post-processing cm-OCA algorithm. A discrete Fourier transform-based sub-pixel registration technique was used to correct the axial shift caused due to bulk motion between each pair of 5 B-scans that were recorded at the same spatial position. The average temporal correlation between these 5 B-scans, in pairs, was calculated to obtain the correlation coefficient. The SNR-dependent artifacts were corrected by using the temporal variance of the background noise as a function of imaging depth. Angiograms with a global correlation value below a threshold of the difference between the mean and the SD were disregarded. The 3D

vasculature maps were obtained from the spatial distribution of the temporal correlation coefficients of the entire 3D image. A MIP was calculated to obtain the *en face* images of the dorsal surface arterial blood vessels on the fetal brain. A frequency rejection filter was applied to the 2D MIPs to remove bulk motion artifacts due to maternal respiration and heartbeat. Amira software (EFI Co., Portland, Oregon) was used for denoising and to form final MIPs.

For these studies, three different parameters, vessel area density (VAD), vessel length fraction (VLF), and vessel diameter (VD) were used to quantify the vasculature. VAD is defined as the area of the image that corresponds to the vasculature, A_{vessel}, divided by the total area of the image, A_{image}, ($VAD= A_{vessel}/A_{image}$), and VLF is defined as the total length of the vessels L_{vessel}, divided by the total area of the image ($VLF= L_{vessel}/A_{image}$). Image J was used to calculate the VAD (from the binarized MIP) and VLF (from the skeletonized binary MIP), while Amira was used to calculate the VD. Only a portion of the MIP including the main vessel was used for quantifications.

First, a nonparametric Kruskal-Wallis ANOVA was performed to assess the effects of different doses on the vasculature. This was followed by a 2-sided Mann-Whitney *U* test that was performed to test for statistically significant changes between every nicotine group and the sham group, and the 2 nicotine groups. Bonferroni correction was performed to correct for multiple testing for the pair-wise tests.

3.3 Results

Like the results shown in the previous chapter, vasculature maps from one fetus from each of the groups are first shown followed by the quantifications and statistics. The

total number of fetuses in the sham group were 6, the nicotine group at a dose of 0.1 mg/kg was 6, and the nicotine group at a dose of 1 mg/kg was 5.

Figure 3.1 shows results from one fetus from the sham group. Figures 3.1 (a) and (b) are MIPs of 3D cm-OCA images before and 45 minutes after maternal exposure to distilled water respectively. Results from the sham group showed almost no change in vasculature 45 minutes after exposure to distilled water.

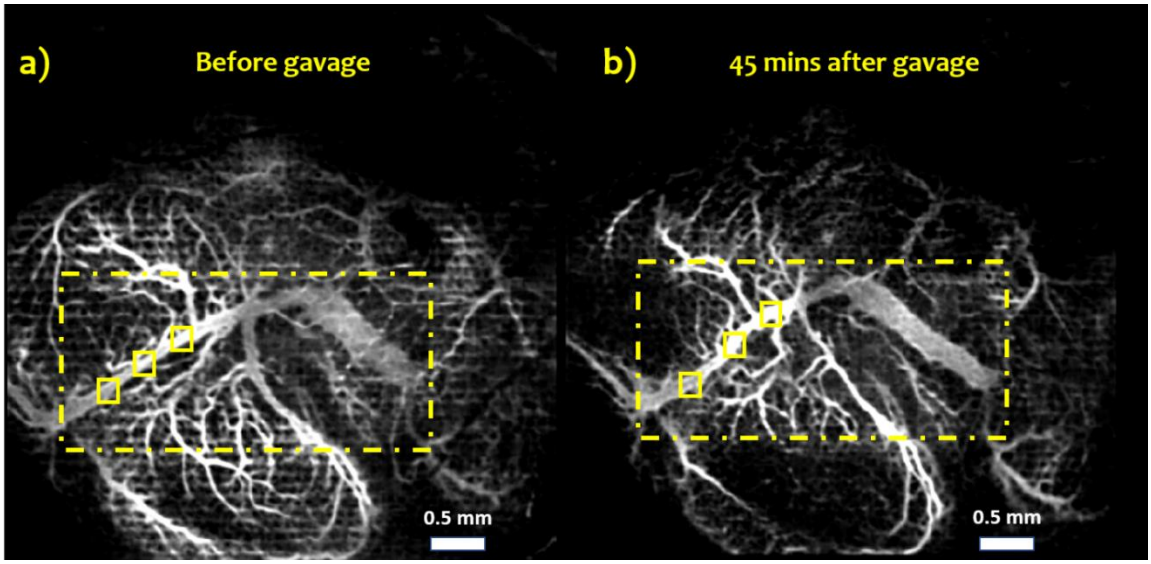

Figure 3.1 2D MIP of cm-OCA images of the fetal brain vasculature (a) before and (b) 45 minutes after maternal exposure to distilled water.

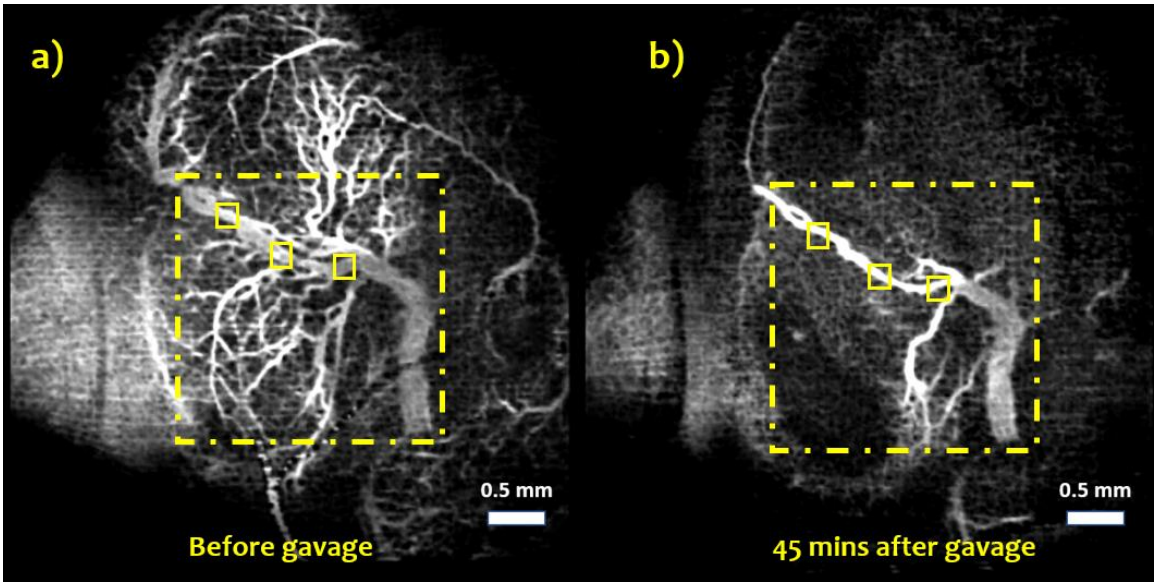

Figure 3.2 2D MIP of cm-OCA images of fetal brain vasculature (a) before and (b) 45 minutes after maternal exposure to nicotine at a dose of 1 mg/kg.

Figure 3.2 (a) and (b) show MIPs of 3D cm-OCA images before and after maternal exposure to nicotine at a dose of 1 mg/kg. Unlike the sham group, within 45 minutes after exposure to nicotine at a dose of 1 mg/kg, there was a dramatic decrease in vasculature. Not only was vasoconstriction observed in the main vessel under investigation, but there was also a disappearance of the surrounding smaller tributaries.

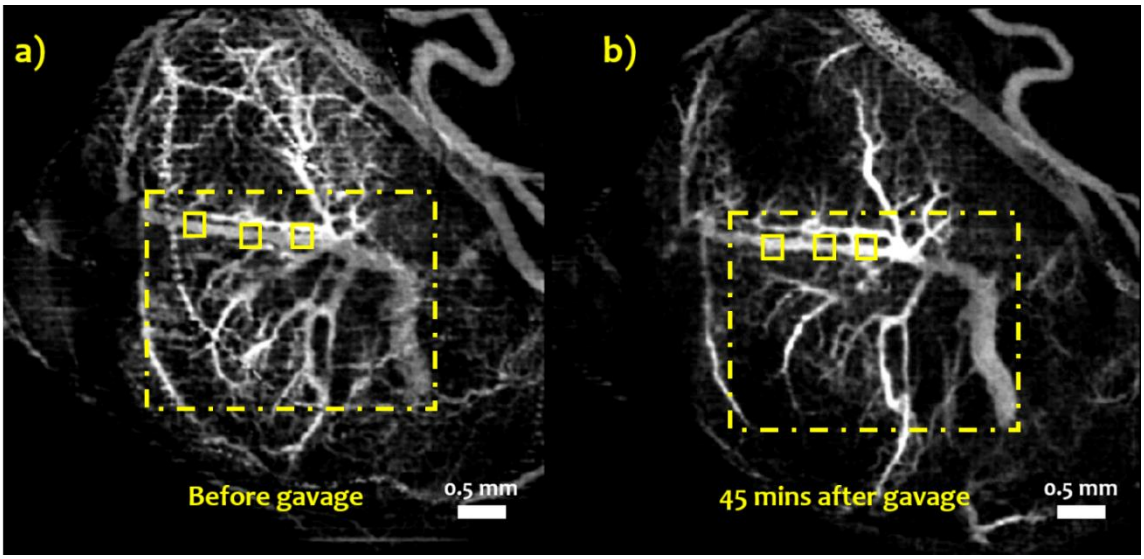

Figure 3.3 2D MIP of cm-OCA images of fetal brain vasculature (a) before and (b) 45 minutes after maternal exposure to nicotine at a dose of 0.1 mg/kg.

Figure 3.3 (a) and (b) show MIPs of 3D cm-OCA images before and 45 minutes after maternal exposure to nicotine at a dose of 0.1 mg/kg. A reduction in vasculature was observed unlike the sham group. However, there was no disappearance in the smaller tributaries as seen in the case of the fetuses exposed to nicotine at a dose of 1 mg/ kg.

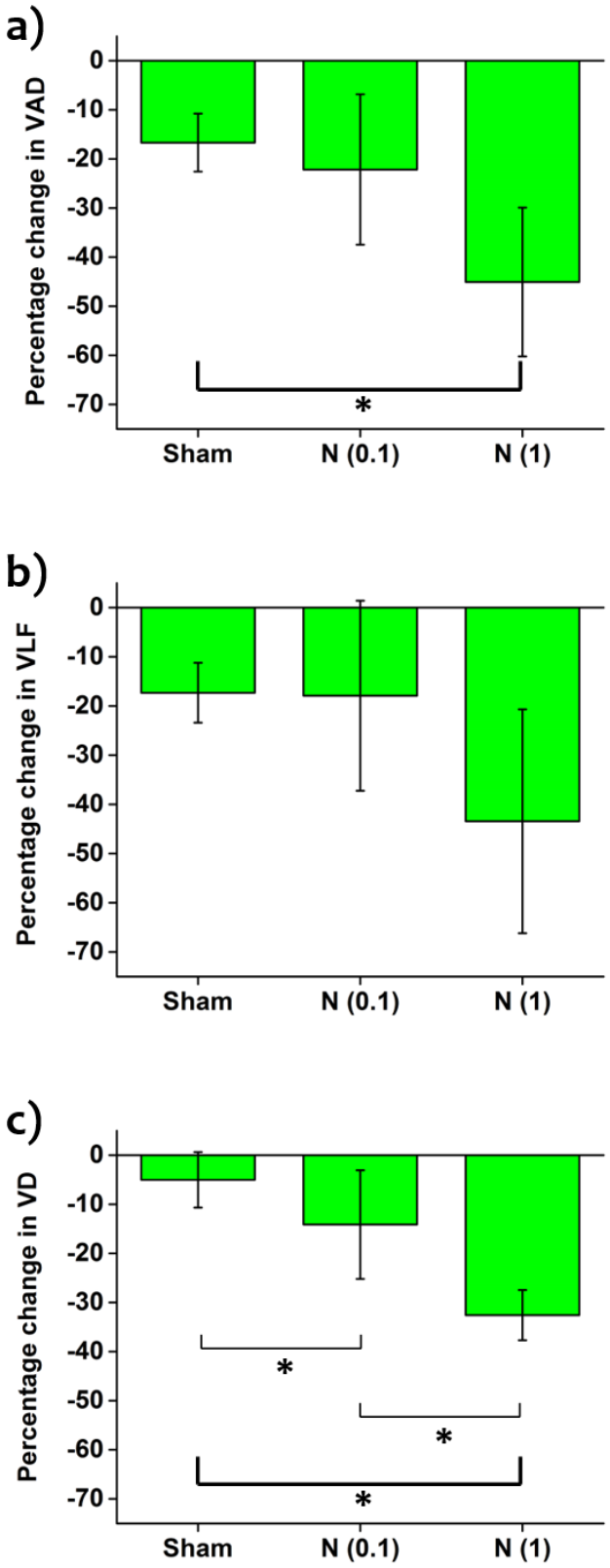

Figure 3.4 Comparisons of percentage change in (a) VAD, (b) VLF, and (c) VD at 45 minutes after maternal exposure to distilled water, and nicotine at doses 0.1 mg/kg and 1 mg/kg.

Figure 3.4 shows a comparison of percentage changes in the quantification parameters at 45 minutes after exposure, between all three groups. Figure 3.4 (a), (b), and (c) depict the changes in VAD, VLF, and VD respectively.

The Kruskal-Wallis ANOVA showed a statistically significant difference between the three groups in the case of VAD and VD, which was not seen in the case of VLF.

The 2-sided Mann-Whitney U test was performed between each of the groups (3 pairs in total) for each VAD, VLF, and VD for pairwise testing. For VLF, there was no statistically significant difference between any of the three pairs. For VAD, while there was a statistically significant difference between the sham and nicotine at a dose of 1 mg/kg, no significant change was seen between the sham group and the nicotine group at a dose of 0.1 mg/kg as well as both the nicotine groups. Percentage change in VD showed statistically significant differences between all three pairs. Table 3.1 shows a summary of results from the Mann-Whitney U test.

Table 3.1 Summary of the Mann-Whitney *U* tests. P values in bold indicates statistical significance.

		VAD	**VLF**	**VD**
	N_{sham}	6	6	18
	$N_{nicotine\ (0.1\ mg/kg)}$	6	6	18
	$N_{nicotine\ (1\ mg/kg)}$	5	5	15
Sham Vs Nicotine (0.1 mg/kg)	U	24	19	266
	P	0.378	0.936	**0.001**
Sham Vs Nicotine (1 mg/kg)	U	30	26	269
	P	**0.008**	0.055	< **0.001**
Nicotine (0.1 mg/kg) Vs Nicotine (1 mg/kg)	U	26	24	266
	P	0.055	0.121	< **0.001**

3.4 Discussion

Vasculature that develops in the brain during the second trimester is vulnerable to teratogens as this period is crucial for fetal angiogenesis. Thus, it is important to study the changes in vasculature that occur due to maternal exposure to various teratogens during the second trimester. This chapter evaluates the acute changes in fetal brain vasculature caused due to maternal exposure to nicotine at a gestational stage corresponding to the second

trimester, using cm-OCA. The vasoconstrictive response to nicotine and the imaging plane are both consistent with the distribution of the terminal anterior and middle cerebral arterial tributaries on the dorsolateral pial surface of the fetal brain.

All VAD and VLF quantifications were performed over the area depicted by the dashed rectangle in figures 3.1, 3.2, and 3.3 to prevent the influence of external noise caused by maternal heartbeat and respiration as well as changes in vasculature in the uterus. However, since the clamping procedure that was performed to stabilize the fetus and reduce bulk motion was utilized uniformly across all samples from all groups, any influence due to clamping, would have affected every sample. Thus, sham groups were utilized as direct comparisons.

Although there was a drastic reduction in vasculature when exposed to the higher dose of nicotine as seen from figure 3.2, there seemed to be no drastic change in the overall length of the major vessel under investigation. This could possibly be the reason why the VLF calculations did not show any statistically significant differences between any of the three groups.

For this study, the effects of only two doses of nicotine were evaluated. The dose of 1mg/kg was chosen as the higher dose as it causes IUGR. Since drastic effects were seen within a period of 45 minutes after exposure to nicotine, a lower dose of 0.1 mg/kg (which is equivalent to what an average smoker receives from one cigarette) was used. However, rodent models are known to metabolize nicotine much faster [240]. Thus, these drastic effects seen with a dose of 1mg/kg is the consequence of administering a moderate dose, for a mouse. Several studies that use rodent models have used relatively higher doses of 6 mg/kg per day [256, 257]. A dose of 6 mg/kg is equivalent to a human smoking around 2

packs of cigarette per day [258]. Studies have also shown that at higher doses, nicotine desensitizes the nAChRs, which renders them unresponsive to nicotine [259]. These points emphasize the need to test higher doses of nicotine to evaluate whether fetal brain vasculature also becomes saturated at high doses.

Another important factor involved in studying the effects of prenatal exposure to nicotine in animals is the route of administration. Typically, smokers have random highs and lows of nicotine concentration in their plasma during the day followed by a long period of no exposure during the night [259]. This work used intragastric gavage to administer nicotine because of which the mother is exposed to the entire dose of nicotine within a few seconds. This causes a sudden increase in plasma nicotine concentration, that occurs in a few seconds unlike in the case of smokers, where it happens in a few minutes. Another example of route of administration is subcutaneous injections which also results in a similar spike in nicotine concentration comparable to intragastric gavage [260]. Two other methods used to administer nicotine include subcutaneously implanted osmotic pumps and nicotine administration through drinking water. The osmotic pumps release a constant amount of nicotine into the animal, resulting in a persistent exposure to the drug without the drastic variations [261]. Although this is not what is seen in smokers, these pumps provide a good model to simulate nicotine patches and for studying mechanisms. Nicotine administration through drinking water offers less control over timing and dosing of nicotine across animals. However, this method creates realistic dynamics in a 24-hour period, without creating artificial spikes [259]. Hence it is important to choose the right method of administration depending upon the application and subject of study. Since this study was focused on imaging the acute effects of nicotine, intragastric gavage was selected as the

method for delivering a controlled bolus of nicotine and for generating as easily comparable sham control group.

Finally, work in this chapter focused on the acute effects of maternal nicotine consumption on fetal cerebral blood flow. However, nicotine use often co-occurs with other risk factors for impaired fetal development like maternal stress [260, 262-264], cardiovascular [265, 266] and metabolic disease [267]. Moreover, nicotine is often co-abused with other drugs including alcohol [268, 269]. These co-occurring conditions may amplify the effects of maternal nicotine on fetal cerebral blood flow, and their contributary effects need further investigation.

3.5 Conclusions

This chapter demonstrated the use of *in utero* cm-OCA to evaluate acute changes in the developing murine brain vasculature due to maternal exposure to nicotine. Results showed a drastic decrease in vasculature within 45 minutes of maternal exposure. A total of two doses of nicotine were tested. As expected, results showed a decrease in the severity of the effect for the lower dose when compared to the higher dose.

Chapter-4 Assessing synthetic cannabinoid induced fetal brain vasculature changes

In this chapter, acute changes in murine fetal brain vasculature caused by prenatal exposure to a synthetic cannabinoid (SCB) were assessed using *in utero* cm-OCA. A home-built SS-OCT system was used to image the fetal brain, and a post processing algorithm was used to create the vasculature maps. Results showed a significant decrease in vessel diameter minutes after maternal SCB exposure, suggesting a possible decrease in blood flow to the developing brain during the peak period of fetal neurogenesis and angiogenesis.

4.1 Introduction

Prenatal substance abuse is a major public health concern [143]. Marijuana is one of the most commonly abused substance during pregnancy [144, 270]. Due to its legalization in several states, it has rapidly become a targeted topic of research. Synthetic cannabinoids (SCBs) are a group of heterogeneous compounds that are similar to natural cannabinoids and were developed to understand the endogenous cannabinoid system and to understand their potential use as therapeutics [271, 272]. However, several variations of SCBs are commercially produced under various brand names and are being marketed as safe and legal alternatives to marijuana. SCBs are known to provide similar psychoactive effects to Δ^9-tetrahydrocannabinol (Δ^9-THC), the major psychoactive component of marijuana, and are easily accessible over the internet and in specialty shops in ready-to-use formulations. Most importantly, they are undetectable in routine drug screens [273, 274]. All this has increased the popularity of SCB usage.

SCBs and Δ^9-THC target the same receptors in the body. However, they have some important differences that increase the potency of SCBs [274]. While Δ^9-THC is only a partial agonist, SCBs are direct agonists [275-277], and SCBs have higher binding affinities to the cannabinoid receptors than Δ^9-THC [271]. In addition, variations in chemical structure [278] and concentration [279] in different SCB products, or sometimes even within the same product have made SCBs 40- to 600- fold more potent than Δ^9-THC. Thus, SCBs are more toxic in nature and produce more harmful effects as compared to Δ^9-THC.

With recent studies showing an increase in both natural cannabinoid and SCB use among women of reproductive age [280-284], and the prevalence of unplanned pregnancies in the United States [167], there is an increase in likelihood of prenatal exposure to cannabinoids. Apart from this, Δ^9-THC is lipophilic in nature [285, 286] and hence is known to cross the feto-placental barrier. Δ^9-THC is also secreted through breast milk [287, 288] which increases the chance of exposure to these drugs even after birth. This emphasizes the need to study both the prenatal and neonatal effects of cannabinoids on fetal developmental processes.

Since the endogenous cannabinoid system starts developing very early in vertebrates [289-291], most of the efforts to study the effects of prenatal exposure to SCBs have been focused on first trimester exposure [292]. The studies focusing on the effects of prenatal exposure to cannabinoids during the first trimester have shown extremely detrimental effects on the fetus including an increased incidence of fetal reabsorption, edema, spina bifida, exencephaly, omphalocele, phocomelia, and myelocele [293, 294].

However, there is significantly much less documentation on the effects of second trimester exposure to cannabinoids.

Apart from the second trimester being the peak period for fetal neurogenesis and angiogenesis [170], endocannabinoid signaling is known to play a major role in brain development [295]. The microvasculature that develops during this period is also known to perform several functions to support a developing fetus [21, 181, 182]. Thus, there is a need to study the effects of second trimester exposure to SCBs on fetal brain development and microvasculature development.

In this chapter, *in utero* cm-OCA was utilized to evaluate changes in fetal brain vasculature due to maternal exposure to a SCB. Results were compared to measurements taken before maternal exposure to the drug as well as to a sham group. Results showed drastic reduction vasculature within 45 minutes after maternal exposure to the SCB unlike the case of the sham group.

4.2 Materials and methods

4.2.1 OCT system

Please refer to appendix A1.

4.2.2 Animal manipulations

Please refer to appendix A2.

4.2.3 Dosing

For this study, CP-55,940, a well characterized compound in SCB research was used and was formulated for maternal exposure based on a protocol similar to Gilbert et al. [296]. CP-55,940 at a dose of 2 mg/kg was suspended in a vehicle of dimethyl sulfoxide (DMSO): Alkamuls El620 (Rhodia, NJ): lactated Ringer's solution at a ratio of 1:1:18 and sprayed on to the mother's liver to simulate intraperitoneal exposure. For the sham group, an equivalent volume of only the vehicle solution alone (without the SCB) was delivered into the peritoneal cavity in an identical manner.

4.2.4 Imaging, quantifications, and statistics

The imaging procedure was identical to the one used in chapter 3. 3D OCT images consisted of 600 B-scans per volume and each B-scan consisted of 600 A-scans. Five B-scans were recorded at each spatial position. The time for each B-scan was 20 ms and the total acquisition time was 84 seconds including the galvanometer flyback time between B-scans. An approximate total area of 6.0 x 6.2 mm^2 of the fetal brain was imaged. The vasculature maps were obtained using a post-processing cm-OCA algorithm. A discrete Fourier transform-based sub-pixel registration technique was used to correct the axial shift caused due to bulk motion between each pair of 5 B-scans that were recorded at the same spatial position. The average temporal correlation between these 5 B-scans, in pairs, was calculated to obtain the correlation coefficient. The SNR-dependent artifacts were corrected by using the temporal variance of the background noise as a function of imaging depth. Angiograms with a global correlation value below a threshold of the difference between the mean and the SD were disregarded. The 3D vasculature maps were obtained from the spatial distribution of the temporal correlation coefficients of the entire 3D image.

A MIP was calculated to obtain the *en face* images of the fetal brain vasculature. A frequency rejection filter was applied to the 2D MIPs to remove bulk motion artifacts due to maternal respiration and heartbeat. Amira software (EFI Co., Portland, Oregon) was used to form final 2D MIPs.

A hessian filter-based approach was used to enhance the contrast and connectivity of the blood vessels in the 2D MIP (Hessian based Frangi Vesselness filter, Dirk-Jan Kroon, MathWorks File Exchange, Mathworks, Natick, Massachusetts). Image J was used to calculate the VAD (from the binarized MIP) and VLF (from the skeletonized binary MIP), while Matlab was used to calculate the VD. Only a portion of the MIP including the main vessel was used for quantifications.

A nonparametric Kruskal-Wallis ANOVA was performed on the VD data of each sample to assess if there was a statistically significant change over time. A 2-sided Mann-Whitney *U* test was performed to test for statistically significant changes between the cannabinoid and the sham groups at 45 minutes post exposure.

4.3 Results

The total number of samples was 3 in the cannabinoid group and 5 in the sham group. Results from one fetus from each of the groups are shown below. Figures 4.1 (A) and (B) depict 2D MIPs of 3D cm-OCA images of murine fetal brain vasculature before and 45 minutes after exposure to the SCB respectively.

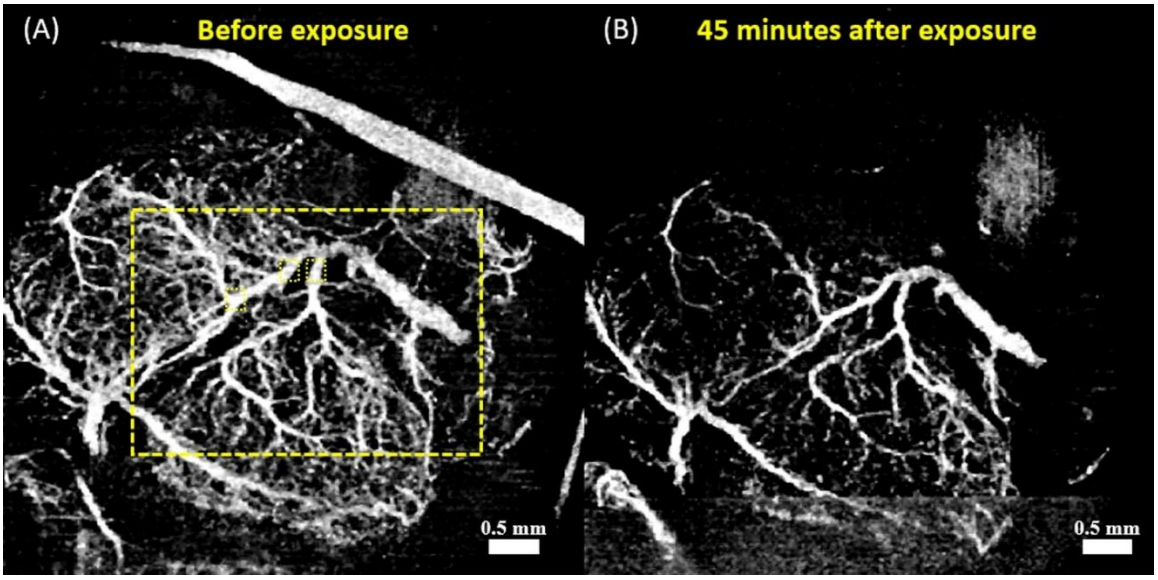

Figure 4.1 2D MIPs of cm-OCA images of fetal brain vasculature (a) before and (b) 45 minutes after maternal exposure to the SCB. The dashed rectangle depicts the region of VAD and VLF quantifications. The small dashed squares depict the regions used for VD quantifications.

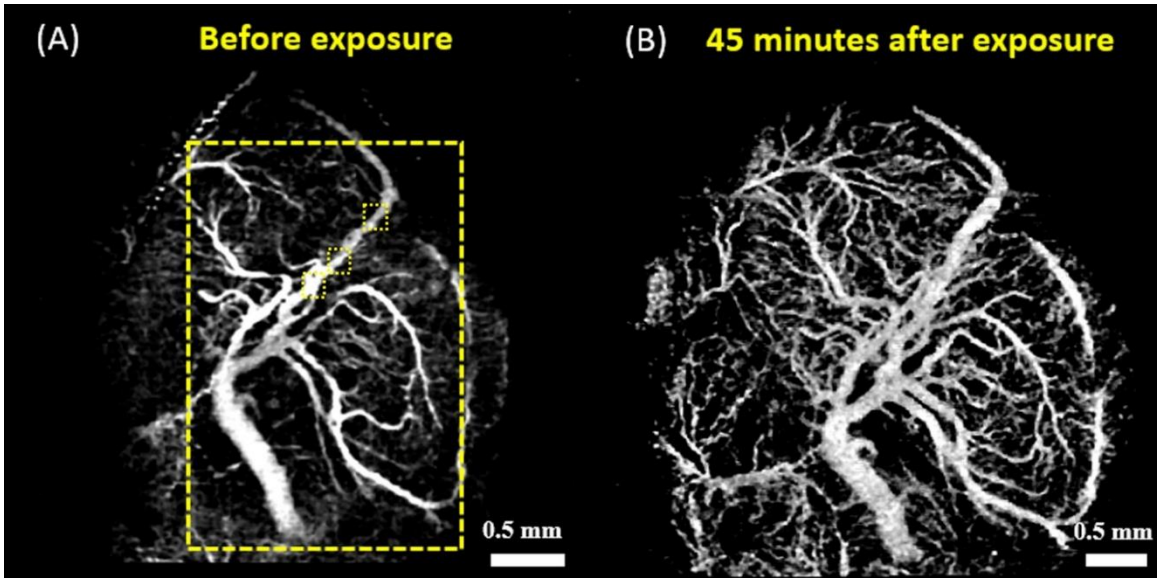

Figure 4.2 2D MIPs of cm-OCA images of fetal brain vasculature (a) before and (b) 45 minutes after maternal exposure to the vehicle solution (without SCB). The dashed rectangle depicts the region of VAD and VLF quantifications. The small dashed squares depict the regions used for VD quantifications.

Figures 4.2 (A) and (B) depict 2D MIPs of 3D cm-OCA images of murine fetal brain vasculature before and 45 minutes after exposure to the vehicle (without the SCB) respectively.

Figure 4.1 shows a drastic reduction in vasculature within 45 minutes of maternal SCB exposure whereas a slight increase is seen within 45 minutes after maternal exposure to the vehicle solution alone. VAD and VLF quantifications were made within the area depicted by the dotted yellow rectangles in figures 4.1 (A) and 4.2 (A), which includes the main vessel under investigation. VD quantifications were made in the 3 locations depicted by dotted yellow squares on the main vessel. This was done to ensure consistency.

Figure 4.3 (A), (B), and (C) show VAD, VLF, and VD quantifications, respectively, for each of the samples from the cannabinoid and the sham groups shown in figures 4.1 and 4.2. The plots show percentage change in each of the parameters for a 45-minute period at intervals of 5 minutes as compared to the initial measurement before maternal exposure to the cannabinoid or the vehicle. For the sample from the cannabinoid group, all the parameters decrease, whereas for the sham group, all three parameters showed a slight increase. The VAD, VLF, and VD decrease by approximately 40%, 56%, and 33% respectively in the cannabinoids group, while it increased by approximately 35%, 26%, and 17% respectively in the sham group.

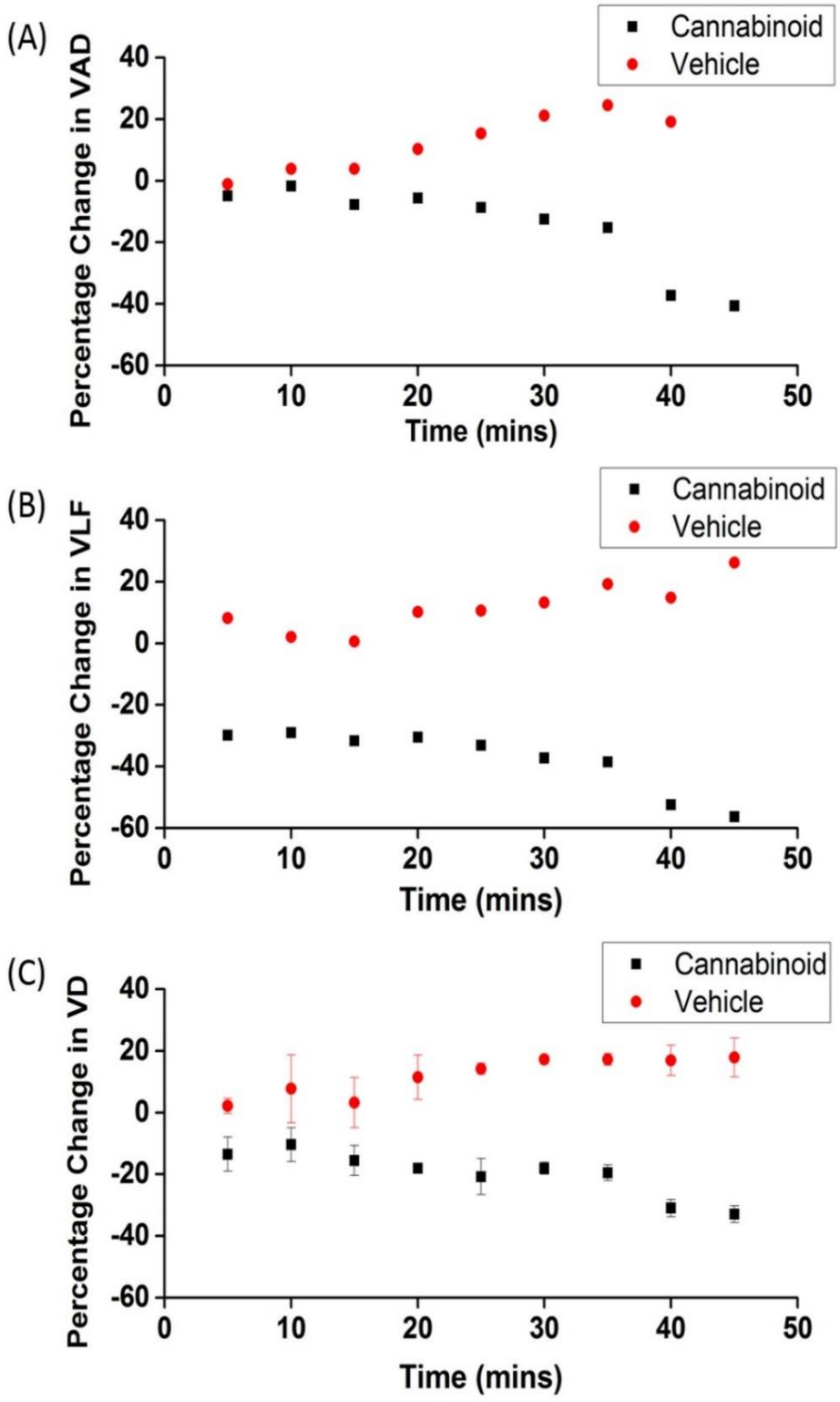

Figure 4.3 Quantifications of one sample each from the sham and cannabinoid group. Percentage change in (A) VAD, (B) VLF, and (VD) after exposure, every 5 minutes for 45 minutes. The error bars represent the standard deviation.

A Kruskal-Wallis ANOVA was performed on the VD data of all samples, since three positions in the vessel were measured at every time point. All the samples in the cannabinoid group showed a statistically significant decrease ($P < 0.001$) in diameter over time, while all samples in the sham group showed a statistically significant increase ($P = 0.028$) in vessel diameter over time.

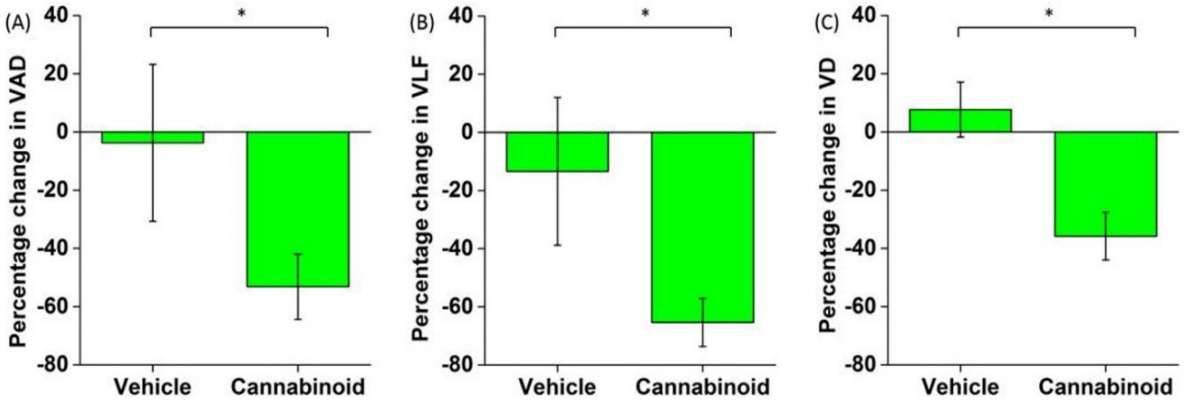

Figure 4.4 Percentage change in (A) VAD, (B) VLF, and (C) VD 45 minutes after maternal exposure. The asterisk indicates statistical significance ($P < 0.05$ by a 2-sided Mann-Whitney *U* test).

Figure 4.4 (A), (B), and (C) show a summary of the VAD, VLF, and VD quantifications respectively from all the samples from both groups. The data is shown as the mean percentage change in each of the parameters at 45 minutes post maternal exposure as compared to the initial measurements before exposure to the cannabinoid or the vehicle. A Mann- Whitney *U* test showed statistically significant differences between the cannabinoid and the sham groups at 45 minutes post exposure for all three parameters. Table 4 summarizes results from the Mann-Whitney U test for each of the parameters used to quantify vasculature.

Table 4.1 Summary of the Mann-Whitney *U* tests. P values in bold indicates statistical significance.

	VAD	**VLF**	**VD**
N $_{vehicle}$	5	5	15
N $_{cannabinoid}$	3	3	9
U	15	15	135
P	**0.0369**	**0.0369**	**<0.001**

4.4 Discussion

Cannabinoids are one of the most widely used psychoactive drugs in the world. About 3.8% of the population of the world between the ages of 15 and 64 have reported cannabis use [297]. Although cannabis is considered a harmless recreational agent [298], and sometimes even therapeutic, literature shows that it can have drastic effects on the adult [299] and developing brain [300].

About 2.5% of women have reported cannabis use during pregnancy and sometimes even during lactation [301]. Studies have not only shown that some cannabis metabolites are found in different types of fetal tissues [302] including the placenta, amniotic fluid, and the fetus itself [303], but due to its lipophilic nature [304], cannabinoids cross barriers including the feto-placental barrier, and the blood-brain barrier. Human brain development starts *in utero* and continues until about 25 years of age, so both prenatal and postnatal exposure poses serious threats to the developing brain. Several studies have shown metabolic, behavioral, and cognitive effects caused by prenatal cannabis exposure. However, vasculature changes caused have not been well-documented.

In this chapter, *in utero* cm-OCA was used to evaluate changes in murine fetal brain vasculature cause by prenatal exposure to CP-55,940, a SCB. Results showed a drastic decrease in vasculature when compared to the sham group, within 45 minutes of maternal exposure.

All the quantifications were made over a certain area depicted by the dotted yellow rectangles in figures 4.1 and 4.2. This was done to reduce the influence of blood vessels other than the major vessel under investigation. For example, during fetal manipulations, there is a lack of complete control over the uterus and yolk sac. Hence vessels from the uterus and yolk sac might be present in images from some of the time points but not necessarily in every image or due to the clamping procedure that is used to reduce bulk motion, uterine vessels that may appear in the first data set collected may eventually disappear during the experiment, which can be seen clearly in figure 4.1 (A) but disappears in 4.1(B). The influence of these factors was removed by selecting constant and repeatable areas for quantifications.

CP-55,940 was the SCB of choice as it is a well-known and well-characterized compound in SCB research. It was administered at a dose of 2 mg/kg following a similar protocol to Gilbert et al. [296]. However, instead of dissolving the SCB in ethanol, it was dissolved it in DMSO as the results shown in chapter 2 demonstrate drastic vasoconstriction caused by prenatal exposure to ethanol [305]. DMSO has histamine releasing properties, which causes vasodilation [306, 307]. This could possibly explain the increase in vasculature observed in figure 4.2 (the sham group) that was not seen in the presence of the SCB. This also explains the results of the Kruskal-Wallis ANOVA. Both the sham and cannabinoid groups showed statistically significant change in VD over time.

However, the sham group had a positive slope, and the cannabinoid group had a negative slope, showing the increase and decrease in VD, respectively.

The work in chapter 2 evaluating the effects of prenatal exposure to ethanol on fetal brain vasculature showed similar results to this study [305]. Although fetal alcohol syndrome-like features have been reported due to prenatal cannabis exposure in human cannabinoid developmental toxicology studies [308], several animal studies have not corroborated these results. Since this area of research is still in its early stages, more detail-oriented studies are necessary. Meticulous dose-response studies, research covering different gestational periods of exposure, and multiple exposure experiments are needed to better understand the effects of cannabinoid exposure on the developing brain in addition to cognitive studies that correlate structural changes with functional outcomes. Correspondingly, future work will be focused on these studies.

4.5 Conclusions

This chapter demonstrated the use of *in utero* cm-OCA to evaluate the acute changes in developing fetal brain vasculature due to prenatal exposure to a SCB, CP-55,940. Results showed a drastic decrease in vessel area density (approximately 53%), vessel length fraction (approximately 65%), and vessel diameter (approximately 35%) within 45 minutes of maternal exposure, suggesting the possibility of the SCB, CP-55,940, acting as a vasoconstrictor on the developing brain. With not much documentation on the effects of vasculature changes caused due to prenatal exposure to teratogens, this work, for the first time, evaluates these changes caused due to this SCB.

Chapter-5 Conclusions and future directions

This dissertation has presented the use of functional extensions of OCT to evaluate changes in murine fetal brain vasculature caused by exposure to different teratogens. Three major sections of this dissertation are based on second trimester-equivalent exposure to different teratogens. A summary of the three sections are specified below:

1) *In utero* angiographic OCT was used to image acute fetal brain vasculature changes caused by prenatal ethanol exposure. The first study in this chapter was a single dose study that simulated binge-drinking in humans. This was followed by dose response studies, where a total of three doses, including the dose in the first study were tested. The chapter concluded with a comparison between changes in vasculature in the mother and the fetus, after maternal exposure to ethanol. Results showed vasoconstriction in the vessels in the fetal brain when the mother was exposed to ethanol, which was not seen in the sham group. The vasoconstriction was relatively less in the lower doses compared to the highest dose tested. Moreover, peripheral vessel dilation was seen in the mother whereas vasoconstriction was observed in the fetal brain.
2) *In utero* angiographic OCT was used to image acute fetal brain vasculature changes caused by prenatal nicotine exposure. Two doses of nicotine were tested. The first dose simulated human smoking, whereas the second was a higher dose, because mice metabolize nicotine faster than humans. Maternal exposure to both these doses resulted in significant vasoconstriction in the fetal brain vessels compared to the sham group. However, the severity of vasoconstriction was significantly less for

the lower dose, similar to dose-dependent vasoconstriction seen with ethanol exposure.

3) *In utero* angiographic OCT was used to image fetal brain vasculature changes caused by prenatal SCB exposure. CP-55,940, a well-known compound in SCB research, was used at a dose of 2 mg/kg. Maternal exposure to the SCB caused significant vasoconstriction in the fetal brain vessels that was not seen in the sham group. In fact, the sham group showed vasodilation due to DMSO present in the SCB vehicle. The vasodilation seen in the sham group showed that the drastic vasoconstriction seen after SCB exposure was actually diminished due to DMSO.

This work plays a crucial role in advancing several fields of science including biomedical imaging and different branches of developmental biology. Acute vasculature changes in the fetal brain due to maternal exposure to teratogens have not been visualized before. Visualizing and evaluating these changes has opened new avenues for exploration, including the potential of these results to act as a supplement for results obtained at the molecular level and also for the development of novel and innovative therapies for reversing the effects of these teratogens.

From the biomedical imaging perspective, the first part of this dissertation used SVOCT and cm-OCA to image the vasculature. However, they cannot provide quantitative analysis of blood flow. Doppler OCT, on the other hand, can evaluate changes in flow rate and correlate them with changes in the vasculature that were seen in these studies. Doppler OCT will also provide the direction of blood flow that will potentially help us in evaluating the difference, if any, between how maternal teratogen exposure affects flow and morphological changes in the arteries versus veins. Flow rate

quantifications can also be used to calculate other indices such as velocity time integral, acceleration, and Pourcelot resistive index, which in turn can be used to assess cardiac output, cardiac stroke volume, and vascular resistance, respectively.

While the work presented in this dissertation has set up a solid base in terms of imaging and surgical protocols and detailed procedures to quantify and characterize fetal vasculature changes with cellular resolution, only acute exposure to the different teratogens have been presented here. Future work will also involve testing the effects of multiple exposures, combination of different teratogens to simulate poly-drug exposure, and most importantly the use of other noninvasive optical imaging modalities in combination with OCT to extract more functional information.

References

1. M. Levin, "Left–right asymmetry in embryonic development: a comprehensive review," Mechanisms of Development **122**, 3-25 (2005).
2. C. Centers for Disease and Prevention, "Update on overall prevalence of major birth defects--Atlanta, Georgia, 1978-2005," MMWR Morb Mortal Wkly Rep **57**, 1-5 (2008).
3. P. W. Yoon, R. S. Olney, M. J. Khoury, W. M. Sappenfield, G. F. Chavez, and D. Taylor, "Contribution of birth defects and genetic diseases to pediatric hospitalizations. A population-based study," Arch Pediatr Adolesc Med **151**, 1096-1103 (1997).
4. G. SF., "Developmental Biology." (Sinauer Associates, 2000), retrieved https://www.ncbi.nlm.nih.gov/books/NBK10052/.
5. J. A. Rivera-Pérez and A.-K. Hadjantonakis, "The Dynamics of Morphogenesis in the Early Mouse Embryo," Cold Spring Harbor perspectives in biology **7**, a015867 (2014).
6. S. F. Gilbert, "Early mammalian development," in *Developmental Biology*, 6th ed., S. F. Gilbert, ed. (Sinauer Associates Inc., Sunderland (MA), 2000).
7. P. P. L. Tam and R. R. Behringer, "Mouse gastrulation: the formation of a mammalian body plan," Mechanisms of Development **68**, 3-25 (1997).
8. H. Bartlett, G. J. C. Veenstra, and D. L. Weeks, "Examining the cardiac NK-2 genes in early heart development," Pediatric cardiology **31**, 335-341 (2010).
9. R. P. Ji, C. K. L. Phoon, O. Aristizábal, K. E. McGrath, J. Palis, and D. H. Turnbull, "Onset of Cardiac Function During Early Mouse Embryogenesis Coincides With

Entry of Primitive Erythroblasts Into the Embryo Proper," Circulation Research **92**, 133-135 (2003).

10. M. Ema, S. Takahashi, and J. Rossant, "Deletion of the selection cassette, but not cis-acting elements, in targeted Flk1-lacZ allele reveals Flk1 expression in multipotent mesodermal progenitors," Blood **107**, 111-117 (2006).
11. C. J. Drake and P. A. Fleming, "Vasculogenesis in the day 6.5 to 9.5 mouse embryo," Blood **95**, 1671-1679 (2000).
12. T. L. Huber, V. Kouskoff, H. Joerg Fehling, J. Palis, and G. Keller, "Haemangioblast commitment is initiated in the primitive streak of the mouse embryo," Nature **432**, 625-630 (2004).
13. F. le Noble, D. Moyon, L. Pardanaud, L. Yuan, V. Djonov, R. Matthijsen, C. Breant, V. Fleury, and A. Eichmann, "Flow regulates arterial-venous differentiation in the chick embryo yolk sac," Development **131**, 361-375 (2004).
14. J. L. Lucitti, E. A. Jones, C. Huang, J. Chen, S. E. Fraser, and M. E. Dickinson, "Vascular remodeling of the mouse yolk sac requires hemodynamic force," Development **134**, 3317-3326 (2007).
15. Y. Sakai, "Neurulation in the mouse: Manner and timing of neural tube closure," The Anatomical Record **223**, 194-203 (1989).
16. D. Wendler, "[Teratogenic damage of the central nervous system during progressing embryogenesis]," Gegenbaurs Morphol Jahrb **127**, 641-648 (1981).
17. L. D. Botto, C. A. Moore, M. J. Khoury, and J. D. Erickson, "Neural-tube defects," N Engl J Med **341**, 1509-1519 (1999).

18. A. J. Copp and N. D. Greene, "Genetics and development of neural tube defects," J Pathol **220**, 217-230 (2010).

19. A. J. Copp, P. Stanier, and N. D. Greene, "Neural tube defects: recent advances, unsolved questions, and controversies," Lancet Neurol **12**, 799-810 (2013).

20. J. B. Wallingford, L. A. Niswander, G. M. Shaw, and R. H. Finnell, "The continuing challenge of understanding, preventing, and treating neural tube defects," Science (New York, N.Y.) **339**, 1222002-1222002 (2013).

21. M. G. Norman and J. R. O'Kusky, "The growth and development of microvasculature in human cerebral cortex," J Neuropathol Exp Neurol **45**, 222-232 (1986).

22. J. Beckers, W. Wurst, and M. H. de Angelis, "Towards better mouse models: enhanced genotypes, systemic phenotyping and envirotype modelling," Nat Rev Genet **10**, 371-380 (2009).

23. S. D. Brown, J. M. Hancock, and H. Gates, "Understanding mammalian genetic systems: the challenge of phenotyping in the mouse," PLoS Genet **2**, e118 (2006).

24. P. M. Nolan, J. Peters, M. Strivens, D. Rogers, J. Hagan, N. Spurr, I. C. Gray, L. Vizor, D. Brooker, E. Whitehill, R. Washbourne, T. Hough, S. Greenaway, M. Hewitt, X. Liu, S. McCormack, K. Pickford, R. Selley, C. Wells, Z. Tymowska-Lalanne, P. Roby, P. Glenister, C. Thornton, C. Thaung, J. A. Stevenson, R. Arkell, P. Mburu, R. Hardisty, A. Kiernan, A. Erven, K. P. Steel, S. Voegeling, J. L. Guenet, C. Nickols, R. Sadri, M. Nasse, A. Isaacs, K. Davies, M. Browne, E. M. Fisher, J. Martin, S. Rastan, S. D. Brown, and J. Hunter, "A systematic, genome-

wide, phenotype-driven mutagenesis programme for gene function studies in the mouse," Nat Genet **25**, 440-443 (2000).

25. K. Paigen and J. T. Eppig, "A mouse phenome project," Mamm Genome **11**, 715-717 (2000).

26. J. Sharpe, U. Ahlgren, P. Perry, B. Hill, A. Ross, J. Hecksher-Sorensen, R. Baldock, and D. Davidson, "Optical projection tomography as a tool for 3D microscopy and gene expression studies," Science **296**, 541-545 (2002).

27. J. R. Walls, L. Coultas, J. Rossant, and R. M. Henkelman, "Three-dimensional analysis of vascular development in the mouse embryo," PLoS One **3**, e2853 (2008).

28. M. E. Dickinson, "Multimodal imaging of mouse development: tools for the postgenomic era," Dev Dyn **235**, 2386-2400 (2006).

29. E. A. Jones, D. Crotty, P. M. Kulesa, C. W. Waters, M. H. Baron, S. E. Fraser, and M. E. Dickinson, "Dynamic in vivo imaging of postimplantation mammalian embryos using whole embryo culture," Genesis **34**, 228-235 (2002).

30. S. Nowotschin and A. K. Hadjantonakis, "Use of KikGR a photoconvertible green-to-red fluorescent protein for cell labeling and lineage analysis in ES cells and mouse embryos," BMC Dev Biol **9**, 49 (2009).

31. C. K. Phoon and D. H. Turnbull, "Ultrasound biomicroscopy-Doppler in mouse cardiovascular development," Physiol Genomics **14**, 3-15 (2003).

32. F. S. Foster, M. Zhang, A. S. Duckett, V. Cucevic, and C. J. Pavlin, "In vivo imaging of embryonic development in the mouse eye by ultrasound biomicroscopy," Invest Ophthalmol Vis Sci **44**, 2361-2366 (2003).

33. B. Hogers, D. Gross, V. Lehmann, K. Zick, H. J. De Groot, A. C. Gittenberger-De Groot, and R. E. Poelmann, "Magnetic resonance microscopy of mouse embryos in utero," Anat Rec **260**, 373-377 (2000).

34. P. Pallares, M. E. Fernandez-Valle, and A. Gonzalez-Bulnes, "In vivo virtual histology of mouse embryogenesis by ultrasound biomicroscopy and magnetic resonance imaging," Reprod Fertil Dev **21**, 283-292 (2009).

35. B. J. Nieman, N. A. Bock, J. Bishop, X. J. Chen, J. G. Sled, J. Rossant, and R. M. Henkelman, "Magnetic resonance imaging for detection and analysis of mouse phenotypes," NMR Biomed **18**, 447-468 (2005).

36. E. L. Ritman, "Micro-computed tomography-current status and developments," Annu Rev Biomed Eng **6**, 185-208 (2004).

37. M. J. Paulus, S. S. Gleason, S. J. Kennel, P. R. Hunsicker, and D. K. Johnson, "High resolution X-ray computed tomography: an emerging tool for small animal cancer research," Neoplasia **2**, 62-70 (2000).

38. B. Dogdas, D. Stout, A. F. Chatziioannou, and R. M. Leahy, "Digimouse: a 3D whole body mouse atlas from CT and cryosection data," Phys Med Biol **52**, 577-587 (2007).

39. J. F. Colas and J. Sharpe, "Live optical projection tomography," Organogenesis **5**, 211-216 (2009).

40. J. Huisken, J. Swoger, F. Del Bene, J. Wittbrodt, and E. H. K. Stelzer, "Optical Sectioning Deep Inside Live Embryos by Selective Plane Illumination Microscopy," Science **305**, 1007 (2004).

41. P. J. Keller and E. H. Stelzer, "Quantitative in vivo imaging of entire embryos with Digital Scanned Laser Light Sheet Fluorescence Microscopy," Curr Opin Neurobiol **18**, 624-632 (2008).

42. C. Wu, H. Le, S. Ran, M. Singh, I. V. Larina, D. Mayerich, M. E. Dickinson, and K. V. Larin, "Comparison and combination of rotational imaging optical coherence tomography and selective plane illumination microscopy for embryonic study," Biomedical Optics Express **8**, 4629-4639 (2017).

43. D. Huang, E. A. Swanson, C. P. Lin, J. S. Schuman, W. G. Stinson, W. Chang, M. R. Hee, T. Flotte, K. Gregory, C. A. Puliafito, and et al., "Optical coherence tomography," Science **254**, 1178-1181 (1991).

44. J. Chen and L. Lee, "Clinical applications and new developments of optical coherence tomography: an evidence-based review," Clin Exp Optom **90**, 317-335 (2007).

45. J. G. Fujimoto and W. Drexler, "Optical Coherence Tomography: Technology and Applications," (Springer, 2015).

46. I. V. Larina, K. V. Larin, M. J. Justice, and M. E. Dickinson, "Optical Coherence Tomography for live imaging of mammalian development," Curr Opin Genet Dev **21**, 579-584 (2011).

47. M. W. Jenkins, M. Watanabe, and A. M. Rollins, "Longitudinal Imaging of Heart Development With Optical Coherence Tomography," IEEE J Sel Top Quantum Electron **18**, 1166-1175 (2012).

48. J. Men, Y. Huang, J. Solanki, X. Zeng, A. Alex, J. Jerwick, Z. Zhang, R. E. Tanzi, A. Li, and C. Zhou, "Optical Coherence Tomography for Brain Imaging and Developmental Biology," IEEE J Sel Top Quantum Electron **22**(2016).

49. M. D. Garcia, A. L. Lopez, 3rd, K. V. Larin, and I. V. Larina, "Imaging of cardiovascular development in mammalian embryos using optical coherence tomography," Methods Mol Biol **1214**, 151-161 (2015).

50. W. Drexler, H. Sattmann, B. Hermann, T. H. Ko, M. Stur, A. Unterhuber, C. Scholda, O. Findl, M. Wirtitsch, J. G. Fujimoto, and A. F. Fercher, "Enhanced visualization of macular pathology with the use of ultrahigh-resolution optical coherence tomography," Arch Ophthalmol **121**, 695-706 (2003).

51. C. A. Puliafito, M. R. Hee, C. P. Lin, E. Reichel, J. S. Schuman, J. S. Duker, J. A. Izatt, E. A. Swanson, and J. G. Fujimoto, "Imaging of macular diseases with optical coherence tomography," Ophthalmology **102**, 217-229 (1995).

52. E. Sattler, R. Kastle, and J. Welzel, "Optical coherence tomography in dermatology," J Biomed Opt **18**, 061224 (2013).

53. I. K. Jang, B. E. Bouma, D. H. Kang, S. J. Park, S. W. Park, K. B. Seung, K. B. Choi, M. Shishkov, K. Schlendorf, E. Pomerantsev, S. L. Houser, H. T. Aretz, and G. J. Tearney, "Visualization of coronary atherosclerotic plaques in patients using optical coherence tomography: comparison with intravascular ultrasound," J Am Coll Cardiol **39**, 604-609 (2002).

54. I. K. Jang, G. J. Tearney, B. MacNeill, M. Takano, F. Moselewski, N. Iftima, M. Shishkov, S. Houser, H. T. Aretz, E. F. Halpern, and B. E. Bouma, "In vivo

characterization of coronary atherosclerotic plaque by use of optical coherence tomography," Circulation **111**, 1551-1555 (2005).

55. L. L. Otis, M. J. Everett, U. S. Sathyam, and B. W. Colston, Jr., "Optical coherence tomography: a new imaging technology for dentistry," J Am Dent Assoc **131**, 511-514 (2000).

56. A. Nam, B. Vakoc, D. Blauvelt, and I. Chico-Calero, "Optical Coherence Tomography in Cancer Imaging," in *Optical Coherence Tomography*, W. Drexler and J. G. Fujimoto, eds. (Springer International Publishing, 2015), pp. 1399-1412.

57. B. J. Vakoc, D. Fukumura, R. K. Jain, and B. E. Bouma, "Cancer imaging by optical coherence tomography: preclinical progress and clinical potential," Nat Rev Cancer **12**, 363-368 (2012).

58. S. Wang, C. H. Liu, V. P. Zakharov, A. J. Lazar, R. E. Pollock, and K. V. Larin, "Three-dimensional computational analysis of optical coherence tomography images for the detection of soft tissue sarcomas," J Biomed Opt **19**, 21102 (2014).

59. A. F. Fercher, K. Mengedoht, and W. Werner, "Eye-length measurement by interferometry with partially coherent light," Optics Letters **13**, 186-188 (1988).

60. A. F. Fercher, C. K. Hitzenberger, G. Kamp, and S. Y. Elzaiat, "Measurement of Intraocular Distances by Backscattering Spectral Interferometry," Optics Communications **117**, 43-48 (1995).

61. M. A. Choma, M. V. Sarunic, C. Yang, and J. A. Izatt, "Sensitivity advantage of swept source and Fourier domain optical coherence tomography," Optics Express **11**, 2183-2189 (2003).

62. J. F. de Boer, B. Cense, B. H. Park, M. C. Pierce, G. J. Tearney, and B. E. Bouma, "Improved signal-to-noise ratio in spectral-domain compared with time-domain optical coherence tomography," Opt Lett **28**, 2067-2069 (2003).

63. R. Leitgeb, C. K. Hitzenberger, and A. F. Fercher, "Performance of fourier domain vs. time domain optical coherence tomography," Optics Express **11**, 889-894 (2003).

64. H. Spahr, D. Hillmann, C. Hain, C. Pfäffle, H. Sudkamp, G. Franke, and G. Hüttmann, "Imaging pulse wave propagation in human retinal vessels using full-field swept-source optical coherence tomography," Optics Letters **40**, 4771-4774 (2015).

65. X. Wei, A. K. S. Lau, Y. Xu, K. K. Tsia, and K. K. Y. Wong, "28 MHz swept source at 1.0 μm for ultrafast quantitative phase imaging," Biomedical Optics Express **6**, 3855-3864 (2015).

66. S. Wang, D. S. Lakomy, M. D. Garcia, A. L. Lopez, 3rd, K. V. Larin, and I. V. Larina, "Four-dimensional live imaging of hemodynamics in mammalian embryonic heart with Doppler optical coherence tomography," J Biophotonics (2016).

67. R. K. Manapuram, V. G. R. Manne, and K. V. Larin, "Development of phase-stabilized swept-source OCT for the ultrasensitive quantification of microbubbles," Laser Physics **18**, 1080-1086 (2008).

68. R. K. Manapuram, V. G. R. Manne, and K. V. Larin, "Phase-sensitive swept source optical coherence tomography for imaging and quantifying of microbubbles in clear and scattering media," J Appl Phys **105**, 102040 (2009).

69. Z. Chen, T. E. Milner, S. Srinivas, X. Wang, A. Malekafzali, M. J. C. van Gemert, and J. S. Nelson, "Noninvasive imaging of in vivo blood flow velocity using optical Doppler tomography," Optics Letters **22**, 1119-1121 (1997).

70. J. A. Izatt, M. D. Kulkarni, S. Yazdanfar, J. K. Barton, and A. J. Welch, "In vivo bidirectional color Doppler flow imaging of picoliter blood volumes using optical coherence tomography," Opt Lett **22**, 1439-1441 (1997).

71. J. Schmitt, "OCT elastography: imaging microscopic deformation and strain of tissue," Opt Express **3**, 199-211 (1998).

72. S. Wang and K. V. Larin, "Optical coherence elastography for tissue characterization: a review," J Biophotonics **8**, 279-302 (2015).

73. J. F. de Boer and T. E. Milner, "Review of polarization sensitive optical coherence tomography and Stokes vector determination," Journal of Biomedical Optics **7**, 359-371 (2002).

74. J. F. de Boer, T. E. Milner, M. J. C. van Gemert, and J. S. Nelson, "Two-dimensional birefringence imaging in biological tissue by polarization-sensitive optical coherence tomography," Optics Letters **22**, 934-936 (1997).

75. Y. Jiang, I. Tomov, Y. Wang, and Z. Chen, "Second-harmonic optical coherence tomography," Optics Letters **29**, 1090-1092 (2004).

76. R. K. Wang, S. L. Jacques, Z. Ma, S. Hurst, S. R. Hanson, and A. Gruber, "Three dimensional optical angiography," Optics Express **15**, 4083 (2007).

77. A. Zhang, Q. Zhang, C. L. Chen, and R. K. Wang, "Methods and algorithms for optical coherence tomography-based angiography: a review and comparison," J Biomed Opt **20**, 100901 (2015).

78. R. Raghunathan, M. Singh, M. E. Dickinson, and K. V. Larin, "Optical coherence tomography for embryonic imaging: a review," J Biomed Opt **21**, 50902 (2016).

79. S. A. Boppart, M. E. Brezinski, B. E. Bouma, G. J. Tearney, and J. G. Fujimoto, "Investigation of developing embryonic morphology using optical coherence tomography," Dev Biol **177**, 54-63 (1996).

80. S. A. Boppart, B. E. Bouma, M. E. Brezinski, G. J. Tearney, and J. G. Fujimoto, "Imaging developing neural morphology using optical coherence tomography," Journal of Neuroscience Methods **70**, 65-72 (1996).

81. M. E. Brezinski, G. J. Tearney, B. E. Bouma, J. A. Izatt, M. R. Hee, E. A. Swanson, J. F. Southern, and J. G. Fujimoto, "Optical coherence tomography for optical biopsy. Properties and demonstration of vascular pathology," Circulation **93**, 1206-1213 (1996).

82. J. G. Fujimoto, C. Pitris, S. A. Boppart, and M. E. Brezinski, "Optical coherence tomography: an emerging technology for biomedical imaging and optical biopsy," Neoplasia **2**, 9-25 (2000).

83. S. A. Boppart, G. J. Tearney, B. E. Bouma, J. F. Southern, M. E. Brezinski, and J. G. Fujimoto, "Noninvasive assessment of the developing Xenopus cardiovascular system using optical coherence tomography," Proc Natl Acad Sci U S A **94**, 4256-4261 (1997).

84. G. J. Tearney, B. E. Bouma, and J. G. Fujimoto, "High-speed phase- and group-delay scanning with a grating-based phase control delay line," Opt Lett **22**, 1811-1813 (1997).

85. A. Rollins, S. Yazdanfar, M. Kulkarni, R. Ung-Arunyawee, and J. Izatt, "In vivo video rate optical coherence tomography," Opt Express **3**, 219-229 (1998).

86. T. M. Yelbuz, M. A. Choma, L. Thrane, M. L. Kirby, and J. A. Izatt, "Optical coherence tomography: a new high-resolution imaging technology to study cardiac development in chick embryos," Circulation **106**, 2771-2774 (2002).

87. B. A. Filas, I. R. Efimov, and L. A. Taber, "Optical coherence tomography as a tool for measuring morphogenetic deformation of the looping heart," Anat Rec (Hoboken) **290**, 1057-1068 (2007).

88. J. Manner, L. Thrane, K. Norozi, and T. M. Yelbuz, "High-resolution in vivo imaging of the cross-sectional deformations of contracting embryonic heart loops using optical coherence tomography," Dev Dyn **237**, 953-961 (2008).

89. A. Barry, "The functional significance of the cardiac jelly in the tubular heart of the chick embryo," The Anatomical Record **102**, 289-298 (1948).

90. B. C. Groenendijk, B. P. Hierck, J. Vrolijk, M. Baiker, M. J. Pourquie, A. C. Gittenberger-de Groot, and R. E. Poelmann, "Changes in shear stress-related gene expression after experimentally altered venous return in the chicken embryo," Circ Res **96**, 1291-1298 (2005).

91. B. Hogers, M. C. DeRuiter, A. C. Gittenberger-de Groot, and R. E. Poelmann, "Extraembryonic venous obstructions lead to cardiovascular malformations and can be embryolethal," Cardiovasc Res **41**, 87-99 (1999).

92. K. Tobita and B. B. Keller, "Maturation of end-systolic stress-strain relations in chick embryonic myocardium," Am J Physiol Heart Circ Physiol **279**, H216-224 (2000).

93. N. T. Ursem, S. Stekelenburg-de Vos, J. W. Wladimiroff, R. E. Poelmann, A. C. Gittenberger-de Groot, N. Hu, and E. B. Clark, "Ventricular diastolic filling characteristics in stage-24 chick embryos after extra-embryonic venous obstruction," J Exp Biol **207**, 1487-1490 (2004).

94. S. Yazdanfar, M. Kulkarni, and J. Izatt, "High resolution imaging of in vivo cardiac dynamics using color Doppler optical coherence tomography," Opt Express **1**, 424-431 (1997).

95. V. Westphal, S. Yazdanfar, A. M. Rollins, and J. A. Izatt, "Real-time, high velocity-resolution color Doppler optical coherence tomography," Opt Lett **27**, 34-36 (2002).

96. V. Yang, M. Gordon, B. Qi, J. Pekar, S. Lo, E. Seng-Yue, A. Mok, B. Wilson, and I. Vitkin, "High speed, wide velocity dynamic range Doppler optical coherence tomography (Part I): System design, signal processing, and performance," Opt Express **11**, 794-809 (2003).

97. V. X. Yang, M. Gordon, E. Seng-Yue, S. Lo, B. Qi, J. Pekar, A. Mok, B. Wilson, and I. Vitkin, "High speed, wide velocity dynamic range Doppler optical coherence tomography (Part II): Imaging in vivo cardiac dynamics of Xenopus laevis," Opt Express **11**, 1650-1658 (2003).

98. M. W. Jenkins, F. Rothenberg, D. Roy, V. P. Nikolski, Z. Hu, M. Watanabe, D. L. Wilson, I. R. Efimov, and A. M. Rollins, "4D embryonic cardiography using gated optical coherence tomography," Opt Express **14**, 736-748 (2006).

99. M. W. Jenkins, O. Q. Chughtai, A. N. Basavanhally, M. Watanabe, and A. M. Rollins, "In vivo gated 4D imaging of the embryonic heart using optical coherence tomography," J Biomed Opt **12**, 030505 (2007).

100. M. W. Jenkins, P. Patel, H. Deng, M. M. Montano, M. Watanabe, and A. M. Rollins, "Phenotyping transgenic embryonic murine hearts using optical coherence tomography," Appl Opt **46**, 1776-1781 (2007).

101. L. Kagemann, H. Ishikawa, J. Zou, P. Charukamnoetkanok, G. Wollstein, K. A. Townsend, M. L. Gabriele, N. Bahary, X. Wei, J. G. Fujimoto, and J. S. Schuman, "Repeated, noninvasive, high resolution spectral domain optical coherence tomography imaging of zebrafish embryos," Mol Vis **14**, 2157-2170 (2008).

102. K. Divakar Rao, P. Upadhyaya, M. Sharma, and P. K. Gupta, "Noninvasive imaging of ethanol-induced developmental defects in zebrafish embryos using optical coherence tomography," Birth Defects Res B Dev Reprod Toxicol **95**, 7-11 (2012).

103. A. Bradu, L. Ma, J. W. Bloor, and A. Podoleanu, "Dual optical coherence tomography/fluorescence microscopy for monitoring of Drosophila melanogaster larval heart," J Biophotonics **2**, 380-388 (2009).

104. M. Zhenhe, H. Zhonghai, Z. Yuqian, L. Zhigang, and W. Zhaoxia, "Spectral domain optical coherence tomography for embryo heart flow measurement," Procedia Engineering **15**, 5318-5322 (2011).

105. A. M. Davis, F. G. Rothenberg, N. Shepherd, and J. A. Izatt, "In vivo spectral domain optical coherence tomography volumetric imaging and spectral Doppler

velocimetry of early stage embryonic chicken heart development," J Opt Soc Am A Opt Image Sci Vis **25**, 3134-3143 (2008).

106. Z. Ma, A. Liu, X. Yin, A. Troyer, K. Thornburg, R. K. Wang, and S. Rugonyi, "Measurement of absolute blood flow velocity in outflow tract of HH18 chicken embryo based on 4D reconstruction using spectral domain optical coherence tomography," Biomed Opt Express **1**, 798-811 (2010).

107. A. Liu, A. Nickerson, A. Troyer, X. Yin, R. Cary, K. Thornburg, R. Wang, and S. Rugonyi, "Quantifying blood flow and wall shear stresses in the outflow tract of chick embryonic hearts," Comput Struct **89**, 855-867 (2011).

108. A. Liu, X. Yin, L. Shi, P. Li, K. L. Thornburg, R. Wang, and S. Rugonyi, "Biomechanics of the chick embryonic heart outflow tract at HH18 using 4D optical coherence tomography imaging and computational modeling," PLoS One **7**, e40869 (2012).

109. A. P. Liu, R. K. K. Wang, K. L. Thornburg, and S. Rugonyi, "Dynamic variation of hemodynamic shear stress on the walls of developing chick hearts: computational models of the heart outflow tract," Engineering with Computers **25**, 73-86 (2009).

110. M. Midgett, V. K. Chivukula, C. Dorn, S. Wallace, and S. Rugonyi, "Blood flow through the embryonic heart outflow tract during cardiac looping in HH13-HH18 chicken embryos," J R Soc Interface **12**, 20150652 (2015).

111. Z. Ma, S. Dou, Y. Zhao, C. Guo, J. Liu, Q. Wang, T. Xu, R. K. Wang, and Y. Wang, "In vivo assessment of wall strain in embryonic chick heart by spectral domain optical coherence tomography," Appl Opt **54**, 9253-9257 (2015).

112. P. Ma, Y. T. Wang, S. Gu, M. Watanabe, M. W. Jenkins, and A. M. Rollins, "Three-dimensional correction of conduction velocity in the embryonic heart using integrated optical mapping and optical coherence tomography," J Biomed Opt **19**, 76004 (2014).

113. A. L. Lopez, 3rd, S. Wang, K. V. Larin, P. A. Overbeek, and I. V. Larina, "Live four-dimensional optical coherence tomography reveals embryonic cardiac phenotype in mouse mutant," J Biomed Opt **20**, 090501 (2015).

114. S. H. Syed, A. J. Coughlin, M. D. Garcia, S. Wang, J. L. West, K. V. Larin, and I. V. Larina, "Optical coherence tomography guided microinjections in live mouse embryos: high-resolution targeted manipulation for mouse embryonic research," J Biomed Opt **20**, 051020 (2015).

115. K. V. Larin, I. V. Larina, M. Liebling, and M. E. Dickinson, "Live Imaging of Early Developmental Processes in Mammalian Embryos with Optical Coherence Tomography," J Innov Opt Health Sci **2**, 253-259 (2009).

116. S. H. Syed, K. V. Larin, M. E. Dickinson, and I. V. Larina, "Optical coherence tomography for high-resolution imaging of mouse development in utero," J Biomed Opt **16**, 046004 (2011).

117. I. V. Larina, S. H. Syed, N. Sudheendran, P. A. Overbeek, M. E. Dickinson, and K. V. Larin, "Optical coherence tomography for live phenotypic analysis of embryonic ocular structures in mouse models," J Biomed Opt **17**, 081410-081411 (2012).

118. N. Sudheendran, M. Mashiatulla, R. Raghunathan, S. H. Syed, M. E. Dickinson, I. V. Larina, and K. V. Larin, "Quantification of Mouse Embryonic Eye Development

with Optical Coherence Tomography In Utero," Journal of Biomedical Photonics & Engineering **1**, 90-95 (2015).

119. N. Sudheendran, S. Bake, R. C. Miranda, and K. V. Larin, "Comparative assessments of the effects of alcohol exposure on fetal brain development using optical coherence tomography and ultrasound imaging," J Biomed Opt **18**, 20506 (2013).

120. I. V. Larina, N. Sudheendran, M. Ghosn, J. Jiang, A. Cable, K. V. Larin, and M. E. Dickinson, "Live imaging of blood flow in mammalian embryos using Doppler swept-source optical coherence tomography," J Biomed Opt **13**, 060506 (2008).

121. I. V. Larina, S. Ivers, S. Syed, M. E. Dickinson, and K. V. Larin, "Hemodynamic measurements from individual blood cells in early mammalian embryos with Doppler swept source OCT," Opt Lett **34**, 986-988 (2009).

122. N. Sudheendran, S. H. Syed, M. E. Dickinson, I. V. Larina, and K. V. Larin, "Speckle variance OCT imaging of the vasculature in live mammalian embryos," Laser Physics Letters **8**, 247-252 (2011).

123. A. Mariampillai, B. A. Standish, E. H. Moriyama, M. Khurana, N. R. Munce, M. K. Leung, J. Jiang, A. Cable, B. C. Wilson, I. A. Vitkin, and V. X. Yang, "Speckle variance detection of microvasculature using swept-source optical coherence tomography," Opt Lett **33**, 1530-1532 (2008).

124. D. C. Adler, R. Huber, and J. G. Fujimoto, "Phase-sensitive optical coherence tomography at up to 370,000 lines per second using buffered Fourier domain mode-locked lasers," Optics Letters **32**, 626-628 (2007).

125. M. Gargesha, M. W. Jenkins, D. L. Wilson, and A. M. Rollins, "High temporal resolution OCT using image-based retrospective gating," Optics Express **17**, 10786-10799 (2009).

126. R. Huber, D. C. Adler, and J. G. Fujimoto, "Buffered Fourier domain mode locking: unidirectional swept laser sources for optical coherence tomography imaging at 370,000 lines/s," Optics Letters **31**, 2975-2977 (2006).

127. M. W. Jenkins, D. C. Adler, M. Gargesha, R. Huber, F. Rothenberg, J. Belding, M. Watanabe, D. L. Wilson, J. G. Fujimoto, and A. M. Rollins, "Ultrahigh-speed optical coherence tomography imaging and visualization of the embryonic avian heart using a buffered Fourier Domain Mode Locked laser," Opt Express **15**, 6251-6267 (2007).

128. M. W. Jenkins, L. Peterson, S. Gu, M. Gargesha, D. L. Wilson, M. Watanabe, and A. M. Rollins, "Measuring hemodynamics in the developing heart tube with four-dimensional gated Doppler optical coherence tomography," J Biomed Opt **15**, 066022 (2010).

129. B. Garita, M. W. Jenkins, M. Han, C. Zhou, M. Vanauker, A. M. Rollins, M. Watanabe, J. G. Fujimoto, and K. K. Linask, "Blood flow dynamics of one cardiac cycle and relationship to mechanotransduction and trabeculation during heart looping," Am J Physiol Heart Circ Physiol **300**, H879-891 (2011).

130. S. Gu, M. W. Jenkins, L. M. Peterson, Y. Q. Doughman, A. M. Rollins, and M. Watanabe, "Optical coherence tomography captures rapid hemodynamic responses to acute hypoxia in the cardiovascular system of early embryos," Dev Dyn **241**, 534-544 (2012).

131. S. Bhat, I. V. Larina, K. V. Larin, M. E. Dickinson, and M. Liebling, "4D reconstruction of the beating embryonic heart from two orthogonal sets of parallel optical coherence tomography slice-sequences," IEEE Trans Med Imaging **32**, 578-588 (2013).

132. I. V. Larina, K. V. Larin, M. E. Dickinson, and M. Liebling, "Sequential Turning Acquisition and Reconstruction (STAR) method for four-dimensional imaging of cyclically moving structures," Biomed Opt Express **3**, 650-660 (2012).

133. J. Yoo, I. V. Larina, K. V. Larin, M. E. Dickinson, and M. Liebling, "Increasing the field-of-view of dynamic cardiac OCT via post-acquisition mosaicing without affecting frame-rate or spatial resolution," Biomed Opt Express **2**, 2614-2622 (2011).

134. C. Wu, N. Sudheendran, M. Singh, I. V. Larina, M. E. Dickinson, and K. V. Larin, "Rotational imaging optical coherence tomography for full-body mouse embryonic imaging," J Biomed Opt **21**, 26002 (2016).

135. A. H. Kashani, C.-L. Chen, J. K. Gahm, F. Zheng, G. M. Richter, P. J. Rosenfeld, Y. Shi, and R. K. Wang, "Optical coherence tomography angiography: A comprehensive review of current methods and clinical applications," Progress in Retinal and Eye Research **60**, 66-100 (2017).

136. C. L. Chen and R. K. Wang, "Optical coherence tomography based angiography [Invited]," Biomed Opt Express **8**, 1056-1082 (2017).

137. J. K. Barton and S. Stromski, "Flow measurement without phase information in optical coherence tomography images," Optics Express **13**, 5234-5239 (2005).

138. J. Schmitt, S. Xiang, and K. Yung, "Speckle in optical coherence tomography," Journal of Biomedical Optics **4**(1999).

139. K. W. Gossage, T. S. Tkaczyk, J. J. Rodriguez, and J. K. Barton, "Texture analysis of optical coherence tomography images: feasibility for tissue classification," J Biomed Opt **8**, 570-575 (2003).

140. D. A. Zimnyakov, V. V. Tuchin, and A. A. Mishin, "Spatial speckle correlometry in applications to tissue structure monitoring," Appl Opt **36**, 5594-5607 (1997).

141. L. Guo, P. Li, C. Pan, R. Liao, Y. Cheng, W. Hu, Z. Chen, Z. Ding, and P. Li, "Improved motion contrast and processing efficiency in OCT angiography using complex-correlation algorithm," Journal of Optics **18**, 025301 (2015).

142. S. Makita, K. Kurokawa, Y. J. Hong, M. Miura, and Y. Yasuno, "Noise-immune complex correlation for optical coherence angiography based on standard and Jones matrix optical coherence tomography," Biomed Opt Express **7**, 1525-1548 (2016).

143. A. Forray, "Substance use during pregnancy," F1000Res **5**, F1000 Faculty Rev-1887 (2016).

144. S. H. Ebrahim and J. Gfroerer, "Pregnancy-related substance use in the United States during 1996-1998," Obstet Gynecol **101**, 374-379 (2003).

145. E. M. Howell, N. Heiser, and M. Harrington, "A Review of Recent Findings on Substance Abuse Treatment for Pregnant Women," Journal of Substance Abuse Treatment **16**, 195-219 (1999).

146. M. Behnke and V. C. Smith, "Prenatal Substance Abuse: Short- and Long-term Effects on the Exposed Fetus," Pediatrics **131**, e1009 (2013).

147. R. F. Becker, C. R. Little, and J. E. King, "Experimental studies on nicotine absorption in rats during pregnancy. 3. Effect of subcutaneous injection of small chronic doses upon mother, fetus, and neonate," Am J Obstet Gynecol **100**, 957-968 (1968).

148. K. Jones and D. Smith, "RECOGNITION OF THE FETAL ALCOHOL SYNDROME IN EARLY INFANCY," The Lancet **302**, 999-1001 (1973).

149. K. L. Jones, D. W. Smith, C. N. Ulleland, and P. Streissguth, "Pattern of malformation in offspring of chronic alcoholic mothers," Lancet **1**, 1267-1271 (1973).

150. L. P. Finnegan, "Pathophysiological and behavioural effects of the transplacental transfer of narcotic drugs to the foetuses and neonates of narcotic-dependent mothers," Bull Narc **31**, 1-58 (1979).

151. I. J. Chasnoff, W. J. Burns, S. H. Schnoll, and K. A. Burns, "Cocaine Use in Pregnancy," New England Journal of Medicine **313**, 666-669 (1985).

152. P. A. Fried, "Postnatal consequences of maternal marijuana use in humans," Ann N Y Acad Sci **562**, 123-132 (1989).

153. A. S. Oro and S. D. Dixon, "Perinatal cocaine and methamphetamine exposure: maternal and neonatal correlates," J Pediatr **111**, 571-578 (1987).

154. F. S. Stinson, B. F. Grant, D. A. Dawson, W. J. Ruan, B. Huang, and T. Saha, "Comorbidity between DSM-IV alcohol and specific drug use disorders in the United States: results from the National Epidemiologic Survey on Alcohol and Related Conditions," Drug Alcohol Depend **80**, 105-116 (2005).

155. W. M. Compton, Y. F. Thomas, F. S. Stinson, and B. F. Grant, "Prevalence, correlates, disability, and comorbidity of DSM-IV drug abuse and dependence in the United States: results from the national epidemiologic survey on alcohol and related conditions," Arch Gen Psychiatry **64**, 566-576 (2007).

156. H. El Marroun, H. Tiemeier, V. W. Jaddoe, A. Hofman, J. P. Mackenbach, E. A. Steegers, F. C. Verhulst, W. van den Brink, and A. C. Huizink, "Demographic, emotional and social determinants of cannabis use in early pregnancy: the Generation R study," Drug Alcohol Depend **98**, 218-226 (2008).

157. M. E. Passey, R. W. Sanson-Fisher, C. A. D'Este, and J. M. Stirling, "Tobacco, alcohol and cannabis use during pregnancy: clustering of risks," Drug Alcohol Depend **134**, 44-50 (2014).

158. R. Caleyachetty, C. A. Tait, A. P. Kengne, C. Corvalan, R. Uauy, and J. B. Echouffo-Tcheugui, "Tobacco use in pregnant women: analysis of data from Demographic and Health Surveys from 54 low-income and middle-income countries," The Lancet Global Health **2**, e513-e520 (2014).

159. P. Petersen Williams, E. Jordaan, C. Mathews, C. Lombard, and C. D. Parry, "Alcohol and Other Drug Use during Pregnancy among Women Attending Midwife Obstetric Units in the Cape Metropole, South Africa," Adv Prev Med **2014**, 871427 (2014).

160. P. G. Higgins, D. H. Clough, B. Frank, and C. Wallerstedt, "Changes in health behaviors made by pregnant substance users," Int J Addict **30**, 1323-1333 (1995).

161. A. Forray, B. Merry, H. Lin, J. P. Ruger, and K. A. Yonkers, "Perinatal substance use: a prospective evaluation of abstinence and relapse," Drug Alcohol Depend **150**, 147-155 (2015).

162. J. F. Williams and V. C. Smith, "Fetal Alcohol Spectrum Disorders," Pediatrics **136**, e1395 (2015).

163. S. Roozen, G. J. Peters, G. Kok, D. Townend, J. Nijhuis, and L. Curfs, "Worldwide Prevalence of Fetal Alcohol Spectrum Disorders: A Systematic Literature Review Including Meta-Analysis," Alcohol Clin Exp Res **40**, 18-32 (2016).

164. J. H. Hannigan and D. R. Armant, "Alcohol in pregnancy and neonatal outcome," Semin Neonatol **5**, 243-254 (2000).

165. J. Cornman-Homonoff, D. Kuehn, S. Aros, T. C. Carter, M. R. Conley, J. Troendle, F. Cassorla, and J. L. Mills, "Heavy prenatal alcohol exposure and risk of stillbirth and preterm delivery," J Matern Fetal Neonatal Med **25**, 860-863 (2012).

166. S. Balaraman, J. J. Schafer, A. M. Tseng, W. Wertelecki, L. Yevtushok, N. Zymak-Zakutnya, C. D. Chambers, and R. C. Miranda, "Plasma miRNA Profiles in Pregnant Women Predict Infant Outcomes following Prenatal Alcohol Exposure," PLOS ONE **11**, e0165081 (2016).

167. L. B. Finer and M. R. Zolna, "Declines in Unintended Pregnancy in the United States, 2008-2011," N Engl J Med **374**, 843-852 (2016).

168. M. T. Fillmore and R. Jude, "Defining "binge" drinking as five drinks per occasion or drinking to a .08% BAC: which is more sensitive to risk?," Am J Addict **20**, 468-475 (2011).

169. SAMHSA, "The NSDUH Report: 18 percent of pregnant women drink alcohol during early pregnancy.," NSDUH Report (2013).

170. A. D. Workman, C. J. Charvet, B. Clancy, R. B. Darlington, and B. L. Finlay, "Modeling transformations of neurodevelopmental sequences across mammalian species," J Neurosci **33**, 7368-7383 (2013).

171. C. Camarillo and R. C. Miranda, "Ethanol exposure during neurogenesis induces persistent effects on neural maturation: evidence from an ex vivo model of fetal cerebral cortical neuroepithelial progenitor maturation," Gene Expr **14**, 159-171 (2008).

172. D. R. Santillano, L. S. Kumar, T. L. Prock, C. Camarillo, J. D. Tingling, and R. C. Miranda, "Ethanol induces cell-cycle activity and reduces stem cell diversity to alter both regenerative capacity and differentiation potential of cerebral cortical neuroepithelial precursors," BMC Neuroscience **6**, 59 (2005).

173. S. D. Vangipuram, W. E. Grever, G. C. Parker, and W. D. Lyman, "Ethanol increases fetal human neurosphere size and alters adhesion molecule gene expression," Alcohol Clin Exp Res **32**, 339-347 (2008).

174. C. F. Bearer, "L1 cell adhesion molecule signal cascades: targets for ethanol developmental neurotoxicity," Neurotoxicology **22**, 625-633 (2001).

175. C. Lebel, F. Roussotte, and E. R. Sowell, "Imaging the Impact of Prenatal Alcohol Exposure on the Structure of the Developing Human Brain," Neuropsychology Review **21**, 102-118 (2011).

176. C. Guerri, A. Bazinet, and E. P. Riley, "Foetal Alcohol Spectrum Disorders and Alterations in Brain and Behaviour," Alcohol and Alcoholism **44**, 108-114 (2009).

177. S. N. Mattson and E. P. Riley, "A Review of the Neurobehavioral Deficits in Children with Fetal Alcohol Syndrome or Prenatal Exposure to Alcohol," Alcoholism: Clinical and Experimental Research **22**, 279-294 (1998).

178. T. M. Roebuck, S. N. Mattson, and E. P. Riley, "Behavioral and psychosocial profiles of alcohol-exposed children," Alcohol Clin Exp Res **23**(1999).

179. M. Carta, M. Mameli, and C. F. Valenzuela, "Alcohol potently modulates climbing fiber-->Purkinje neuron synapses: role of metabotropic glutamate receptors," J Neurosci **26**, 1906-1912 (2006).

180. J. R. West, S. E. Parnell, W. J. Chen, and T. A. Cudd, "Alcohol-mediated Purkinje cell loss in the absence of hypoxemia during the third trimester in an ovine model system," Alcohol Clin Exp Res **25**, 1051-1057 (2001).

181. A. L. Fowden and A. J. Forhead, "Endocrine regulation of feto-placental growth," Horm Res **72**, 257-265 (2009).

182. S. J. Tam and R. J. Watts, "Connecting vascular and nervous system development: angiogenesis and the blood-brain barrier," Annu Rev Neurosci **33**, 379-408 (2010).

183. S. Bake, J. D. Tingling, and R. C. Miranda, "Ethanol exposure during pregnancy persistently attenuates cranially directed blood flow in the developing fetus: evidence from ultrasound imaging in a murine second trimester equivalent model," Alcohol Clin Exp Res **36**, 748-758 (2012).

184. S. E. Parnell, J. Ramadoss, M. D. Delp, M. W. Ramsey, W.-J. A. Chen, J. R. West, and T. A. Cudd, "Chronic ethanol increases fetal cerebral blood flow specific to the ethanol-sensitive cerebellum under normoxaemic, hypercapnic and acidaemic conditions: ovine model," Experimental Physiology **92**, 933-943 (2007).

185. E. Muggli, H. Matthews, A. Penington, P. Claes, C. O'Leary, D. Forster, S. Donath, P. J. Anderson, S. Lewis, C. Nagle, J. M. Craig, S. M. White, E. J. Elliott, and J. Halliday, "Association Between Prenatal Alcohol Exposure and Craniofacial Shape of Children at 12 Months of Age," JAMA Pediatr **171**, 771-780 (2017).

186. R. Waltman and E. S. Iniquez, "Placental transfer of ethanol and its elimination at term," Obstet Gynecol **40**, 180-185 (1972).

187. L. Burd, J. Blair, and K. Dropps, "Prenatal alcohol exposure, blood alcohol concentrations and alcohol elimination rates for the mother, fetus and newborn," J Perinatol **32**, 652-659 (2012).

188. P. H. Pikkarainen, "Metabolism of ethanol and acetaldehyde in perfused human fetal liver," Life Sci II **10**, 1359-1364 (1971).

189. K. M. Poole, D. R. McCormack, C. A. Patil, C. L. Duvall, and M. C. Skala, "Quantifying the vascular response to ischemia with speckle variance optical coherence tomography," Biomedical Optics Express **5**, 4118-4130 (2014).

190. J. D. Fewings, M. J. Hanna, J. A. Walsh, and R. F. Whelan, "The effects of ethyl alcohol on the blood vessels of the hand and forearm in man," British journal of pharmacology and chemotherapy **27**, 93-106 (1966).

191. J. L. Short, J. Drago, and A. J. Lawrence, "Comparison of ethanol preference and neurochemical measures of mesolimbic dopamine and adenosine systems across different strains of mice," Alcohol Clin Exp Res **30**, 606-620 (2006).

192. P. A. Daft, M. C. Johnston, and K. K. Sulik, "Abnormal heart and great vessel development following acute ethanol exposure in mice," Teratology **33**, 93-104 (1986).

193. R. P. Ji, C. K. Phoon, O. Aristizabal, K. E. McGrath, J. Palis, and D. H. Turnbull, "Onset of cardiac function during early mouse embryogenesis coincides with entry of primitive erythroblasts into the embryo proper," Circ Res **92**, 133-135 (2003).

194. M. Serrano, M. Han, P. Brinez, and K. K. Linask, "Fetal alcohol syndrome: cardiac birth defects in mice and prevention with folate," Am J Obstet Gynecol **203**, 75.e77-75.e15 (2010).

195. P. Drake, A. K. Driscoll, and T. J. Mathews, "Cigarette Smoking During Pregnancy: United States, 2016," NCHS Data Brief, 1-8 (2018).

196. B. Haglund and S. Cnattingius, "Cigarette smoking as a risk factor for sudden infant death syndrome: a population-based study," Am J Public Health **80**, 29-32 (1990).

197. C. T. Orleans, D. C. Barker, N. J. Kaufman, and J. F. Marx, "Helping pregnant smokers quit: meeting the challenge in the next decade," Tob Control **9 Suppl 3**, III6-11 (2000).

198. P. H. Persson, L. Grennert, G. Gennser, and S. Kullander, "A study of smoking and pregnancy with special references to fetal growth," Acta Obstet Gynecol Scand Suppl **78**, 33-39 (1978).

199. H. S. Bada, A. Das, C. R. Bauer, S. Shankaran, B. M. Lester, C. C. Gard, L. L. Wright, L. Lagasse, and R. Higgins, "Low birth weight and preterm births: etiologic fraction attributable to prenatal drug exposure," J Perinatol **25**, 631-637 (2005).

200. V. Conter, I. Cortinovis, P. Rogari, and L. Riva, "Weight growth in infants born to mothers who smoked during pregnancy," BMJ **310**, 768-771 (1995).

201. B. M. D'Onofrio, E. N. Turkheimer, L. J. Eaves, L. A. Corey, K. Berg, M. H. Solaas, and R. E. Emery, "The role of the children of twins design in elucidating causal

relations between parent characteristics and child outcomes," J Child Psychol Psychiatry **44**, 1130-1144 (2003).

202. V. S. Knopik, E. P. Sparrow, P. A. Madden, K. K. Bucholz, J. J. Hudziak, W. Reich, W. S. Slutske, J. D. Grant, T. L. McLaughlin, A. Todorov, R. D. Todd, and A. C. Heath, "Contributions of parental alcoholism, prenatal substance exposure, and genetic transmission to child ADHD risk: a female twin study," Psychol Med **35**, 625-635 (2005).

203. N. B. Kyrklund-Blomberg, F. Granath, and S. Cnattingius, "Maternal smoking and causes of very preterm birth," Acta Obstet Gynecol Scand **84**, 572-577 (2005).

204. L. M. McCowan, G. A. Dekker, E. Chan, A. Stewart, L. C. Chappell, M. Hunter, R. Moss-Morris, R. A. North, and S. consortium, "Spontaneous preterm birth and small for gestational age infants in women who stop smoking early in pregnancy: prospective cohort study," BMJ **338**, b1081 (2009).

205. H. M. Salihu, M. H. Aliyu, and R. S. Kirby, "In utero nicotine exposure and fetal growth inhibition among twins," Am J Perinatol **22**, 421-427 (2005).

206. L. R. Stroud, R. L. Paster, M. S. Goodwin, E. Shenassa, S. Buka, R. Niaura, J. F. Rosenblith, and L. P. Lipsitt, "Maternal smoking during pregnancy and neonatal behavior: a large-scale community study," Pediatrics **123**, e842-e848 (2009).

207. G. Thiriez, M. Bouhaddi, L. Mourot, F. Nobili, J. O. Fortrat, A. Menget, P. Franco, and J. Regnard, "Heart rate variability in preterm infants and maternal smoking during pregnancy," Clin Auton Res **19**, 149-156 (2009).

208. G. L. Bell and K. Lau, "Perinatal and neonatal issues of substance abuse," Pediatr Clin North Am **42**, 261-281 (1995).

209. N. R. Butler and H. Goldstein, "Smoking in pregnancy and subsequent child development," British medical journal **4**, 573-575 (1973).

210. M. D. Cornelius, C. M. Ryan, N. L. Day, L. Goldschmidt, and J. A. Willford, "Prenatal tobacco effects on neuropsychological outcomes among preadolescents," J Dev Behav Pediatr **22**, 217-225 (2001).

211. J. R. DiFranza and R. A. Lew, "Effect of maternal cigarette smoking on pregnancy complications and sudden infant death syndrome," J Fam Pract **40**, 385-394 (1995).

212. H. G. Dunn and A. K. McBurney, "Cigarette Smoking and the Fetus and Child," Pediatrics **60**, 772 (1977).

213. M. S. Indredavik, A.-M. Brubakk, P. Romundstad, and T. Vik, "Prenatal smoking exposure and psychiatric symptoms in adolescence," Acta paediatrica (Oslo, Norway : 1992) **96**, 377-382 (2007).

214. M. M. Lefkowitz, "Smoking during pregnancy: Long-term effects on offspring," Developmental Psychology **17**, 192-194 (1981).

215. R. L. Naeye, "Effects of maternal cigarette smoking on the fetus and placenta," Br J Obstet Gynaecol **85**, 732-737 (1978).

216. R. L. Naeye, "Cognitive and behavioral abnormalities in children whose mothers smoked cigarettes during pregnancy," J Dev Behav Pediatr **13**, 425-428 (1992).

217. R. L. Naeye and E. C. Peters, "Mental development of children whose mothers smoked during pregnancy," Obstet Gynecol **64**, 601-607 (1984).

218. J. F. Orlebeke, D. L. Knol, and F. C. Verhulst, "Child behavior problems increased by maternal smoking during pregnancy," Arch Environ Health **54**, 15-19 (1999).

219. A. R. Piquero, C. L. Gibson, S. G. Tibbetts, M. G. Turner, and S. H. Katz, "Maternal cigarette smoking during pregnancy and life-course-persistent offending," Int J Offender Ther Comp Criminol **46**, 231-248 (2002).

220. L. S. Wakschlag, K. E. Pickett, E. Cook, Jr., N. L. Benowitz, and B. L. Leventhal, "Maternal smoking during pregnancy and severe antisocial behavior in offspring: a review," Am J Public Health **92**, 966-974 (2002).

221. M. Weitzman, R. S. Byrd, C. A. Aligne, and M. Moss, "The effects of tobacco exposure on children's behavioral and cognitive functioning: implications for clinical and public health policy and future research," Neurotoxicol Teratol **24**, 397-406 (2002).

222. J. E. Bruin, H. C. Gerstein, and A. C. Holloway, "Long-term consequences of fetal and neonatal nicotine exposure: a critical review," Toxicol Sci **116**, 364-374 (2010).

223. L. M. Ebert and K. Fahy, "Why do women continue to smoke in pregnancy?," Women Birth **20**, 161-168 (2007).

224. L. Ruggiero, J. Y. Tsoh, K. Everett, J. L. Fava, and B. J. Guise, "The transtheoretical model of smoking: comparison of pregnant and nonpregnant smokers," Addict Behav **25**, 239-251 (2000).

225. T. Coleman, J. Britton, and J. Thornton, "Nicotine replacement therapy in pregnancy," BMJ **328**, 965-966 (2004).

226. T. Coleman, S. Cooper, J. G. Thornton, M. J. Grainge, K. Watts, J. Britton, and S. Lewis, "A Randomized Trial of Nicotine-Replacement Therapy Patches in Pregnancy," New England Journal of Medicine **366**, 808-818 (2012).

227. C. A. Oncken, L. Pbert, J. K. Ockene, J. Zapka, and A. Stoddard, "Nicotine replacement prescription practices of obstetric and pediatric clinicians," Obstetrics & Gynecology **96**, 261-265 (2000).

228. L. F. Stead, R. Perera, C. Bullen, D. Mant, J. Hartmann-Boyce, K. Cahill, and T. Lancaster, "Nicotine replacement therapy for smoking cessation," Cochrane Database of Systematic Reviews (2012).

229. K. S. Mark, B. Farquhar, M. S. Chisolm, V. H. Coleman-Cowger, and M. Terplan, "Knowledge, Attitudes, and Practice of Electronic Cigarette Use Among Pregnant Women," J Addict Med **9**, 266-272 (2015).

230. L. Porter, J. Duke, M. Hennon, D. Dekevich, E. Crankshaw, G. Homsi, and M. Farrelly, "Electronic Cigarette and Traditional Cigarette Use among Middle and High School Students in Florida, 2011-2014," PLoS One **10**, e0124385 (2015).

231. T. A. Wills, R. Knight, R. J. Williams, I. Pagano, and J. D. Sargent, "Risk Factors for Exclusive E-Cigarette Use and Dual E-Cigarette Use and Tobacco Use in Adolescents," Pediatrics **135**, e43 (2015).

232. N. Gray, J. E. Henningfield, N. L. Benowitz, G. N. Connolly, C. Dresler, K. Fagerstrom, M. J. Jarvis, and P. Boyle, "Toward a comprehensive long term nicotine policy," Tobacco Control **14**, 161 (2005).

233. D. A. Dempsey and N. L. Benowitz, "Risks and benefits of nicotine to aid smoking cessation in pregnancy," Drug Saf **24**, 277-322 (2001).

234. E. R. Spindel and C. T. McEvoy, "The Role of Nicotine in the Effects of Maternal Smoking during Pregnancy on Lung Development and Childhood Respiratory

Disease. Implications for Dangers of E-Cigarettes," American Journal of Respiratory and Critical Care Medicine **193**, 486-494 (2016).

235. K. E. Farsalinos, A. Spyrou, C. Stefopoulos, K. Tsimopoulou, P. Kourkoveli, D. Tsiapras, S. Kyrzopoulos, K. Poulas, and V. Voudris, "Nicotine absorption from electronic cigarette use: comparison between experienced consumers (vapers) and naive users (smokers)," Sci Rep **5**, 11269 (2015).

236. S. Talih, Z. Balhas, T. Eissenberg, R. Salman, N. Karaoghlanian, A. El Hellani, R. Baalbaki, N. Saliba, and A. Shihadeh, "Effects of user puff topography, device voltage, and liquid nicotine concentration on electronic cigarette nicotine yield: measurements and model predictions," Nicotine Tob Res **17**, 150-157 (2015).

237. C. A. Oncken and H. R. Kranzler, "Pharmacotherapies to enhance smoking cessation during pregnancy," Drug Alcohol Rev **22**, 191-202 (2003).

238. J. M. Lauder, "Roles for neurotransmitters in development: possible interaction with drugs during the fetal and neonatal periods," Prog Clin Biol Res **163C**, 375-380 (1985).

239. P. M. Whitaker-Azmitia, "Role of serotonin and other neurotransmitter receptors in brain development: basis for developmental pharmacology," Pharmacol Rev **43**, 553-561 (1991).

240. T. A. Slotkin, "If nicotine is a developmental neurotoxicant in animal studies, dare we recommend nicotine replacement therapy in pregnant women and adolescents?," Neurotoxicol Teratol **30**, 1-19 (2008).

241. E. D. Levin and T. A. Slotkin, "Developmental neurotoxicity of nicotine," in *Handbook of developmental neurotoxicology* (Elsevier, 1998), pp. 587-615.

242. H. A. Navarro, F. J. Seidler, R. D. Schwartz, F. E. Baker, S. S. Dobbins, and T. A. Slotkin, "Prenatal exposure to nicotine impairs nervous system development at a dose which does not affect viability or growth," Brain Res Bull **23**, 187-192 (1989).

243. H. A. Navarro, F. J. Seidler, W. L. Whitmore, and T. A. Slotkin, "Prenatal exposure to nicotine via maternal infusions: effects on development of catecholamine systems," J Pharmacol Exp Ther **244**, 940-944 (1988).

244. W. Slikker, Jr., Z. A. Xu, E. D. Levin, and T. A. Slotkin, "Mode of action: disruption of brain cell replication, second messenger, and neurotransmitter systems during development leading to cognitive dysfunction--developmental neurotoxicity of nicotine," Crit Rev Toxicol **35**, 703-711 (2005).

245. T. Slotkin, "Prenatal exposure to nicotine: what can we learn from animal models? Maternal Substance Abuse and the Developing Nervous System," Zagon IS, Slotkin TA (1992).

246. T. Slotkin, E. McCook, and F. Seidler, "Cryptic brain cell injury caused by fetal nicotine exposure is associated with persistent elevations of c-fos protooncogene expression," Brain research **750**, 180-188 (1997).

247. T. Slotkin, L. Orband-Miller, and K. Queen, "Development of [3H] nicotine binding sites in brain regions of rats exposed to nicotine prenatally via maternal injections or infusions," Journal of Pharmacology and Experimental Therapeutics **242**, 232-237 (1987).

248. T. A. Slotkin, "Fetal nicotine or cocaine exposure: which one is worse?," Journal of pharmacology and experimental therapeutics **285**, 931-945 (1998).

249. T. A. Slotkin, "Cholinergic systems in brain development and disruption by neurotoxicants: nicotine, environmental tobacco smoke, organophosphates," Toxicology and applied pharmacology **198**, 132-151 (2004).

250. J. A. Trauth, F. J. Seidler, E. C. McCook, and T. A. Slotkin, "Persistent c-fos induction by nicotine in developing rat brain regions: interaction with hypoxia," Pediatric research **45**, 38-45 (1999).

251. T. Slotkin, "Developmental cholinotoxicants: nicotine and chlorpyrifos Environ Health Perspect 107 (suppl 1): 71–80," Find this article online (1999).

252. B. Naeff, M. Schlumpf, and W. Lichtensteiger, "Pre-and postnatal development of high-affinity [3H] nicotine binding sites in rat brain regions: an autoradiographic study," Developmental brain research **68**, 163-174 (1992).

253. P. Atluri, M. Fleck, Q. Shen, S. Mah, D. Stadfelt, W. Barnes, S. Goderie, S. Temple, and A. Schneider, "Functional nicotinic acetylcholine receptor expression in stem and progenitor cells of the early embryonic mouse cerebral cortex," Developmental biology **240**, 143-156 (2001).

254. A. Schneider, P. Atluri, Q. Shen, W. Barnes, S. Mah, D. Stadfelt, S. Goderie, S. Temple, and M. Fleck, "Functional nicotinic acetylcholine receptor expression on stem and progenitor cells of the early embryonic nervous system," Annals of the New York Academy of Sciences **971**, 135-138 (2002).

255. T. Roy and U. Sabherwal, "Effects of gestational nicotine exposure on hippocampal morphology," Neurotoxicology and teratology **20**, 465-473 (1998).

256. J. C. Damborsky, W. H. Griffith, and U. H. Winzer-Serhan, "Chronic neonatal nicotine exposure increases excitation in the young adult rat hippocampus in a sex-dependent manner," Brain Res **1430**, 8-17 (2012).

257. L. Z. Huang, S. H. Hsiao, J. Trzeciakowski, G. D. Frye, and U. H. Winzer-Serhan, "Chronic nicotine induces growth retardation in neonatal rat pups," Life Sci **78**, 1483-1493 (2006).

258. L. C. Murrin, J. R. Ferrer, W. Y. Zeng, and N. J. Haley, "Nicotine administration to rats: methodological considerations," Life Sci **40**, 1699-1708 (1987).

259. L. C. Abbott and U. H. Winzer-Serhan, "Smoking during pregnancy: lessons learned from epidemiological studies and experimental studies using animal models," Crit Rev Toxicol **42**, 279-303 (2012).

260. A. Harris and J. Seckl, "Glucocorticoids, prenatal stress and the programming of disease," Horm Behav **59**, 279-289 (2011).

261. T. A. Slotkin, T. A. Epps, M. L. Stenger, K. J. Sawyer, and F. J. Seidler, "Cholinergic receptors in heart and brainstem of rats exposed to nicotine during development: implications for hypoxia tolerance and perinatal mortality," Brain Res Dev Brain Res **113**, 1-12 (1999).

262. E. T. Korgun, A. Ozmen, G. Unek, and I. Mendilcioglu, "The effects of glucocorticoids on fetal and placental development," Glucocorticoids-New Recognition of Our Familiar Friend (2012).

263. K. Muneoka, T. Ogawa, K. Kamei, S.-i. Muraoka, R. Tomiyoshi, Y. Mimura, H. Kato, M. R. Suzuki, and M. Takigawa, "Prenatal nicotine exposure affects the development of the central serotonergic system as well as the dopaminergic system

in rat offspring: involvement of route of drug administrations," Developmental Brain Research **102**, 117-126 (1997).

264. R. Graignic-Philippe, J. Dayan, S. Chokron, A. Y. Jacquet, and S. Tordjman, "Effects of prenatal stress on fetal and child development: A critical literature review," Neuroscience & Biobehavioral Reviews **43**, 137-162 (2014).

265. N. L. Benowitz, "Nicotine and Cardiovascular Disease," in *Effects of Nicotine on Biological Systems*, F. Adlkofer and K. Thurau, eds. (Birkhäuser Basel, Basel, 1991), pp. 579-596.

266. N. L. Benowitz, "The Role of Nicotine in Smoking-Related Cardiovascular Disease," Preventive Medicine **26**, 412-417 (1997).

267. T. J. Dickerson and K. D. Janda, "A previously undescribed chemical link between smoking and metabolic disease," Proceedings of the National Academy of Sciences **99**, 15084 (2002).

268. D. E. Falk, H.-y. Yi, and S. Hiller-Sturmhöfel, "An epidemiologic analysis of co-occurring alcohol and tobacco use and disorders: findings from the National Epidemiologic Survey on Alcohol and Related Conditions," Alcohol Research & Health **29**, 162 (2006).

269. D. Kandel, K. Chen, L. A. Warner, R. C. Kessler, and B. Grant, "Prevalence and demographic correlates of symptoms of last year dependence on alcohol, nicotine, marijuana and cocaine in the US population," Drug and alcohol dependence **44**, 11-29 (1997).

270. J. E. McCabe and S. Arndt, "Demographic and substance abuse trends among pregnant and non-pregnant women: eleven years of treatment admission data," Matern Child Health J **16**, 1696-1702 (2012).

271. M. S. Castaneto, D. A. Gorelick, N. A. Desrosiers, R. L. Hartman, S. Pirard, and M. A. Huestis, "Synthetic cannabinoids: epidemiology, pharmacodynamics, and clinical implications," Drug Alcohol Depend **144**, 12-41 (2014).

272. S. Tai and W. E. Fantegrossi, "Synthetic Cannabinoids: Pharmacology, Behavioral Effects, and Abuse Potential," Curr Addict Rep **1**, 129-136 (2014).

273. E. W. Gunderson, H. M. Haughey, N. Ait-Daoud, A. S. Joshi, and C. L. Hart, ""Spice" and "K2" herbal highs: a case series and systematic review of the clinical effects and biopsychosocial implications of synthetic cannabinoid use in humans," Am J Addict **21**, 320-326 (2012).

274. B. Mills, A. Yepes, and K. Nugent, "Synthetic Cannabinoids," Am J Med Sci **350**, 59-62 (2015).

275. C. S. Breivogel and S. R. Childers, "Cannabinoid agonist signal transduction in rat brain: comparison of cannabinoid agonists in receptor binding, G-protein activation, and adenylyl cyclase inhibition," J Pharmacol Exp Ther **295**, 328-336 (2000).

276. L. J. Sim, R. E. Hampson, S. A. Deadwyler, and S. R. Childers, "Effects of chronic treatment with delta9-tetrahydrocannabinol on cannabinoid-stimulated [35S]GTPgammaS autoradiography in rat brain," J Neurosci **16**, 8057-8066 (1996).

277. Q. Tao and M. E. Abood, "Mutation of a highly conserved aspartate residue in the second transmembrane domain of the cannabinoid receptors, CB1 and CB2, disrupts G-protein coupling," J Pharmacol Exp Ther **285**, 651-658 (1998).

278. K. A. Seely, P. L. Prather, L. P. James, and J. H. Moran, "Marijuana-based drugs: innovative therapeutics or designer drugs of abuse?," Mol Interv **11**, 36-51 (2011).

279. L. Fattore and W. Fratta, "Beyond THC: The New Generation of Cannabinoid Designer Drugs," Front Behav Neurosci **5**, 60 (2011).

280. H. L. Brown and C. R. Graves, "Smoking and marijuana use in pregnancy," Clin Obstet Gynecol **56**, 107-113 (2013).

281. D. Calvigioni, Y. L. Hurd, T. Harkany, and E. Keimpema, "Neuronal substrates and functional consequences of prenatal cannabis exposure," Eur Child Adolesc Psychiatry **23**, 931-941 (2014).

282. B. D. Holbrook and W. F. Rayburn, "Teratogenic risks from exposure to illicit drugs," Obstet Gynecol Clin North Am **41**, 229-239 (2014).

283. E. Papaseit, M. Farre, F. Schifano, and M. Torrens, "Emerging drugs in Europe," Curr Opin Psychiatry **27**, 243-250 (2014).

284. A. B. Schneir, J. Cullen, and B. T. Ly, ""Spice" girls: synthetic cannabinoid intoxication," J Emerg Med **40**, 296-299 (2011).

285. J. R. Bailey, H. C. Cunny, M. G. Paule, and W. Slikker, Jr., "Fetal disposition of delta 9-tetrahydrocannabinol (THC) during late pregnancy in the rhesus monkey," Toxicol Appl Pharmacol **90**, 315-321 (1987).

286. D. E. Hutchings, B. R. Martin, Z. Gamagaris, N. Miller, and T. Fico, "Plasma concentrations of delta-9-tetrahydrocannabinol in dams and fetuses following acute or multiple prenatal dosing in rats," Life Sci **44**, 697-701 (1989).

287. A. Garry, V. Rigourd, A. Amirouche, V. Fauroux, S. Aubry, and R. Serreau, "Cannabis and breastfeeding," J Toxicol **2009**, 596149 (2009).

288. M. Perez-Reyes and M. E. Wall, "Presence of delta9-tetrahydrocannabinol in human milk," N Engl J Med **307**, 819-820 (1982).

289. J. Begbie, P. Doherty, and A. Graham, "Cannabinoid receptor, CB1, expression follows neuronal differentiation in the early chick embryo," J Anat **205**, 213-218 (2004).

290. N. E. Buckley, S. Hansson, G. Harta, and E. Mezey, "Expression of the CB1 and CB2 receptor messenger RNAs during embryonic development in the rat," Neuroscience **82**, 1131-1149 (1998).

291. D. Psychoyos, K. Y. Vinod, J. Cao, S. Xie, R. L. Hyson, B. Wlodarczyk, W. He, T. B. Cooper, B. L. Hungund, and R. H. Finnell, "Cannabinoid receptor 1 signaling in embryo neurodevelopment," Birth Defects Res B Dev Reprod Toxicol **95**, 137-150 (2012).

292. D. Psychoyos, B. Hungund, T. Cooper, and R. H. Finnell, "A cannabinoid analogue of Delta9-tetrahydrocannabinol disrupts neural development in chick," Birth Defects Res B Dev Reprod Toxicol **83**, 477-488 (2008).

293. W. F. Geber and L. C. Schramm, "Effect of marihuana extract on fetal hamsters and rabbits," Toxicol Appl Pharmacol **14**, 276-282 (1969).

294. T. V. Persaud and A. C. Ellington, "Cannabis in early pregnancy," Lancet **2**, 1306 (1967).

295. T. Harkany, M. Guzman, I. Galve-Roperh, P. Berghuis, L. A. Devi, and K. Mackie, "The emerging functions of endocannabinoid signaling during CNS development," Trends Pharmacol Sci **28**, 83-92 (2007).

296. M. T. Gilbert, K. K. Sulik, E. W. Fish, L. K. Baker, D. B. Dehart, and S. E. Parnell, "Dose-dependent teratogenicity of the synthetic cannabinoid CP-55,940 in mice," Neurotoxicol Teratol **58**, 15-22 (2016).

297. U. Off, "Drugs Crime (UNODC). 2019," World drug report 2019.

298. J. S. Hayes, R. Lampart, M. C. Dreher, and L. Morgan, "Five-year follow-up of rural Jamaican children whose mothers used marijuana during pregnancy," West Indian Med J **40**, 120-123 (1991).

299. D. M. Morrison, M. S. Spencer, and M. R. Gillmore, "Beliefs about substance use among pregnant and parenting adolescents," J Res Adolesc **8**, 69-95 (1998).

300. P. Campolongo, V. Trezza, P. Ratano, M. Palmery, and V. Cuomo, "Developmental consequences of perinatal cannabis exposure: behavioral and neuroendocrine effects in adult rodents," Psychopharmacology **214**, 5-15 (2011).

301. M. R. Hayatbakhsh, A. M. Kingsbury, V. Flenady, K. S. Gilshenan, D. M. Hutchinson, and J. M. Najman, "Illicit drug use before and during pregnancy at a tertiary maternity hospital 2000-2006," Drug Alcohol Rev **30**, 181-187 (2011).

302. B. Bar-Oz, J. Klein, T. Karaskov, and G. Koren, "Comparison of meconium and neonatal hair analysis for detection of gestational exposure to drugs of abuse," Archives of disease in childhood. Fetal and neonatal edition **88**, F98-F100 (2003).

303. R. D. Harbison, B. Mantilla-Plata, and D. J. Lubin, "Alteration of delta 9-tetrahydrocannabinol-induced teratogenicity by stimulation and inhibition of its metabolism," J Pharmacol Exp Ther **202**, 455-465 (1977).

304. J. Schou, L. D. Prockop, G. Dahlstrom, and C. Rohde, "Penetration of delta-9-tetrahydrocannabinol and 11-OH-delta-9-tetrahydrocannabinol through the blood-brain barrier," Acta Pharmacol Toxicol (Copenh) **41**, 33-38 (1977).

305. R. Raghunathan, C. Wu, M. Singh, C. H. Liu, R. C. Miranda, and K. V. Larin, "Evaluating the effects of maternal alcohol consumption on murine fetal brain vasculature using optical coherence tomography," J Biophotonics **11**, e201700238 (2018).

306. T. Kaneda, N. Sasaki, N. Urakawa, and K. Shimizu, "Endothelium-Dependent and -Independent Vasodilator Effects of Dimethyl Sulfoxide in Rat Aorta," Pharmacology **97**, 171-176 (2016).

307. L. K. Wong and E. L. Reinertson, "Clinical Considerations of Dimethyl Sulfoxide," Iowa State University Veterinarian **46**(1984).

308. G. T. Gibson, P. A. Baghurst, and D. P. Colley, "Maternal alcohol, tobacco and cannabis consumption and the outcome of pregnancy," Aust N Z J Obstet Gynaecol **23**, 15-19 (1983).

309. H. J. Blom, G. M. Shaw, M. den Heijer, and R. H. Finnell, "Neural tube defects and folate: case far from closed," Nat Rev Neurosci **7**, 724-731 (2006).

310. R. J. Lemire, "Neural Tube Defects," JAMA **259**, 558-562 (1988).

311. S. Wang, M. D. Garcia, A. L. Lopez, 3rd, P. A. Overbeek, K. V. Larin, and I. V. Larina, "Dynamic imaging and quantitative analysis of cranial neural tube closure

in the mouse embryo using optical coherence tomography," Biomed Opt Express **8**, 407-419 (2017).

312. E. Nikolopoulou, G. L. Galea, A. Rolo, N. D. E. Greene, and A. J. Copp, "Neural tube closure: cellular, molecular and biomechanical mechanisms," Development (Cambridge, England) **144**, 552-566 (2017).

313. D. S. Vijayraghavan and L. A. Davidson, "Mechanics of neurulation: From classical to current perspectives on the physical mechanics that shape, fold, and form the neural tube," Birth Defects Research **109**, 153-168 (2017).

314. J. Zhou, S. Pal, S. Maiti, and L. A. Davidson, "Force production and mechanical accommodation during convergent extension," Development **142**, 692-701 (2015).

315. T. Zulueta-Coarasa and R. Fernandez-Gonzalez, "Laser ablation to investigate cell and tissue mechanics in vivo," in *Integrative Mechanobiology: Micro- and Nano-Techniques in Cell Mechanobiology*, C. A. Simmons, D.-H. Kim, and Y. Sun, eds. (Cambridge University Press, Cambridge, 2015), pp. 110-127.

316. L. V. Beloussov, J. G. Dorfman, and V. G. Cherdantzev, "Mechanical stresses and morphological patterns in amphibian embryos," J Embryol Exp Morphol **34**, 559-574 (1975).

317. R. David, O. Luu, E. W. Damm, J. W. Wen, M. Nagel, and R. Winklbauer, "Tissue cohesion and the mechanics of cell rearrangement," Development **141**, 3672-3682 (2014).

318. O. Luu, R. David, H. Ninomiya, and R. Winklbauer, "Large-scale mechanical properties of Xenopus embryonic epithelium," Proc Natl Acad Sci U S A **108**, 4000-4005 (2011).

319. A. R. Moore and A. S. Burt, "On the locus and nature of the forces causing gastrulation in the embryos of Dendraster excentricus," J Exp Zool **82**, 159-171 (1939).

320. K. K. Chiou, L. Hufnagel, and B. I. Shraiman, "Mechanical stress inference for two dimensional cell arrays," PLoS Comput Biol **8**, e1002512 (2012).

321. S. Ishihara and K. Sugimura, "Bayesian inference of force dynamics during morphogenesis," J Theor Biol **313**, 201-211 (2012).

322. K. Sugimura and S. Ishihara, "The mechanical anisotropy in a tissue promotes ordering in hexagonal cell packing," Development **140**, 4091-4101 (2013).

323. A. Chaigne, C. Campillo, N. S. Gov, R. Voituriez, J. Azoury, C. Umaña-Diaz, M. Almonacid, I. Queguiner, P. Nassoy, C. Sykes, M.-H. Verlhac, and M.-E. Terret, "A soft cortex is essential for asymmetric spindle positioning in mouse oocytes," Nat Cell Biol **15**, 958-966 (2013).

324. J. L. Maitre, R. Niwayama, H. Turlier, F. Nedelec, and T. Hiiragi, "Pulsatile cell-autonomous contractility drives compaction in the mouse embryo," Nat Cell Biol **17**, 849-855 (2015).

325. M. von Dassow, J. A. Strother, and L. A. Davidson, "Surprisingly simple mechanical behavior of a complex embryonic tissue," PLoS One **5**, e15359 (2010).

326. J. Wen, J. Liu, K. Lau, H. Liu, S. Hopyan, and Y. Sun, "Automated micro-aspiration of mouse embryo limb bud tissue," in *Proceedings - IEEE International Conference on Robotics and Automation*, 2015), 2667-2672.

327. R. Feroze, J. H. Shawky, M. von Dassow, and L. A. Davidson, "Mechanics of blastopore closure during amphibian gastrulation," Dev Biol **398**, 57-67 (2015).

328. Y. Hara, K. Nagayama, T. S. Yamamoto, T. Matsumoto, M. Suzuki, and N. Ueno, "Directional migration of leading-edge mesoderm generates physical forces: Implication in Xenopus notochord formation during gastrulation," Dev Biol **382**, 482-495 (2013).

329. M. Krieg, Y. Arboleda-Estudillo, P. H. Puech, J. Kafer, F. Graner, D. J. Muller, and C. P. Heisenberg, "Tensile forces govern germ-layer organization in zebrafish," Nat Cell Biol **10**, 429-436 (2008).

330. N. Desprat, W. Supatto, P. A. Pouille, E. Beaurepaire, and E. Farge, "Tissue deformation modulates twist expression to determine anterior midgut differentiation in Drosophila embryos," Dev Cell **15**, 470-477 (2008).

331. E. Farge, "Mechanical induction of Twist in the Drosophila foregut/stomodeal primordium," Curr Biol **13**, 1365-1377 (2003).

332. B. A. Filas, G. Xu, and L. A. Taber, "Probing Regional Mechanical Properties of Embryonic Tissue Using Microindentation and Optical Coherence Tomography," in *Tissue Morphogenesis: Methods and Protocols*, C. M. Nelson, ed. (Springer New York, New York, NY, 2015), pp. 3-16.

333. E. A. Zamir and L. A. Taber, "Material Properties and Residual Stress in the Stage 12 Chick Heart During Cardiac Looping," J Biomech Eng **126**, 823 (2004).

334. K. Bambardekar, R. Clement, O. Blanc, C. Chardes, and P. F. Lenne, "Direct laser manipulation reveals the mechanics of cell contacts in vivo," Proc Natl Acad Sci U S A **112**, 1416-1421 (2015).

335. G. F. Weber, M. A. Bjerke, and D. W. DeSimone, "A mechanoresponsive cadherin-keratin complex directs polarized protrusive behavior and collective cell migration," Dev Cell **22**, 104-115 (2012).

336. A. D. Wessel, M. Gumalla, J. Grosshans, and C. F. Schmidt, "The mechanical properties of early Drosophila embryos measured by high-speed video microrheology," Biophys J **108**, 1899-1907 (2015).

337. D. Cai, S. C. Chen, M. Prasad, L. He, X. Wang, V. Choesmel-Cadamuro, J. K. Sawyer, G. Danuser, and D. J. Montell, "Mechanical feedback through E-cadherin promotes direction sensing during collective cell migration," Cell **157**, 1146-1159 (2014).

338. O. Campas, T. Mammoto, S. Hasso, R. A. Sperling, D. O'Connell, A. G. Bischof, R. Maas, D. A. Weitz, L. Mahadevan, and D. E. Ingber, "Quantifying cell-generated mechanical forces within living embryonic tissues," Nat Methods **11**, 183-189 (2014).

339. N. R. Chevalier, E. Gazguez, S. Dufour, and V. Fleury, "Measuring the micromechanical properties of embryonic tissues," Methods **94**, 120-128 (2016).

340. J. Park, J. Lee, S. T. Lau, C. Lee, Y. Huang, C. L. Lien, and K. Kirk Shung, "Acoustic radiation force impulse (ARFI) imaging of zebrafish embryo by high-frequency coded excitation sequence," Ann Biomed Eng **40**, 907-915 (2012).

341. B. F. Kennedy, P. Wijesinghe, and D. D. Sampson, "The emergence of optical elastography in biomedicine," Nat Photon **11**, 215-221 (2017).

342. G. Scarcelli and S. H. Yun, "Confocal Brillouin microscopy for three-dimensional mechanical imaging," Nat Photonics **2**, 39-43 (2008).

343. G. Scarcelli, P. Kim, and Seok H. Yun, "In Vivo Measurement of Age-Related Stiffening in the Crystalline Lens by Brillouin Optical Microscopy," Biophys J **101**, 1539-1545 (2011).

344. G. Scarcelli, R. Pineda, and S. H. Yun, "Brillouin Optical Microscopy for Corneal Biomechanics," Invest. Ophthalmol. Vis. Sci. **53**, 185-190 (2012).

345. G. Scarcelli and S. H. Yun, "In vivo Brillouin optical microscopy of the human eye," Opt. Express **20**, 9197-9202 (2012).

346. F. Palombo, C. P. Winlove, R. S. Edginton, E. Green, N. Stone, S. Caponi, M. Madami, and D. Fioretto, "Biomechanics of fibrous proteins of the extracellular matrix studied by Brillouin scattering," J. R. Soc. Interface **11**(2014).

347. G. Antonacci and S. Braakman, "Biomechanics of subcellular structures by non-invasive Brillouin microscopy," Sci. Rep. **6**, 37217 (2016).

348. K. Elsayad, S. Werner, M. Gallemi, J. Kong, E. R. Sanchez Guajardo, L. Zhang, Y. Jaillais, T. Greb, and Y. Belkhadir, "Mapping the subcellular mechanical properties of live cells in tissues with fluorescence emission-Brillouin imaging," Sci Signal **9**, rs5 (2016).

349. G. Scarcelli, W. J. Polacheck, H. T. Nia, K. Patel, A. J. Grodzinsky, R. D. Kamm, and S. H. Yun, "Noncontact three-dimensional mapping of intracellular hydromechanical properties by Brillouin microscopy," Nat Methods **12**, 1132-1134 (2015).

350. J. Zhang, X. A. Nou, H. Kim, and G. Scarcelli, "Brillouin flow cytometry for label-free mechanical phenotyping of the nucleus," Lab Chip **17**, 663-670 (2017).

351. J. Zhang, R. Raghunathan, J. Rippy, C. Wu, R. H. Finnell, K. V. Larin, and G. Scarcelli, "Tissue biomechanics during cranial neural tube closure measured by Brillouin microscopy and optical coherence tomography," Birth Defects Res **111**, 991-998 (2019).

352. S. G. McShane, M. A. Mole, D. Savery, N. D. Greene, P. P. Tam, and A. J. Copp, "Cellular basis of neuroepithelial bending during mouse spinal neural tube closure," Dev Biol **404**, 113-124 (2015).

353. D. E. Koser, E. Moeendarbary, J. Hanne, S. Kuerten, and K. Franze, "CNS cell distribution and axon orientation determine local spinal cord mechanical properties," Biophys J **108**, 2137-2147 (2015).

354. I. P. Weber, S. H. Yun, G. Scarcelli, and K. Franze, "The role of cell body density in ruminant retina mechanics assessed by atomic force and Brillouin microscopy," Physical biology **14**, 065006-065006 (2017).

355. R. Barer and S. Joseph, "Refractometry of Living Cells," Quarterly Journal of Microscopical Science **s3-95**, 399 (1954).

356. M. Schurmann, J. Scholze, P. Muller, J. Guck, and C. J. Chan, "Cell nuclei have lower refractive index and mass density than cytoplasm," J Biophotonics **9**, 1068-1076 (2016).

357. E. Edrei and G. Scarcelli, "Brillouin micro-spectroscopy through aberrations via sensorless adaptive optics," Applied Physics Letters **112**, 163701 (2018).

358. R. M. Cabrera, D. S. Hill, A. J. Etheredge, and R. H. Finnell, "Investigations into the etiology of neural tube defects," Birth Defects Research Part C: Embryo Today: Reviews **72**, 330-344 (2004).

First Author Journal Publications

1. **R. Raghunathan**, M. Singh, M. E. Dickinson, and K. V. Larin, "Optical coherence tomography for embryonic imaging: a review," J Biomed Opt 21, 50902 (2016).
2. **R. Raghunathan**, J. Zhang, C. Wu, J. Rippy, M. Singh, K. V. Larin, and G. Scarcelli, "Evaluating biomechanical properties of murine embryos using Brillouin microscopy and optical coherence tomography," J Biomed Opt 22, 1-6 (2017). (**Equal Contribution**)
3. **R. Raghunathan**, C. Wu, M. Singh, C. H. Liu, R. C. Miranda, and K. V. Larin, "Evaluating the effects of maternal alcohol consumption on murine fetal brain vasculature using optical coherence tomography," J Biophotonics 11, e201700238 (2018). (**Equal Contribution**)
4. J. Zhang, **R. Raghunathan**, J. Rippy, C. Wu, R. H. Finnell, K. V. Larin, and G. Scarcelli, "Tissue biomechanics during cranial neural tube closure measured by Brillouin microscopy and optical coherence tomography," Birth Defects Res 111, 991-998 (2019). (**Equal Contribution**)
5. **R. Raghunathan**, C. H. Liu, A. Kouka, M. Singh, R. C. Miranda, and K. V. Larin, "Assessing the acute effects of prenatal synthetic cannabinoid exposure on murine fetal brain vasculature using optical coherence tomography," J Biophotonics 12, e201900050 (2019).
6. **R. Raghunathan**, C. H. Liu, Y. S. Ambekar, M. Singh, R. C. Miranda, and K. V. Larin, "Optical coherence tomography angiography to evaluate murine fetal brain

vasculature changes caused by prenatal exposure to nicotine," Biomed Opt Express (submitted, April 2020).

7. **R. Raghunathan**, C. H. Liu, A. Kouka, M. Singh, R. C. Miranda, and K. V. Larin, "Dose response analysis of vasculature changes in the murine fetal brain due to prenatal ethanol exposure," (in preparation, 2020).

Appendix- A1- OCT system schematic

A phase-stabilized swept source OCT system (PhS-SSOCT) was used for cm-OCA imaging. The system composed of a swept source laser (HSL2000, Santec, Inc., USA) of central wavelength 1310 nm, scan range of 150 nm, A-scan rate of 30 kHz, output power of ~39 mW, and axial resolution of 11 µm in air. The interference pattern was recorded by a balanced photodetector and digitized by a high-speed analog-to-digital converter. After resampling the raw interference pattern into linear k-space, a fast Fourier transform was performed on the fringe to obtain a 1D depth profile, called the A-scan. The axial and transverse resolutions were ~11 µm and ~15 µm, respectively, and the phase stability of the system was experimentally measured as ~16 mrad in air. Using a scanning galvanometer-mounted mirror, 2D cross-sectional image was constructed, called a B-scan. Further details can be found in a previous publication [67].

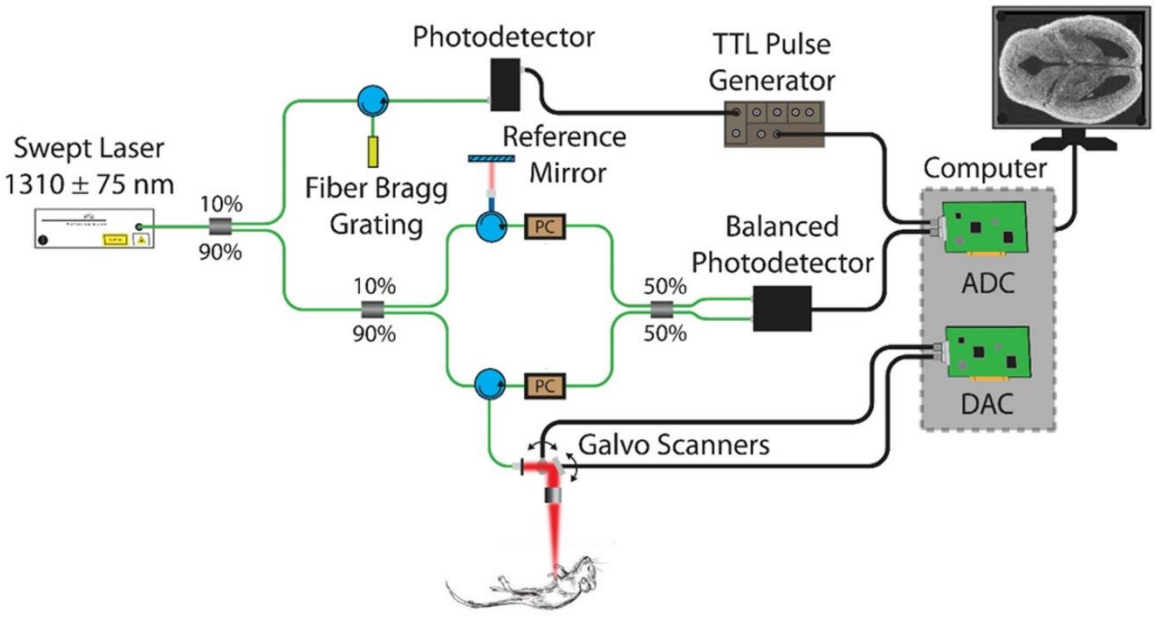

Figure A1.1 Experimental schematic, including the OCT system.

Appendix- A2- Animal manipulations

All procedures were performed under an approved protocol by the University of Houston Institutional Animal Care and Use committee. The animals were housed in an AALAC-accredited animal facility at the University of Houston on a 12 hours light/dark cycle with ad libitum access to food and water. CD-1 mice were set up for mating and the presence of a vaginal plug was considered gestational day (GD) 0.5. At GD 14.5, pregnant mice were anesthetized by isoflurane inhalation and placed on a heated surgical platform at 37^{0}C for the entire duration of the procedure. The depth of maternal anesthesia was maintained with continuous isoflurane exposure until the last measurement. Abdominal fur was removed, and a small incision was made in the abdomen to expose the uterine horn for imaging. Once the fetus was selected for imaging, it was stabilized using forceps to minimize bulk motion due to maternal respiration and heartbeat. Initial OCT measurements were recorded, and the mother was administered the drug being tested or the corresponding solution for the sham group. Subsequent OCT measurements were taken for a period 45 minutes at 5-minute intervals. Except for the results shown in section 2.3.1, for all the other experiments, the uterus was hydrated with 1XPBS 1 minute before every measurement. After all the measurements were completed, the animal was euthanized by isoflurane overdose followed by cervical dislocation.

Appendix- A3- Biomechanical mapping of early murine fetal development

The first part of this dissertation was focused on imaging and evaluating changes in the developing fetal brain vasculature due to prenatal exposure to teratogens in the second trimester equivalent in a mouse model. This final section will focus on the first trimester imaging. Neurulation is one of the earliest processes in fetal development which involves the flat neural plate rolling up and closing to form the neural tube. Failure in proper neural tube closure can lead to neural tube defects and hence abnormal brain development. The process of neural tube closure is driven by mechanical forces and hence mere structural imaging is insufficient to understand the effects of teratogens. A quantitative evaluation of changes in biomechanical properties of the developing tissue would provide a better understanding of the process of the neural tube closure along with structural imaging. Hence, this section focuses on preliminary studies conducted on combining OCT with Brillouin microscopy to image neural tube closure and hence the effect of teratogens.

14.1 Introduction

One of the earliest processes in fetal development, that later leads to the formation of the brain is neural tube closure (NTC). Failure in this process leads to neural tube defects (NTDs) [17-20, 309, 310], which is one of the main causes of congenital defects. Even with an incidence of 1 in 1000 pregnancies [17, 310], the etiology of NTDs is still largely unknown. Additionally, some studies have shown that NTDs can be caused by exposure to specific teratogens.

Imaging the process of NTC has been an important area of study for quite some time. In 2017, OCT was used for the first time for live imaging of murine NTC [311]. The process of closure involves shaping, bending, and fusion of the neural plates followed by the propagation of the closure along the body axis [312]. Just like cardiac development, the process of neural tube closure is driven by mechanical forces, driven by underlying cellular processes. These biomechanical processes are dependent on the generated internal forces and the stiffness of the fetal tissue [312-314]. Thus, it is important to understand how the tissue deforms and reshapes during neural tube closure.

Several *in vitro* and *in vivo* techniques have been used to measure the mechanical properties of developing embryos. Some of these techniques include laser ablation [315], tissue dissection and relaxation [316-319], force inference [320-322], micropipette aspiration [323-326], cantilevers and atomic force microscopy (AFM) [327-329], microindenters and microplates [330-333], 3D traction force microscopy [314], optical tweezers (OT) [334], magnetic tweezers [335], microrheology [336], Forster resonance energy transfer- based tension sensors [337], and droplet-based sensors (DS) [338]. All these techniques have revealed valuable information about the mechanophysiology of fetal development. However, some are invasive, involve the use of external contrast agents, or have poor spatial and temporal resolutions. For example, microindentation and AFM require physical contact with the sample while force inference cannot provide quantitative material properties. On the other hand, OT and DS provide quantitative information, but require microinjections of external contrast agents or involve complex calibrations.

Different forms of elastography like AFM elastography [339], optical coherence elastography (OCE) [332], and acoustic radiation force impulse (ARFI) imaging [340]

have been used to study the biomechanics of embryos. However, resolution constraints for subcellular imaging with OCE and ARFI and the need for external loading to induce deformations might have detrimental effects on the developing embryo or may induce additional perturbations to the already existing mechanical forces.

Brillouin microscopy has gained popularity recently for tissue and cellular biomechanical assessments [341, 342]. It is an all optical method that probes the mechanical properties of a material via light scattering where the interaction between an incoming photon and acoustic waves generated from fluctuations within the sample creates a very minute frequency shift in the scattered light. This frequency shift, called the Brillouin shift, is directly linked to the longitudinal modulus of the material. Brillouin microscopy can achieve submicron resolution with the use of a high numerical aperture (NA) objective lenses and does not require any external loading during measurements. Brillouin microscopy has been used to characterize various tissues, such as the crystalline lens and cornea [343-345], the measurement of fibrous proteins of extracellular matrix [346], and to map cellular and subcellular mechanics of live cells [347-350].

This section describes preliminary studies done probing the biomechanical changes that occur during neural tube closure with the combined use of OCT and Brillouin microscopy to study the effects of teratogens on NTC. OCT provided structural guidance so that Brillouin microscopy could effectively measure the stiffness changes in embryonic tissues.

14.2 Materials and methods

14.2.1 Animal manipulations

Timed mating of CD-1 mice were set up and the presence of a vaginal plug was considered gestational day (GD) 0.5. On the day of imaging, the mother was euthanized by carbon dioxide inhalation and the embryos were dissected out. They were first imaged using OCT. Then the embryos were transported to the University of Maryland, where they were imaged using Brillouin microscopy within 24 hours of dissection. Initially, the embryos were kept in 0.9% saline during imaging and transported. Next, the embryos were embedded in 1% agarose with PBS before imaging, to maintain the same orientation of the embryo while imaging by both imaging modalities. The first study involved imaging the entire embryo at one developmental stage (GD 8.5) to measure the stiffness of different organs at the same stage of development. The second study focused on imaging the neural tube region at two different developmental stages (GD 8.5 and GD 9.5). Since the second study was focused on imaging the neural tube region alone, embedding the embryos in agarose helped ensure imaging was performed on the same region of the neural tube with both imaging modalities. A total of 5 embryos were imaged for the first study at GD 8.5. For the second study, two embryos each for GD 8.5 and GD 9.5 were imaged. The embryos were kept cold, but not frozen during transportation and were brought back to room temperature before imaging.

14.2.2 Brillouin microscope

The Brillouin microscopy set up (shown in Figure 14.1) was built by coupling a Brillouin spectrometer with a confocal microscope. The laser source was a single-mode

linearly polarized 532-nm continuous wave laser (Torus, Laser Quantum) with an output power of approximately 10 mW. After passing through a half-wave plate and a polarizer, the polarization of the laser beam was aligned to the input polarization of the polarized beam splitter. The beam was then focused onto the sample with an objective lens (NA = 0.6, and magnification = 40x) with a spot size of ~0.5 µm x ~0.5 µm x ~2 µm. The back-scattered light was collected by the same objective and coupled into a Brillouin spectrometer through a fiber coupler. A combination of a quarter-wave plate and a polarized beam splitter was used to ensure that all the scattered light collected by the objective lens was delivered into the spectrometer. The Brillouin spectrometer consisted of a two-stage virtually imaged phase array in cross-axis configuration. The Brillouin spectrometer was calibrated before and after experiments using standard materials with known Brillouin frequency shift. For the experiments, the embryo samples were placed onto a glass bottom dish and surrounded by the medium. Brillouin images were acquired by scanning the sample with the help of an automated 3D stage, with a step size of 5µm. The parameters of the Brillouin system were slightly modified for the second study. More details can be found here [351].

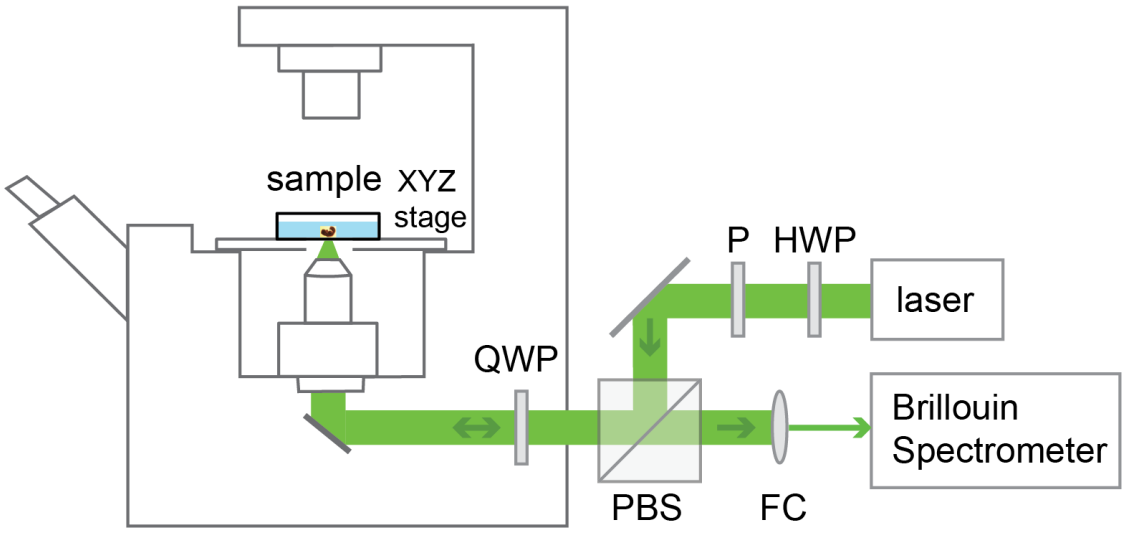

Figure A3.1 Schematic of Brillouin microscopy setup. HWP: half-wave plate; P: polarizer; PBS: polarization beam splitter; QWP: quarter-wave plate; FC: fiber coupler.

14.2.3 OCT system

A home-built OCT system consisting of a swept source laser (HSL2000, Santec USA, Corp., Hackensack, New Jersey) with a central wavelength of ~1310 nm, scan range of ~150 nm, A-scan rate of ~30 kHz, output power of ~39 mW. The OCT system had an axial resolution of ~11 µm (in air) and transverse resolution of ~16 µm. More details of the OCT imaging system are provided in previous work[67]. Figure 14.2 shows a schematic of the OCT system used. Five A-scans were recorded at each location and A-scan averaging was performed to increase the SNR. The images were corrected to physical dimensions assuming that the refractive indices of saline and the embryos were 1.38.

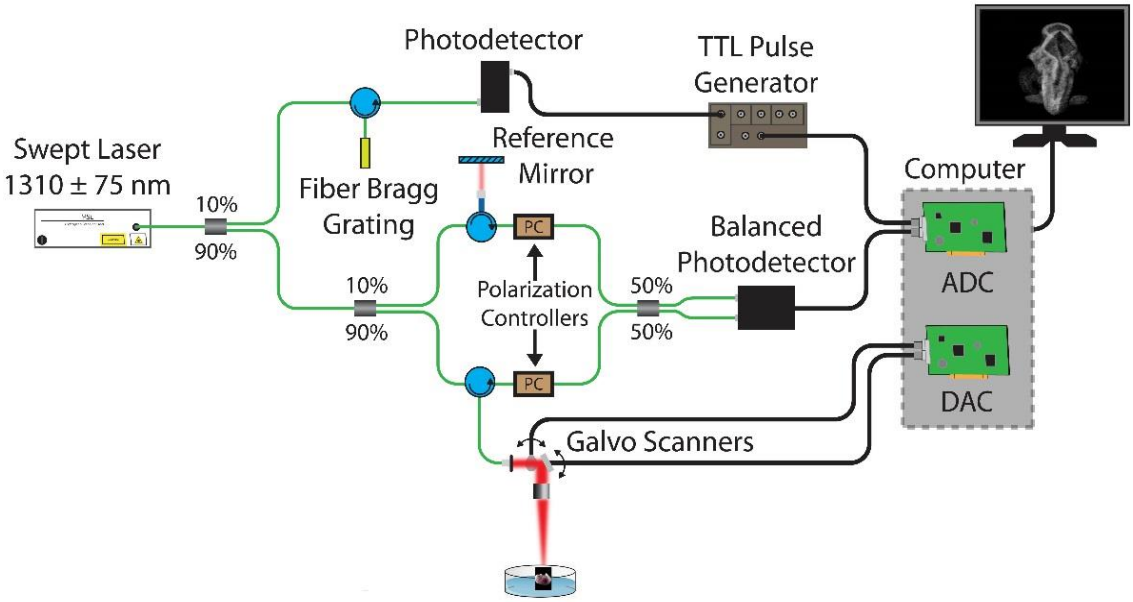

Figure A3.2 OCT system schematic. ADC: analog-to-digital converter; DAC: digital-to-analog converter.

14.2.4 Relationship between Brillouin frequency shift and elastic moduli

The frequency shift of the scattered light caused by the interaction of the incoming laser light with the acoustic phonons present within the material is called the Brillouin frequency shift (υB). The relationship between υB and the high frequency longitudinal modulus M' (the ratio of uniaxial stress to uniaxial strain) of a material is given by:

$$\upsilon B = \frac{2n}{\lambda}\sqrt{\left(\frac{M'}{\rho}\right)}\sin(\theta/2), \qquad (2)$$

where λ is the wavelength of the light source, n is the refractive index of the material, ρ is the density of the material, and Θ is the angle between the incident and scattered lights. Since this work uses backscattering, $\Theta = 180^0$. In order to obtain the longitudinal modulus, the value of ρ/n^2 is required. Although the density and the refractive index varies at different

locations in the sample due to its inhomogeneity, studies have shown that the variations in the ratio ρ/n^2 are fairly small for various biological samples such as cells and the cornea [344, 349]. Thus, the measured Brillouin shift is approximately proportional to the standard longitudinal modulus. The relationship between high-frequency longitudinal modulus and traditional quasi-static Young's or shear moduli that are generally used for material characterization is straightforward in crystalline material. However, the relationship is not well understood in biological tissues. For soft materials, such as biopolymers, biological tissues, and cells, the longitudinal modulus is generally much higher than the other traditional measures due to the incompressibility of the material and the frequency dependence of the modulus. It has been reported that empirically, the longitudinal modulus (M') measured by Brillouin microscopy has a log-log linear relationship to the conventional Young's modulus (E') given by:

$$\log(M') = a\,.\log(E') + b, \tag{3}$$

where a and b are material dependent coefficients [343]. For this study, the Brillouin shift is reported as a metric of the mechanical properties of the embryo as it is the direct parameter measured in the experiment.

14.3 Results

14.3.1 Stiffness differences of different regions of a developing embryo

A total of 5 embryos were imaged in this study. Figure 14.3 (a) depicts a 2D mechanical map of a sagittal plane of an embryo measured by Brillouin microscopy. Figure 14.3 (b) shows a similar 2D cross-sectional plane obtained from the 3D OCT image shown

in figure 14.3 (c). The neural folds, developing heart, and the neural tube/somites of the embryo can be identified in figure 14.3 (a) using the OCT image in figure 14.3 (b) as a reference.

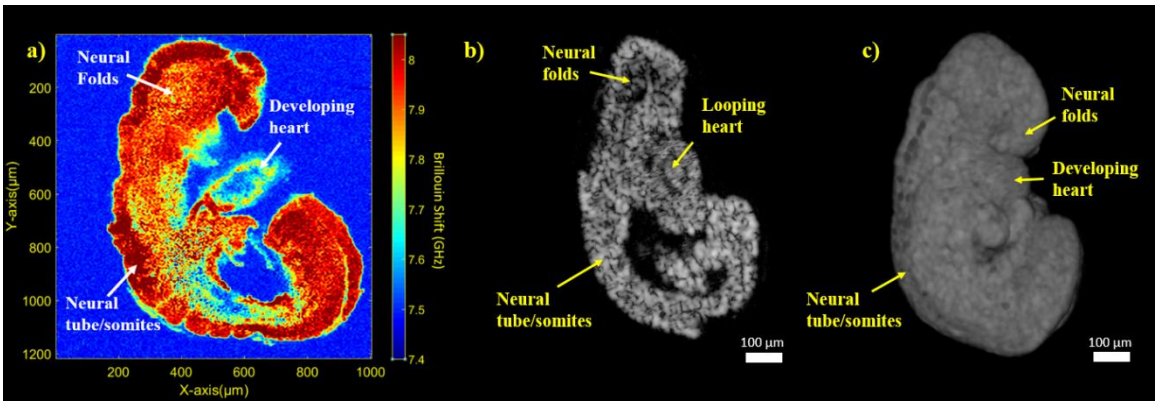

Figure A3.3 Images of embryo at GD 8.5. (a) 2D elasticity map obtained using Brillouin microscopy from one sagittal plane (b) 2D OCT image of a similar sagittal plane of the same embryo in (a). (c) 3D OCT image.

Mean Brillouin shift values of different regions of the embryo depicted by the dotted black circles in figure 14.4 (a) are plotted in figure 14.4 (b). From figure 14.4 (b) we observe that at GD 8.5, the neural tube/somites are much stiffer than the neural folds and the developing heart.

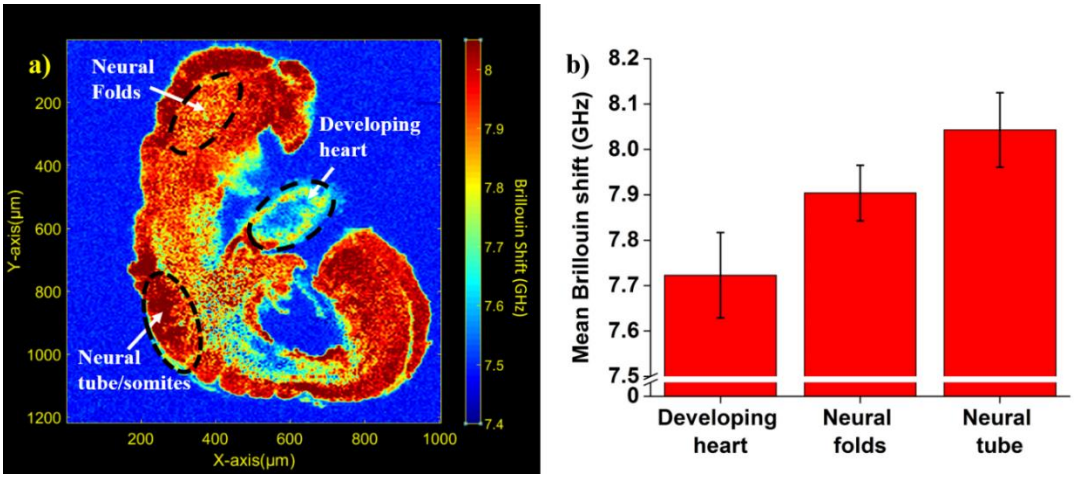

Figure A3.4 (a) 2D elasticity map obtained using Brillouin microscopy from one sagittal plane with labeled regions for quantifying embryo tissue stiffness and (b) stiffness quantifications of labeled regions.

14.3.2 Stiffness changes during neural tube development

Murine embryos at two different developmental stages were imaged to assess the biomechanical properties of neural tube before (GD 8.5) and after (GD 9.5) closure. Figures 14.5 (a) and (b) show OCT images of the neural tubes of the embryos at stages GD 8.5 and GD 9.5 respectively, while figures 14.5 (c) and (d) show the corresponding Brillouin images. From the Brillouin images, it is clearly seen that the neural tube stiffens after closure. The mean Brillouin shift of the entire neural tube region was calculated, and results showed that the Brillouin shift value of the closed neural tube was 0.21 GHz greater than the open neural tube (Figure 14.5 (e)). This amount of frequency difference corresponded to ~80% relative increase in Young's modulus as per the relationship between Brillouin-derived longitudinal modulus and Young's modulus.

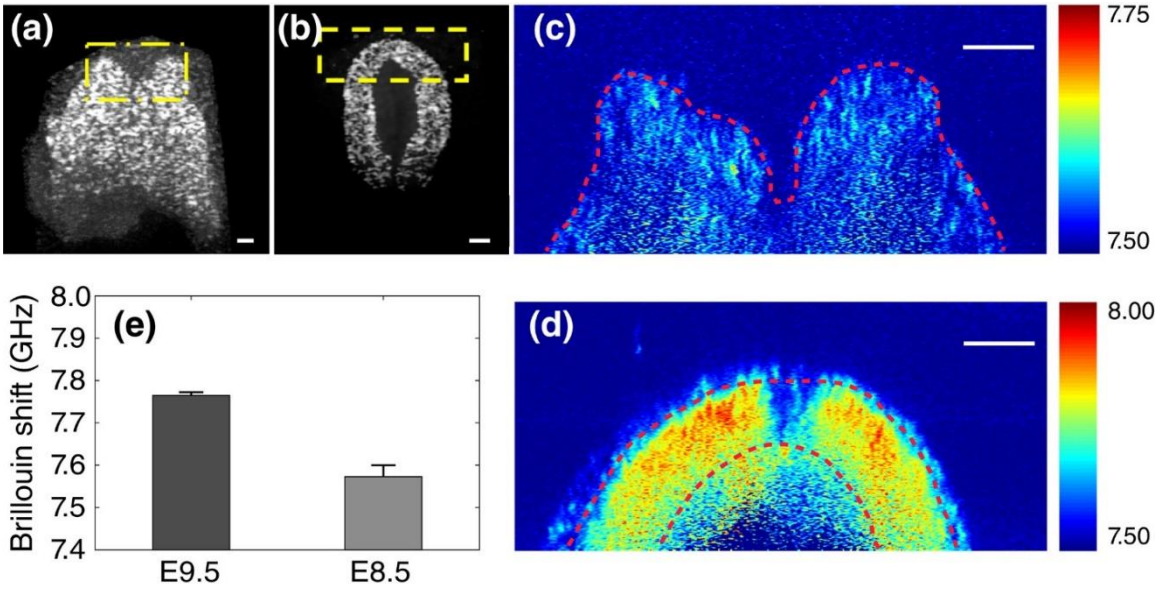

Figure A3.5 OCT cross sectional images of the neural tube of embryos at (a) GD 8.5, and (b) GD 9.5. (c) and (d) are Brillouin images at the same cross-sections depicted by OCT in (a) and (b). (e) averaged Brillouin shift of the neural tube tissue at GD 8.5 and GD 9.5. All scale bars are 100 μm.

Next, the modulus distribution along the neural folds were assessed after neural tube closure. Figures 14.6 (a-c) show 2D OCT cross-sections of three regions of the cranial neuropore. All three images confirm neural tube closure at these three different locations. The corresponding Brillouin cross-sections, depicted in figures 14.6 (d-f), showed modulus gradients along the neural tube. This was verified by dividing the entire neural fold region into several sub-regions and quantifying the mean Brillouin shift in each of these individual regions. These values were plotted and are shown in figures 14.6 (g-i). The Brillouin shift in the neural tube fusion region is much less than that of the adjacent neural folds. The difference in the shift values were within a range of 0.14 and 0.28 GHz, indicating that compared to the fusion region, the adjacent neural folds were ~60-100 % stiffer, in terms of Young's modulus. The plots also showed a decrease in modulus from the dorsal to the ventral region, depicted by the green arrows in figures 14.6 (g-i). Since a similar phenomenon wasn't observed at GD 8.5, this gradient could be related to the translocation of neuroepithelial cells in the ventral-dorsal direction during later development [352], indicating that this may play a crucial role in neural tube closure.

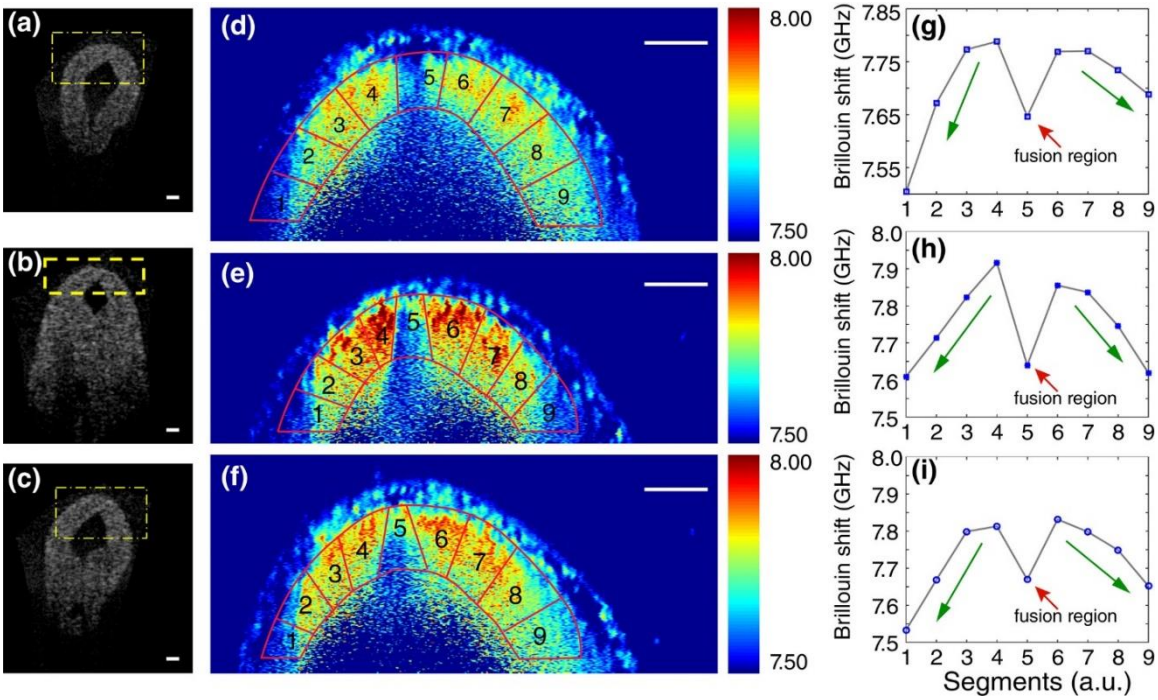

Figure A3.6 (a-c) OCT cross-sectional images of the neural tube of a GD 9.5 embryo. (d-f) Brillouin microscopy images of the cross-sections depicted by the yellow boxes in figures (a-c); (g-i) Brillouin shift of the different segmented regions of the neural tube. All scale bars are 100 μm.

The ectoderm is the layer surrounding the closed neural tube. This layer is usually only visible when a cell labelling technique is used. However, the 2D Brillouin maps obtained in this study were able to distinguish this layer from the remain neural tube tissue. The dashed white line in figures 14.7 (a-c) show this ectoderm layer. To quantify the difference in Brillouin shift, if any, between the neural folds (excluding the fusion region) and the ectoderm layer, the mean Brillouin shift value of three regions, the left and right sides of the neural tube, as indicated by the red dashed boxes in figures 14.7 (a-c), and the ectoderm layer was calculated and plotted in figures 14.7 (d-f). While the mean Brillouin shift values of the two sides of the neural tube were very similar, the Brillouin shift of the ectoderm layer was much smaller. This suggested that the ectoderm layer was ~80.4% softer than the closed neural tube in terms of Young's modulus.

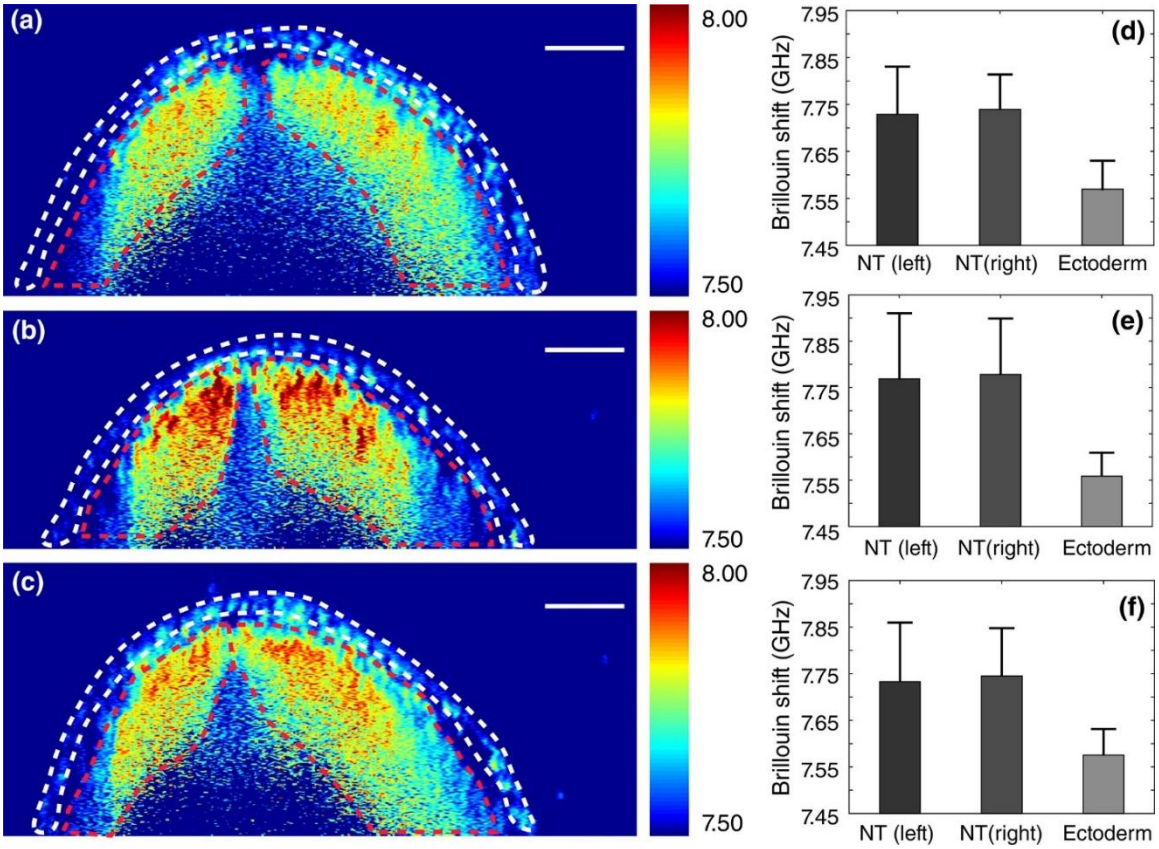

Figure A3.7 (a-c) Brillouin images of neural tube at different depths as shown in figure 5.6 (d-f). (d-f) Average Brillouin shift values of neural tube tissue (red dashed lines) and the ectoderm (dashed white lines). All scale bars are 100 µm.

14.4 Discussion and conclusions

In this section, preliminary studies to assess the stiffness of fetal tissues and changes in the biomechanical properties of the neural tube during closure were performed at different developmental stages. OCT provided structural guidance, and Brillouin microscopy was able to create mechanical maps of different cross sections of fetal tissue during development.

The neural tube closure is a highly dynamic process involving mechanical manipulations, which involves thickening, lengthening, elevating, and bending the tissue. All these processes are driven by mechanical forces at a cellular level. The changes in tissue stiffness observed in this study could be a result of all these processes and the forces driving these processes. McShane et al. reported an increase in cell density dorsolaterally compared to the ventromedial folds [352]. As tissue stiffness is closely related to cell density [353, 354], the modulus gradient observed in this study could be due to this difference in cell density that has been reported. However, more work is needed to provide closer and more direct correlations.

The relationship between the high frequency longitudinal modulus obtained from the Brillouin technique and the quasi-static Young's modulus measured by conventional methods is not clearly known. However, several studies have shown empirically that the moduli are strongly correlated [343, 349, 354]. A material-dependent calibration is required to obtain an accurate conversion from the longitudinal modulus to Young's modulus. For this study, the estimations of Young's modulus reported are based on calibrations from the retina. Future work will involve direct calibrations on neural tube tissue.

As shown in equation (2), the value of the Brillouin shift is also related to the density of the material (ρ) as well as the refractive index (n). The effects of these parameters were not investigated as a part of this study. Previous studies suggest that these two parameters are usually coupled with each other for biological samples such as cells and tissues [355, 356] and the ratio of $n/\sqrt{\rho}$ is nearly constant for cells [349]. A direct measurement of density and refractive index of embryonic tissue would also be a part of future work to be able to assess the longitudinal modulus more accurately. All measurements in these studies were conducted post-mortem, but future studies will image live embryos. Live imaging might cause a change in absolute values of the moduli but may not change the gradients observed here. This is a subject for future studies as well.

Due to elastic scattering from the embryonic tissue, the intensity of the Brillouin signal in this study dropped quickly as the imaging depth increased. This limitation could be surpassed using an advanced illumination strategy based on adaptive optics techniques [357].

Finally, as mentioned earlier, the long term goal is to study the effects of prenatal exposure to teratogens during the first trimester of gestation on NTC and its biomechanical dynamics. The process of neurulation occurs at a stage particularly vulnerable to teratogens during embryonic development [358]. Understanding the effects that teratogens have on NTC based on changes in tissue stiffness during embryogenesis would complement existing molecular and genetic research and provide new insights.